Downloaded from orbit.dtu.dk on: Dec 20, 2017

Technical University of Denmark

Computation of Superconducting Generators for Wind Turbine Applications

Rodriguez Zermeno, Victor Manuel ; Pedersen, Niels Falsig; Sørensen, Mads Peter; Kjær, Philip Carne ; Anbarasu, Ramasamy

Publication date:
2012

Document Version
Publisher's PDF, also known as Version of record

Link back to DTU Orbit

Citation (APA):
Rodriguez Zermeno, V. M., Pedersen, N. F., Sørensen, M. P., Kjær, P. C., & Anbarasu, R. (2012). Computation of Superconducting Generators for Wind Turbine Applications. Kgs. Lyngby: Technical University of Denmark (DTU).

DTU Library
Technical Information Center of Denmark

General rights
Copyright and moral rights for the publications made accessible in the public portal are retained by the authors and/or other copyright owners and it is a condition of accessing publications that users recognise and abide by the legal requirements associated with these rights.

- Users may download and print one copy of any publication from the public portal for the purpose of private study or research.
- You may not further distribute the material or use it for any profit-making activity or commercial gain
- You may freely distribute the URL identifying the publication in the public portal

If you believe that this document breaches copyright please contact us providing details, and we will remove access to the work immediately and investigate your claim.

PhD. thesis
Víctor Manuel Rodríguez Zermeño
March 2012

Computation of Superconducting Generators for Wind Turbine Applications

DTU Mathematics
Department of Mathematics

Title of the thesis:
Computation of Superconducting Generators for Wind Turbine Applications

Ph.D. student:
Víctor Manuel Rodríguez Zermeño
DTU Mathematics
Department of Mathematics
Technical University of Denmark
2800 Kgs. Lyngby
Denmark
Email: V.Zermeno@mat.dtu.dk

Supervisors:
Mads Peter Sørensen
Associate professor
DTU Mathematics
Department of Mathematics
Technical University of Denmark
2800 Kgs. Lyngby
Denmark
Email: M.P.Soerensen@mat.dtu.dk

Niels Falsig Pedersen, Professor (emeritus)
DTU Mathematics
Department of Mathematics
Technical University of Denmark
2800 Kgs. Lyngby
Denmark
Email: n.f.pedersen@mat.dtu.dk

Chief Specialist Philip Carne Kjær,
Technology R&D, Power Plant,
Vestas Wind Systems

Dr. Ramasamy Anbarasu
Manager Advanced Generator Technology
Advanced Generator Technology, DE
Lübeck, Germany, Vestas Technology R&D.

A mis padres

Abstract

The idea of introducing a superconducting generator for offshore wind turbine applications has received increasing support. It has been proposed as a way to meet energy market requirements and policies demanding clean energy sources in the near future. However, design considerations have to take into account hysteresis losses in the superconducting windings during transient responses. Modeling and simulation of these transients is a challenging task. It requires considering a system that spans spatially 5 (or 6) orders of magnitude: from the 1 μm thick superconducting layers in the windings, to the actual generators in the KW (MW) class with an expected cross section in the order of decimeters (meters).

This thesis work presents cumulative results intended to create a bottom-up model of a synchronous generator with superconducting rotor windings. In a first approach, multiscale meshes with large aspect ratio elements are used to simulate the electromagnetic properties of superconducting thin films. This provided a computational speedup of two to three orders of magnitude without compromising accuracy. A second approach used a homogeneous-medium anisotropic bulk with a power law $\boldsymbol{E}-\boldsymbol{J}$ relationship to model stacks of superconducting tapes. This method provided an additional speedup of about two orders of magnitude when calculating AC losses in superconducting stacks.

The anisotropic bulk was latter used to model a generator with superconducting rotor windings. Transient response of the generator including ramp-up of rotor coils, load connection and change was simulated. Hence, transient hysteresis losses in the superconducting coils were computed. This allowed addressing several important design and performance issues such as critical current of the superconducting coils, electric load change rate, cryostat design and identification of *quench-prone* regions.

Keywords: Superconducting generator; AC losses; Finite Element Simulation; Homogenization; HTS coils.

Acknowledgments

First and foremost, I want to thank my main thesis advisor, Associate Professor Mads Peter Sørensen for giving me the opportunity to work with him, and for all his support and teachings during my PhD study. His unbounded patience and trust were a true gift to me.

I want to thank Dr. Asger B. Abrahamsen for always being there, helping me close the gap in my work. A big part of it is not but a consequence of our long conversations. I would have had a much harder job in this journey without his constant guidance.

I thank specially my fellow colleague Nenad Mijatovic, who provided all the generator information, designs and models along with irreplaceable support. Every discussion, collaboration and advice made my task easier.

Also, I want to thank all the people who hosted my academic visits: Prof. Archie Campbell and Dr. Tim Coombs from University of Cambridge; Dr. Fedor Gömöry from the Slovak Academy of Sciences and Dr. Frédéric Sirois from École Polytechnique de Montréal.

I want to thank all the people who beyond the spirit of collaboration shared their knowledge and network of contacts with me: Professor Niels Falsig Pedersen, MC Mark Ainslie, Dr. Bogi Bech Jensen, Dr. Enric Pardo, Dr. Francesco Grilli, Dr. Weijia Yuan and Dr. Steeve Memieage. Also, I want to thank the great support received by Dr. Lars Gregersen from COMSOL Multiphysics.

On a personal note, I thank my fiancé Analie, for following me to these latitudes so that I could pursue my goals. Her encouragement, kindness and love have made this journey a pleasant experience.

Finally, I thank the support received from the Technical University of Denmark, the Danish Center for Applied Mathematics and Mechanics, Vestas Wind Systems and SEP- Mexico.

Contents

Abstract ...iii

Acknowledgments ... v

Introduction ... 1

Chapter 1 Motivation ... 3

1.1 Energy requirements, policies and wind power in EU ... 3

1.2 Permanent magnet based technology and rare earth elements supply ... 4

1.3 A superconducting generator for wind turbines applications ... 5

1.4 Modeling and simulation challenges ... 8

Chapter 2 Modeling and Simulation ... 9

2.1 Type-II Superconductors ... 9

2.2 E-J relationship and critical current density ... 11

2.3 Formulation ... 13

2.4 Several parallel conductors ... 15

2.5 Simulation ... 16

2.6 The Finite Element Method and COMSOL Multiphysics ... 16

Chapter 3 Stacks and coils ... 21

3.1 Importance of 2G HTS stacks ... 21

3.2 Structured (mapped) meshes ... 22

3.3 Validation ... 23

3.4 Simulation of a racetrack coil ... 25

3.5 Calculation of AC Losses ... 28

3.6 Conclusion ... 29

Chapter 4 Homogenization ... 31

4.1 Challenges in 2D formulations ... 31

4.2 State of the art ... 31

4.3 Modeling Strategy ... 32

4.4 Formulation ... 32

4.5 Validation strategy ... 34

4.6 Transport current ... 36

4.7 Applied magnetic field ... 39

4.8 Conclusions ... 41

Chapter 5 Simulation of a HTS generator ... 43

5.1 Background 43
5.2 Simulation Strategy 43
Generator model 44
Coils model 45
5.3 Case study: Load change 45
5.4 Results 46
5.5 Discussion 51
5.6 Conclusions 52
Chapter 6 Summary of Publications 53
Chapter 7 Concluding Remarks 55
7.1 Future work 55
Bibliography 57
Appendix A 63
Appendix B 71
Appendix C 77
Appendix D 87
Appendix E 95
Appendix F 103

Introduction

The background of this Ph.D.-study comes from cooperation between Vestas Wind Systems, and the Departments of Mathematics and Electrical Engineering of the Technical University of Denmark. The aim of said cooperation is to study the feasibility of introducing wind turbine generators based on high temperature superconductors. This thesis presents the main findings of the PhD project entitled "Computation of Superconducting Wind Turbine Generators". The project focused on developing tools for modeling and simulation of large scale superconducting devices with aims towards computing the hysteresis losses of a superconducting generator during transient operation. This work was carried out at the Department of Mathematics of the Technical University of Denmark from December 2008 to February 2012.

As a motivating preamble, Chapter 1 starts with a discussion about energy requirements, and related policies in the EU. Emphasis is made upon the case of offshore wind power installations and their future share of the European energy market. Challenges associated with raw material availability, maintenance, size and weight for the upcoming installations are considered. After a brief discussion use of superconducting generators in wind turbine applications is considered as a cost effective alternative in the 5 to 10 MW rating. The current challenges in modeling and simulation of large scale superconducting devices are presented towards the end of the chapter. Chapter 2 gives a brief description of the mechanism behind the losses in type-II superconductors. The chosen formulation for modeling and simulation by finite elements is presented there. As a way to speed up computations, in Chapter 3, structured meshes with aspect ratios resembling the layered conductors are used to simulate stacks of superconducting tapes. This technique is used for calculating AC losses in a 57 turn race-track coil. A homogenization technique that allows for further computational time reduction is presented in Chapter 4. In Chapter 5, simulation of the transient response of a superconducting generator is presented. Both ramp-up of the rotor coils and electric load change cases are considered. Chapters 6 and 7 present the summary of publication and concluding remarks respectively. Finally, the appendixes recollect the documents published during the course of this PhD study.

Chapter 1 Motivation

The rising demand for cleaner, cost effective, methods for electric power generation impulses the development of new alternatives. In this chapter, some of them are analyzed under the light of the European energy market requirements and policies. Emphasis is made on the wind turbine sector and its forecasted future share of the energy market. For the case of upcoming offshore wind power installations, several challenges related to both deployment (weight and size) and upkeep (long term reliability) are discussed. Particular attention is given to the case of rare earth permanent magnet based generators. Forthcoming raw material availability is analyzed considering both demand growth and concentration of supply. The case for the superconducting generator in wind turbine applications is made as a cost effective alternative to meet future demands and policies. Finally, the need for simulation tools in designing and testing these machines is presented as a multiscale problem spanning 5 to 6 orders of magnitude.

1.1 Energy requirements, policies and wind power in EU

According to the Energy Roadmap 2050 for the EU [1], "The EU has committed to reducing greenhouse gas emissions to 80-95% below 1990 levels by 2050". This increases pressure upon the clean alternatives to be implemented for fulfilling such requirements. In this sense, several low carbon technologies — mainly nuclear and hydropower — already make up for up to 45% percent of electricity generation in the EU [2]. However, in the period from 2000 to 2010, the nuclear energy sector experienced a net decline of 7.6 GW, while large-hydropower presented a net growth of just 3 GW. In the same period, photovoltaic sources achieved a net growth of 26.4 GW, while wind stood as the fastest growing of the low carbon emitting technologies with a handsome 75.2 GW. At the end of 2010, wind power alone accounted for 84 GW, covering 5.3% of the EU electricity demands [3]. In this context it is worth noticing Denmark's leadership: 21% of its electricity needs are met from wind sources, the biggest relative share for any country [4].

Furthermore, according to the UpWind Final report [5] by 2020, a 265 GW wind powered capacity will be necessary to fulfill the European Commission‘s ambitions for wind energy. The same publication indicates the importance of offshore installations: offshore wind turbines are expected to be the most competitive energy source by 2030 without considering external costs. Besides, offshore technology is expected to provide 21% of all wind power by 2020, 37.5% by 2030 and 58% by 2050 -- the report points out. However, to achieve such energy payload, offshore wind power installations must meet many challenges as the technologies and know-how used in onshore technologies are not fully applicable to offshore facilities [5]. Therefore, offshore wind power presents a seedbed for new technologies that must tackle problems such as size, weight and maintenance. For instance, repairs could be not straightforward in the North and Baltic seas, where wind farms are expected to be deployed. The same high speed winds that make such regions attractive for energy farming are the same that make upkeep and troubleshooting a challenging task.

Cost effective offshore wind turbines will require more reliable components at a low maintenance cost. Direct drive train technologies provide with a reliable option, as the absence of a mechanical transmission avoids many potential failures associated with wear and maintenance. However, one of the most obvious drawbacks of such technology is the need to reduce the speed of the generator as it must now rotate along with the turbine blades i.e. 12.1 rmp for the 5 MW class [6]. This consideration is clearly drawn by Mijatovic et al. [7]: To match the power output, the smaller rotational speed must be compensated for with an increase in size and/or air gap magnetic field magnitude. Conventional machines with copper windings could provide a high field, although its strength will be limited by Joule heating in the rotor windings and the saturation magnetization of steel [7] [8] [9]. Therefore, other drive train alternatives will be necessary to meet the EU goals for 2050.

1.2 Permanent magnet based technology and rare earth elements supply

One option that recently received particular attention from UpWind [5], as a way to cope with offshore needs, is the use of permanent magnet generators. After introduction of their V112-3.0 MW model, Vestas has now launched a turbine completely dedicated to offshore environments, the V164-7.0 MW [10]. Although these new models still have a gearbox, they benefit from the high field of a permanent magnet generator. Among others, Goldwind's 1.5 MW and 2.5MW rated wind turbines; Siemens SWT-2.3 and SWT-3.0; and GE's 4.1-113 turbines all rely upon a direct drive and permanent magnet based technology [11] [12] [13]. While, at this moment, permanent magnet technology is commercially available for offshore applications, rare earth elements supply could prove to be a limiting factor on the large scale at low cost implementation.

Neodymium magnets ($Nd_2Fe_{14}B$) are more powerful than other alternatives, with up to 2.5 times the magnetic energy of their samarium-cobalt counterparts [14]. However, the success rare earth permanent magnets achieve is not exclusive for the wind energy sector. Both long-standing and emerging technologies are benefiting from them: hard disks, DVD drives, and hybrid cars -with models like the Toyota Prius which demands 1kg of Neodymium per unit [14].

A recent study by The Institute for Energy and Transport of the Joint Research Centre (JRC) of the European Commission [15] shows that for low-speed wind turbines, an expected 700 kg of permanent magnets per MW of installed capacity are necessary. Such magnets are 30% Neodymium in composition; this implies that about 210 kg per MW will be needed. According to the Lynas corporation annual report [16], the price of the Chinese exported Neodymium Oxides rose more than 800% from the 1st quarter of 2010 to the 2nd quarter of 2011. Furthermore, recent estimates [15] show that if the penetration of permanent magnet generators for wind turbines continues as projected, then by 2030, EU would require up to 4% of the world production of 2010. This should be analyzed and contrasted under the light of the developing economies growth. For instance, during 2010 alone, China created 18.9 GW of wind power [4]. This is more than double the EU-27's 9.3GW installation during the same period. Being China the leading provider of rare earth oxides, this issue puts a great pressure on the developing technologies that rely on Neodymium based compounds, such as permanent magnets. Hence, the competition for a share of the market is expected to become even fiercer in the following years. The JRC report [15] already warns that Neodymium is in high risk of future supply chain bottlenecks due to its likelihood of rapid demand growth, concentration of supply and the political risk involved. Therefore a new alternative proposal capable of avoiding this dependency is likely to find a niche in the sector and penetrate the wind power offshore market, not just in Europe, but worldwide.

1.3 A superconducting generator for wind turbines applications

Coils manufactured from High Temperature Superconductors (HTS) can deliver much higher magnetic fields than the strongest permanent magnets as the later become saturated when all the magnetic moments of the Fe atoms of the Neodymium magnet ($Nd_2Fe_{14}B$) become aligned [9]. Moreover, in a comparison of different generator design concepts for offshore wind turbines [17], several drawbacks of the technologies are presented. In the particular case of permanent magnet synchronous machines, the following shortcomings are mentioned: weight and size already present a problem from transportation to assembly; a heavier structure is needed to hold these heavier generators; and finally, as it is not possible to "turn off" the field of a permanent magnet in the same way that in a coil, special care must be taken when revising permanent magnet generators as they are constantly energized. Lesser et al. [17] conclude that for wind turbines dedicated to offshore applications at or above the 5MW threshold, the superconducting solution will become a competitive option.

An insight from the point of view of the materials needed in HTS generators is given in a recent estimate by the Superwind project at DTU [6]. The study, which presents feasibility estimates for a 5MW superconducting wind turbine generator, predicts that about 500kg of the 2nd generation (2G) HTS coated conductor manufactured by Superpower [18] are sufficient for such a generator: only 100kg of coated conductors per MW of installed power capacity. 2G HTS coated conductors are layered composites with a thin layer of the superconductor $YBa_2Cu_3O_{7-x}$ (YBCO) grown on top of a substrate and covered with an stabilizer metal like copper as shown in Figure 1. Note that coated conductors contain about 1% of YBCO. Following from the above discussion, it is pointed out that roughly 1kg of YBCO (less than 140 g of Yttrium) per MW of installed capacity will be necessary.

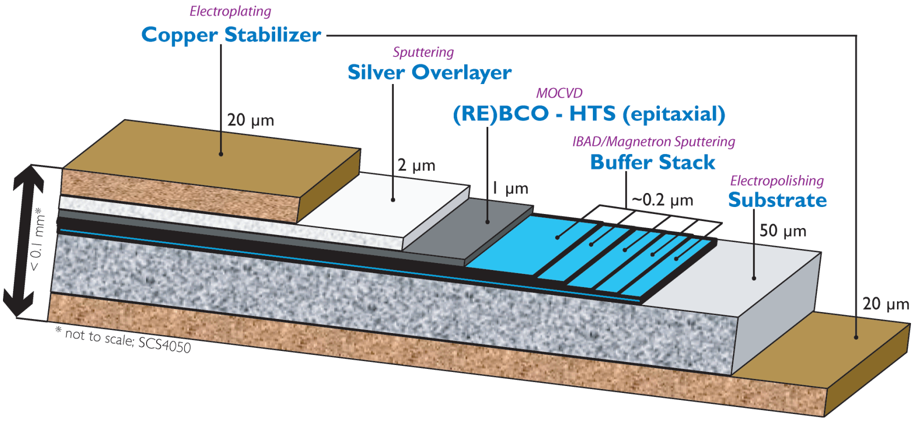

Figure 1. Structure of a 2G HTS coated conductor. Image courtesy of SuperPower Inc [18].

Furthermore, Yttrium, the only rare earth involved in commercially available HTS coated conductors, occurs in nearly all of the rare-earth minerals [19]. Hence given the overall high demand for rare-earths, Yttrium availability is expected to come steady. Overall, most raw materials involved in production of the superconducting material YBCO do not make a high mark in the JRC report which aims to assess the impact of critical metals in Low-Carbon Technologies [15]. The report presents the metals requirements of the EU's Strategic Energy Technology Plan in 2030 as % of 2010 World Supply. Besides Silver, none of the materials needed for 2G HTS coated conductors scores above 1%. In fact, Yttrium marks just under 0.1%. This shows that YBCO based coated conductors are expected to avoid both natural resources bottlenecks as well as competition from other Low-Carbon Technologies.

Although, tests of rotating machinery based in Low Temperature Superconductors (LTS) in the 70's-90's proved successful, the low operational temperature and the related requirement of an extremely efficient cryostat running on liquid helium made commercial application of this technology a challenge that was not surpassed. However, appearance of HTS allowed placing the question once again when materials with transition temperatures above liquid nitrogen emerged [20]. The improvements provided by the 1st generation (1G) HTS wires based on $Bi_2Sr_2Ca_2Cu_3O_{10+x}$ (BSCCO) saw their main drawbacks from the raw materials needed for manufacturing: 1G HTS wires are manufactured by pouring powdered BSCCO into a large Silver matrix. The high price of Silver proved to be a limiting factor for large scale implementations [9].

Despite being used in both 1G and 2G HTS coated conductors, Silver accounts for only 2% of the volume fraction for the 2G case, a much lower number when compared to 1G. Hence, as previously discussed, 2G HTS tapes do not have such limiting factors. In fact, recent estimates [21] assume that a price reduction (in $/kA-m) in excess to one order of magnitude can be achieved within the next five years. Thus, allowing the introduction of 2G HTS in both medium and large scale commercial market applications. It is clear, that use of superconducting materials in the rotor windings of a generator has become an option worth exploring for as both price and availability show a promising near future.

The case for using HTS coils in electric generators for wind turbine applications is well discussed by Abrahamsen et al. [9]. According to that study, direct drive superconducting generators are expected to be both lighter and smaller. Additionally, not having a gearbox, reduced mechanical wear will trim down the subsequent maintenance visits, both scheduled and remedial. This is a very important issue, especially for offshore applications where a faulty gearbox can stop the turbine performance over extended periods of time.

In fact, in recent years, several examples of commercial HTS rotating machines in the MW ratings have either being built or are still in development [20] [22] [17] [18]. The main advantages reported are:

- Size and weight reduction
- High efficiency at both full and partial load
- Halved losses
- Increase in power quality
- Lack of iron teeth reduces noise
- Higher power density

Furthermore, as of today, several initiatives intended to build superconducting generators for wind power applications as shown in Figure 2 have emerged, among others: American Superconductor/TECO–Westinghouse with their 10MW rated Sea Titan wind turbine [23]; AML Energy with a fully superconducting MgB_2 based generator also in the 10MW rating [24]; and Converteam/Zenergy with an 8 MW design [25].

Although, as previously mentioned, several HTS rotating machines based on 2G coated conductors have been already built and tested; special considerations are to be taken into account in the design of a generator intended for wind turbine applications. While rotating at constant angular speed, the magnetic field in the rotor's coils of a synchronous generator is expected to be constant under ideal operational conditions, i.e. constant resistive electric load. Therefore, in principle, losses in the superconducting windings should not be a big concern as long as both, the rotor speed is kept constant, and the electric load does not present transients or reactive components (loads with inductive or capacitive components).

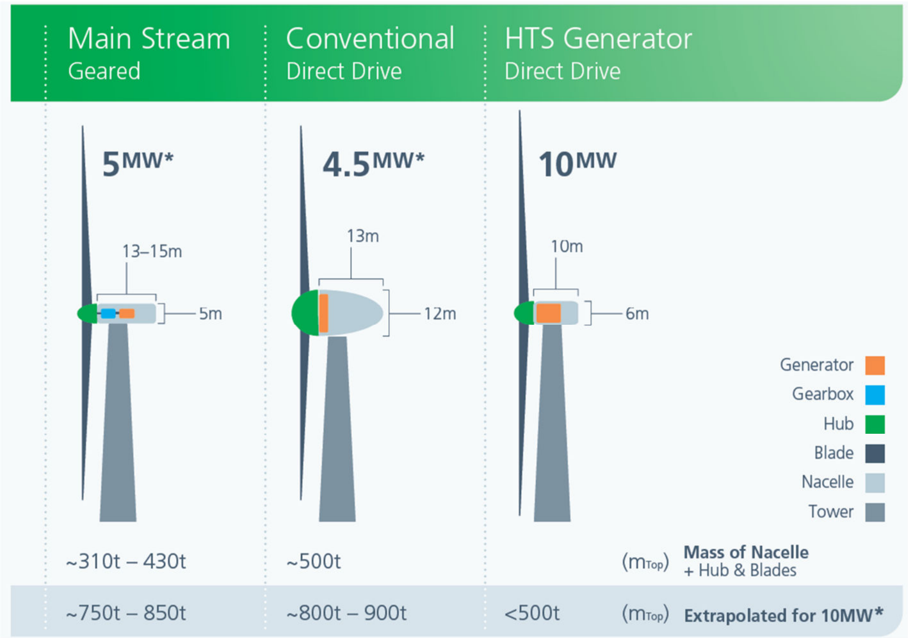

Figure 2. Comparison of various wind turbine designs. Note the substantial size and weight reductions expected with the introduction of superconducting windings. Image courtesy of American Superconductor [23].

However, given its stochastic nature, wind velocity is expected to change over time, both in the short term due to meteorological conditions and in the long term due to seasonal events. Additionally, in offshore wind farms with several turbines allocated in a fixed array, wind direction change will affect the wind velocity throughout the farm as the turbines facing the wind will mask it for the turbines behind them. Finally, wind turbines are expected to operate at a better performance within a certain wind speed range. A cut-in speed will determine the minimal wind speed at which the turbine is set to start rotating. In the same way, a cut-out speed will provide with a maximal wind speed at which the turbine is expected to work without risk [9]. Thus, for all wind speeds outside this nominal range, the turbine is expected to be turned off until the wind speed reaches an acceptable value. Every time a superconducting generator is started and stopped, hysteretic losses are to be expected as it interacts with the electric grid. Furthermore, in real operational conditions, load changes are expected as a part of everyday grid performance. In the same way, unbalanced loads and even short circuits should be considered as they can occur during ordinary work conditions or accidental disruptions in power demand. This non-ideal interaction with the electric grid will produce magnetic field fluctuations in the rotor’s coils. Clearly, these AC field ripples will amount to hysteresis losses in the superconducting windings. Overall, several sources, of either mechanical and/or electromagnetic character are expected to contribute to the AC heating losses. Understanding and being able of predicting these losses is fundamental for cryostat design. An exceedingly robust cryocooler design will decrease the overall efficiency while adding undesired weight and volume to the generator. In the same manner, safety and long term durability can be compromised by an optimistic design of the cryostat.

Despite the serious concerns described above, several technical resources can be applied to lower both mechanical and electrically born hysteretic losses in the superconducting windings. Pitch regulation of the blades angles can help on easing transient mechanical inputs such as wind speed change or start up and turn off, hence providing with a steadier rotational speed. In a similar fashion, use of power converters can allow for smoothing the grid interaction and up to some degree deal with load unbalance, reactive loads and load change transients. But although some of the causes of HTS AC losses can be trimmed down with external devices, they will always be a matter of concern that must be taken into account while designing a superconducting generator. Consequences of unattended heating can lead to permanent damage of the machine. For instance, thermal run-away can be triggered by local temporary heat dissipation. This, in turn, would lead to detrimental burn out of the superconducting materials if excess heat is not removed fast enough or if protective measures are not enforced [26]. Thus determining safety limits from the operation point to critical boundaries is very important.

1.4 Modeling and simulation challenges

Calculation of AC losses in HTS tapes typically requires using infinite dimensional models based on either integral equations [27] [28], partial differential equations [29] [30] [31] [32] or quasi-variational inequalities [33]. Although, a few analytical solutions do exist for particular geometries as described for instance in [34] [35], no general closed form solution is available yet. However, for practical matters, most formulations can be solved using a variety of numerical methods such as finite elements, finite differences or finite volumes among others. While sound results have been obtained with the aforementioned formulations, the numerical burden involved on simulating a large number of conductors can pose a significant shortcoming. Hence, simulation of large scale HTS devices such as magnet coils, transformers, generators and motors is limited by this issue.

This problem has already proven to be a matter of concern, and several efforts have been directed towards that end. For certain limiting cases such as infinite stacks, some results are already available [34] [36]. The case of a finite stack has already been treated in some small configurations [37] [38]. Other methods based on homogenization techniques include the works of Clem et al. [39], Yuan et al. [40] and the more recent work of Prigozhin and Sokolovsky [41]. These methods will be discussed in detail in chapter 4, where some of their inherent drawbacks will be discussed.

Furthermore, the multiscale nature of the problem at hand presents additional challenges. 2G HTS coated conductors have a thin superconducting layer of about 1 μm in thickness. On the opposite end of the scale, generators in the MW (KW) class are expected to have a cross section in the order of meters (decimeters). Within this range, the typical thickness of the tapes is found at about 100 μm, while the coils are in the centimeter to decimeter range. Overall, a successful model will span spatially the required 5 to 6 orders of magnitude connecting these phenomena. In order to perform such large scale simulations within reasonable computing and programing times, new models and/or simulation tools need to be developed.

Such tools should be comparable in speed and accuracy to the commercially available software packages based in the Finite Element Method currently used for electromagnetic simulations of rotating machinery. Also, it should provide with an easy and natural way to include normal conductors and magnetic materials with nonlinear properties. Therefore, design, analysis and optimization of superconducting devices for power applications should become an uncomplicated task.

Chapter 2 Modeling and Simulation

This chapter gives a brief introduction to the properties of type-II superconductors and describes the mechanism behind the losses under applied current transport. Expressions for the macroscopic constitutive relationship between the electric field $\boldsymbol{E}$ and the current density $\boldsymbol{J}$ and for the critical current density J_c are discussed. The chosen formulation based on the magnetic field $\boldsymbol{H}$, is deduced for the case of several conductors. Finally, a brief description of the finite element method and its solution in COMSOL Multiphysics is given.

2.1 Type-II Superconductors

Type-II superconducting materials such as YBCO are characterized for presenting three significantly different states. These states are separated by two critical magnetic fields, namely H_{c1} and H_{c2}. If the magnetic field is below the lower critical field H_{c1}, the Meissner state is exhibited and most magnetic field is expelled from the material. Only a small layer in the surface is penetrated up to a distance known as the London penetration depth. While in this state, the material is superconducting. Fields above the upper critical field H_{c2} have the effect of cancelling all superconducting behavior as the material turns into a normal conductor, hence exhibiting Ohmic losses for applied transport currents. A more interesting effect happens when fields above H_{c1} but below the upper critical field H_{c2} are applied (either externally or as a consequence of transport current). In this state, the material is a mixture of normal and superconducting materials. A phase diagram describing these three states is presented in Figure 3.

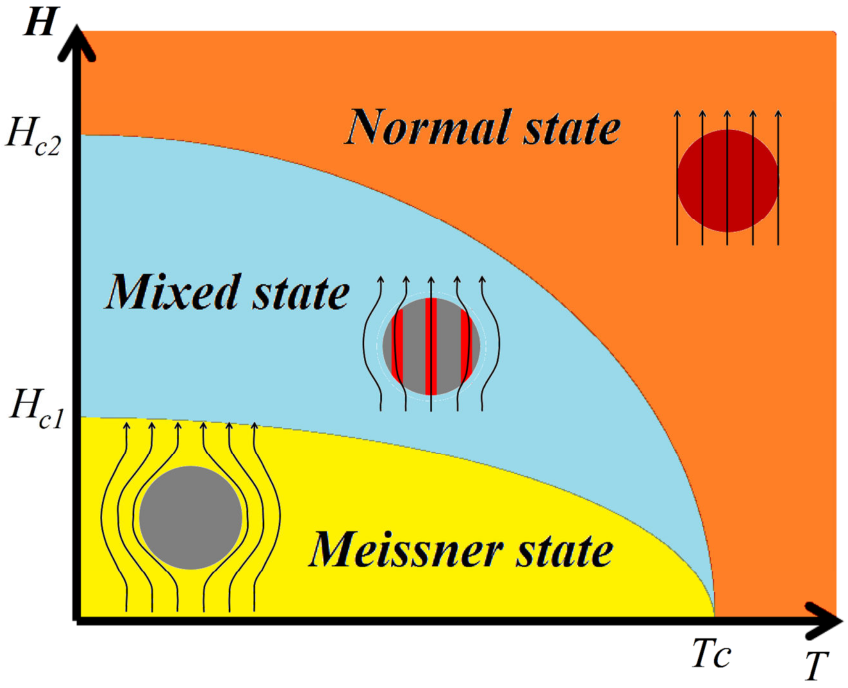

Figure 3. Phase diagram for type II superconductors. For fields below H_{c1}, the Meissner state is observed. Fields above H_{c2} turn the material into a normal conductor. However, for fields above H_{c1} but below H_{c2}, a mixed state in seen.

In the mixed state, as shown in Figure 4, magnetic field lines penetrate through small regions of the material. These regions become normal conductors within the otherwise superconducting sample. Screening circular currents – called Abrikosov vortices – are created around the field lines. For this reason, the mixed state is also referred to as vortex state. Through this work, HTS materials will be assumed to be on the mixed state. Through each vortex passes a quantized magnetic flux:

$$\Phi_0 = h/2e \tag{1}$$

where, h is the Plank's constant and e, the electron charge. When an electric current is applied to a type-II superconductor, the vortices in the material will experience a Lorentz force per length unit given by:

$$\boldsymbol{F} = \boldsymbol{J} \times \Phi_0 \hat{\boldsymbol{y}} \tag{2}$$

where J is the local current density. If the force is strong enough to move the flux line, then, energy will be dissipated as:

$$W = \int \boldsymbol{F} \cdot d\hat{\boldsymbol{z}} \tag{3}$$

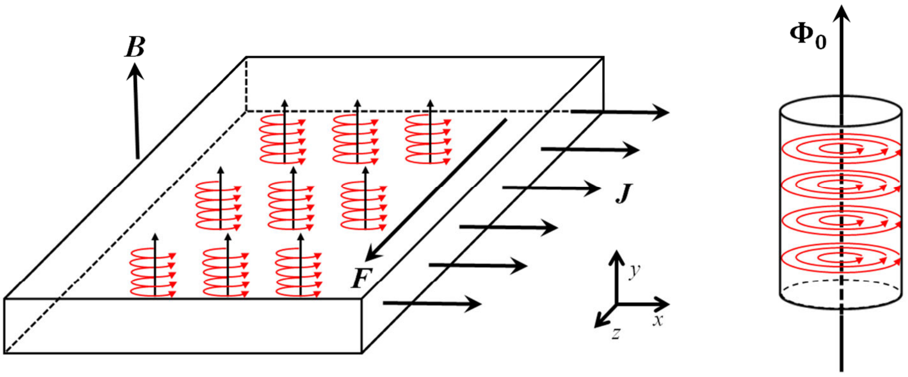

Figure 4. *Left:* Lorentz force on the vortices of a type II superconductor in the mixed state. A current density $\boldsymbol{J}$ in the $\hat{\boldsymbol{x}}$ direction and a magnetic flux density $\boldsymbol{B}$ in the $\hat{\boldsymbol{y}}$ direction are applied, producing a Lorentz force $\boldsymbol{F}$ in the $\hat{\boldsymbol{z}}$ direction that acts on each vortex. *Rigth:* Each vortex has a quantized magnetic flux $\Phi_0 = h/2e$.

However, vortices typically stick to material defects. These defects can come from a wide variety of sources, either as a non-intended manufacturing issue or as a carefully planned addition. It turns out that the vortex energy is reduced in these locations, hence the associated potential energy wells will pin the vortices in the material with a so called "pinning force" [42]. The pinning force can then be expressed as:

$$F_p = \nabla U_p \tag{4}$$

where U_p is the pinning energy. As long as the pinning force is larger than the Lorentz force acting on a vortex, no displacement will occur. Hence, transport current will be possible without incurring in energy dissipation. On the other hand, following from equation (3), if no pinning is exhibited at all, the zero resistivity characteristic of the superconducting material will be lost, as energy will be dissipated. It is the balance between the pinning and the Lorentz forces that gives rise to the critical current density. It can be thought of as the maximum allowed current density producing a Lorentz force that does not yet overcome the pinning force. Assuming the geometry as described in

Figure 4, the forces in equations (2) and (4) are balanced when $J = J_c$. Solving these equations for J_c yields:

$$J_c = \frac{\nabla U_p}{\Phi_0} \tag{5}$$

The interaction among vortices has been disregarded, but this picture helps to describe the nature of the critical current density as a consequence of vortex pinning.

In a phenomenological way, the Ginzburg-Landau equations can be used to describe the behavior of superconductors in the mixed state. Their numerical solution by means of finite elements has been studied for more than 20 years [43]. However, as pointed out by Bossavit [44] this approach is not a suitable option when dealing with samples much larger than the characteristic size of the Abrikosov vortices' lattice. Given that the power applications intended in this work fall far from this spatial scales, other modeling and simulation strategies were sought to consider the macroscopic behavior of superconductors. In what follows, material characteristics are presented along with macroscopic constitutive relations before discussing the selected modeling strategy and its solution by the finite element method.

2.2 E-J relationship and critical current density

As already mentioned, being in the mixed state, superconducting materials will exhibit a non-zero resistivity that increases for either large enough applied transport currents or magnetic fields. A typical set of I-V curves for a 2G HTS coated conductor is presented in Figure 5.

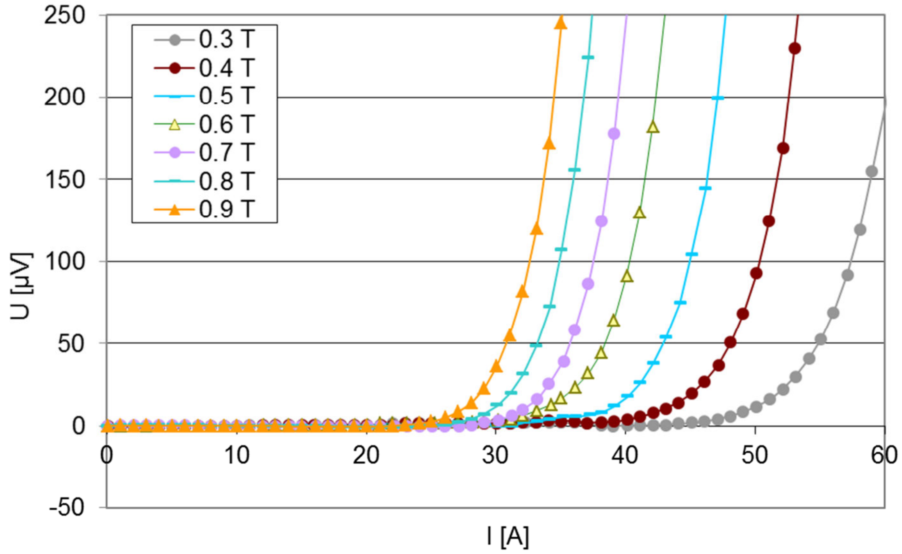

Figure 5. IV-curves at 77K for different magnetic fields applied perpendicular to the tape's wide face of a Superpower [18] coated conductor. Data courtesy of Asger B. Abrahamsen.

Macroscopically, the Current–Voltage characteristic relation in 2G HTS coated conductors can be modeled by fitting experimental data with the following power law:

$$V = V_0 \left| \frac{I}{I_c(\boldsymbol{B})} \right|^{n(\boldsymbol{B})} sign(I) \tag{6}$$

Here, V and I stand for the voltage drop across the conductor and the transport current respectively; both $Ic(\boldsymbol{B})$ and $n(\boldsymbol{B})$ are scalar functions of the magnetic flux density $\boldsymbol{B}$; and V_0 is a constant, set so that a 1μV/cm criteria is met. This means that, in DC conditions, the critical current $Ic(\boldsymbol{B})$ of a coated conductor is reached once a voltage drop of 1μV is observed in a 1cm long sample. The power law exponent $n(\boldsymbol{B})$, determines how sharp the transition from the superconducting to the resistive state is.

The critical state model proposed by Bean [45], and further improvements made by Kim et al. [46] provided with very useful ways to calculate AC losses in superconductors, however those models consider a discontinuous $\boldsymbol{E}-\boldsymbol{J}$ relation, and are not capable of considering overcritical currents. A widely used alternative is the use of a power law relation as described by Rhyner [47]. Considering equation (6), such choice appears rather naturally as:

$$\boldsymbol{E} = E_c \left|\frac{\boldsymbol{J}}{J_c\,(\boldsymbol{B})}\right|^{n(\boldsymbol{B})} \frac{\boldsymbol{J}}{|\boldsymbol{J}|} \tag{7}$$

where $J_c\,(\boldsymbol{B})$ is the field dependent critical current density, $n(\boldsymbol{B})$, the power law index and $E_c = 1\mu\mathrm{V/cm}$. For consistency with other materials, this $\boldsymbol{E}-\boldsymbol{J}$ relation can be written as

$$\boldsymbol{E} = \rho_{HTS}\boldsymbol{J} \tag{8}$$

where ρ_{HTS}, the mesoscopic resistivity, is given by:

$$\rho_{HTS} = \frac{E_c}{J_c\,(\boldsymbol{B})}\left|\frac{\boldsymbol{J}}{J_c\,(\boldsymbol{B})}\right|^{n(\boldsymbol{B})-1} \tag{9}$$

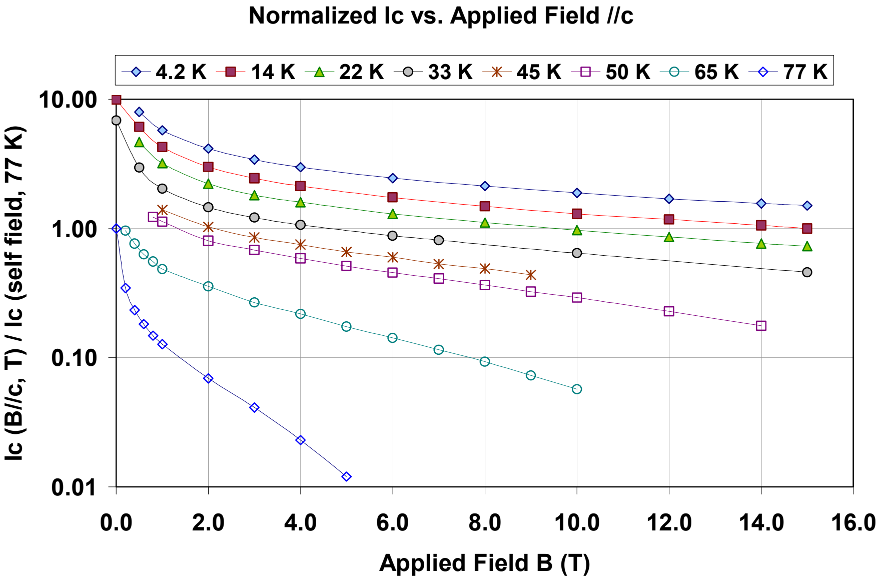

Figure 6. $I_c(\boldsymbol{B})$ curves at several temperatures. Image courtesy of Superpower [18]. The direction //c (parallel to the c-axis of the material) is perpendicular to the tapes surface

Experimental data for the critical current in superconducting wires is presented in Figure 6 Note that while for higher temperatures and lower applied magnetic fields, I_c presents a strong $\boldsymbol{B}$ dependence. On the other hand, at low temperatures and high applied magnetic fields, this dependence is much weaker.

Development of 2G HTS conductors has seen constant developments with increasing critical current densities and overall performance enhance under applied magnetic field [21]. Therefore, every new batch produced has at the least some small change. Dr. Wolfgang Nick gave a humorous analogy on the matter (personal communication, February 7th, 2012): The situation is in a way similar to wine production. A good enologist can tell the make and the year of each wine by tasting a sip of it. In the same way, a good experimentalist could guess the make and the year for a given small sample of a 2G HTS conductor. Although, originally intended as a joke, this situation is true and has serious implications for modeling and simulation as the material properties have to be constantly updated.

Throughout this document, several expressions to describe the critical current density J_c dependence upon the magnetic flux density $\boldsymbol{B}$ will be used. Without loss of generality and considering that $B_{\parallel}$ and $B_{\perp}$ are respectively, the parallel and perpendicular components of the magnetic flux density with respect to the tape's surface, the following expression [48]:

$$J_c(\boldsymbol{B}) = \frac{J_{c_0}}{\left(1 + \frac{\sqrt{k^2 \left|B_{\parallel}\right|^2 + |B_{\perp}|^2}}{B_0}\right)^{\alpha}} \tag{10}$$

will be considered. Here J_{c_0} is the critical current density at zero applied magnetic field; k is a parameter quantifying the anisotropy of the HTS material; B_0 is the characteristic magnetic field and α the exponent of the field dependence. Other relations used in this work can be reduced from (10) by appropriately choosing these material parameters.

2.3 Formulation

During the course of this PhD study some investigations were performed using several models and formulations already used for simulating superconductors, including:

1. The $T - \Omega$ formulation, based on the current vector potential T, and the scalar magnetic potential Ω, as presented by Amemiya et al. [30]
2. The A formulation as presented by Stenvall & Tarhasaari [32] based on the magnetic vector potential.
3. The critical state model based on the magnetic vector potential as presented by Campbell [29].

However, the H-formulation [31] using linear edge elements was chosen for its stability, speed and capability to consider overcritical currents. Early uses of a formulation in the magnetic field H for modeling superconductors can be traced back to Kajikawa et al. [49] and to Pecher et al. [50]. The latter, already used edge elements for performing numerical simulations. Their treatment however does separate the self and applied contributions of the magnetic field. Strategies involving only the physical magnetic field $\boldsymbol{H}$ appear in Hong et al. [51] and Brambilla et al. [31]. A further study made by Nguyen and Ashworth [52], allowed extending the model to consider materials with nonlinear $\boldsymbol{B} - \boldsymbol{H}$ relations. This is the case of roll assisted biaxially textured substrate (RABiTS) 2G HTS tapes, where a magnetic substrate is employed to deposit the YBCO layer. In the end, the formulation described in this work will correspond to the one presented by Brambilla et al. [31] as no separation is made between the self and external fields. However the derivation and justification follows closer to Kajikawa's [49].

For power applications, the low frequency regime can be assumed. Starting from Maxwell's equations, the problem is reduced to calculating the Eddy currents for a material with nonlinear resistivity. Therefore, displacement currents are to be neglected and the Electromagnetic field can be obtained by solving the related Quasi-static problem [53] [54]:

$$\boldsymbol{\nabla} \times \boldsymbol{H} = \boldsymbol{J} \tag{11}$$

$$\boldsymbol{\nabla} \cdot \boldsymbol{B} = \boldsymbol{0} \tag{12}$$

$$\boldsymbol{\nabla} \times \boldsymbol{E} + \frac{\partial \boldsymbol{B}}{\partial t} = \boldsymbol{0} \tag{13}$$

$$\boldsymbol{E} = \rho \boldsymbol{J} \tag{14}$$

$$\boldsymbol{B} = \mu \boldsymbol{H} \tag{15}$$

We start our treatment by substituting the $\boldsymbol{E} - \boldsymbol{J}$ and $\boldsymbol{B} - \boldsymbol{H}$ relations, given in (14) and (15); in Maxwell–Faraday equation (13) and Gauss's law for magnetism (12), yielding:

$$\boldsymbol{\nabla} \times \rho\, \boldsymbol{J} + \frac{\partial(\mu\, \boldsymbol{H})}{\partial t} = \boldsymbol{0} \tag{16}$$

and

$$\boldsymbol{\nabla} \cdot (\mu\, \boldsymbol{H}) = \boldsymbol{0} \tag{17}$$

By restricting the present study to consider only linear magnetic materials, such that $\dot{\mu} = 0$, further substitution of Ampère's circuital law (11) on (16) yields:

$$\boldsymbol{\nabla} \times (\rho \boldsymbol{\nabla} \times \boldsymbol{H}) = -\mu \frac{\partial(\boldsymbol{H})}{\partial t} \tag{18}$$

Note that, in principle, simultaneous solution of equations (17) and (18) yields a problem as it would involve having one too many equations, therefore an alternative procedure must be used. An elegant solution to this issue was presented by Kajikawa et al. [49]. Taking the divergence of equation (18) yields:

$$\nabla \cdot \big(\nabla \times (\rho \nabla \times \boldsymbol{H})\big) = \nabla \cdot \left(-\frac{\partial(\mu \boldsymbol{H})}{\partial t}\right) \tag{19}$$

The left hand side of equation (19) is identically zero. After exchanging the order of time and spatial derivatives it is easy to see that $\nabla \cdot (\mu \boldsymbol{H})$, or alternatively $\nabla \cdot \boldsymbol{B}$, is constant in time. Consequently, if $\nabla \cdot \boldsymbol{B} = 0$ at a given time t_0, then $\nabla \cdot \boldsymbol{B} = 0$, will hold at any other instant. So, if initial conditions are chosen so that $\nabla \cdot (\mu \boldsymbol{H})|_{t=t_0} = 0$

then, it is assured that that $\nabla \cdot (\mu \boldsymbol{H}) = 0$ will hold at all times. Finally, a complete formulation is given by equation (18), initial conditions fulfilling equation (17) and a set of appropriate boundary conditions and/or constraints.

2.4 Several parallel conductors

Consider the cross section of a bundle of conductors – both normal and superconducting materials – surrounded by air. The computational domain of interest Ω is shown in Figure 7. To model a stack or a coil, its cross section is considered and assumed as a bundle of parallel conductors. In the case of a stack, if the conductors are coupled at the ends, transport current can be imposed by means of a Dirichlet condition at the domain boundary $\partial\Omega$. However, for the more general case of a given current being forced in each conductor, as it is for coils or the strands of ROEBEL cables, said Dirichlet condition alone would not suffice. As an example, consider a two layer coaxial cable. Knowing the magnetic field outside the cable does not provide enough information about the currents: any two equal, but opposite currents of any given magnitude would produce a zero magnetic field.

In general, a group of n_c parallel conductors can be considered – each carrying a prescribed current $I_k(t)$, $k \in \{1,2,\dots,n_c\}$. As described by Brambilla et al. [31], one integral constraint per conductor ensures the requirement is met:

$$I_k(t) = \int_{C_k} J\, dA \tag{20}$$

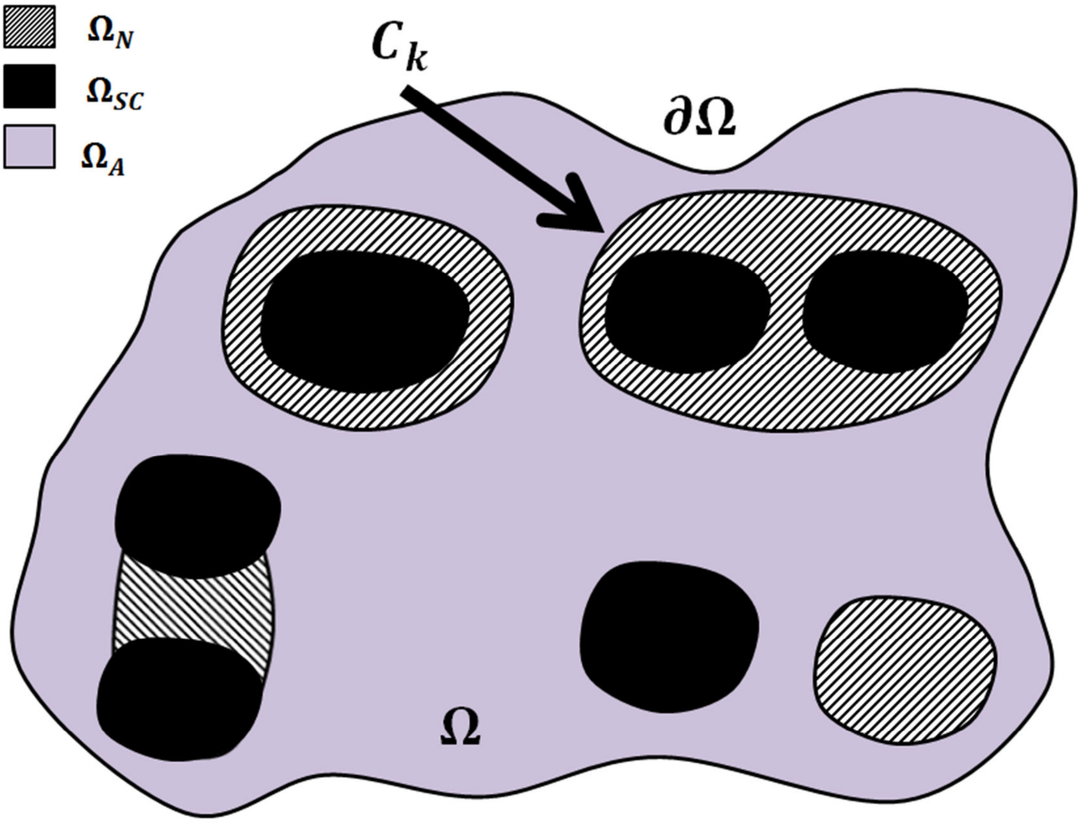

Figure 7. Computational domain $\Omega = \Omega_A \cup \Omega_N \cup \Omega_{SC}$. The superconducting regions are denoted by Ω_{SC}, the normal conductors by Ω_N and the air by Ω_A. Note that neither Ω_{SC} nor Ω_N need to be connected. The arrow points to the kth conductor which carries a net current $I_k(t)$. The boundary of the computational domain is denoted by $\partial\Omega$.

Here, $J = \hat{\boldsymbol{e}}_3 \cdot \nabla \times \boldsymbol{H}$ is the component of the current density in the direction out of the plane and $I_k(t)$, the net transport current in the conductor C_k. Note that in the 2D case considered here, the critical current density $\boldsymbol{J} = \nabla \times \boldsymbol{H}$, has only one non-zero component. If each tape carries the same current $I(t)$ as it is the case for coils or ROEBEL cables, then $\forall k \in \{1,2,\dots,n_c\}$, $I_k(t) = I(t)$. Finally, considering Figure 7 again, the Eddy currents problem is reduced to find $\boldsymbol{H}$ such that:

$$\nabla \times \rho \nabla \times \boldsymbol{H} = -\mu \frac{\partial \boldsymbol{H}}{\partial t} \quad in\ \Omega \tag{21}$$

$$\boldsymbol{H} = \boldsymbol{H}_{self} + \boldsymbol{H}_{ext} \quad on\ \partial\Omega \tag{22}$$

$$I_k(t) = \int_{C_k} J\, dA \quad \forall k \in \{1,2,\dots,n_c\} \tag{23}$$

$$\boldsymbol{H}|_{\boldsymbol{t=0}} = \boldsymbol{H}_0 |\ \nabla \cdot (\mu\, \boldsymbol{H}_0) = \boldsymbol{0} \tag{24}$$

Values for $\boldsymbol{J}$, $\boldsymbol{E}$ and $\boldsymbol{B}$ can be calculated from $\boldsymbol{H}$ using equations (11), (14) and (15) respectively. Finally, calculation of instantaneous AC losses (in W/m) can be achieved by evaluating of the following integral:

$$\xi = \int_S \boldsymbol{E} \cdot \boldsymbol{J} dS \tag{25}$$

For periodic driving signals (either applied magnetic field or transport current), average AC losses (in W/m) can also be calculated by means of the following integral:

$$Q = \frac{1}{T} \int_0^T dt \int_S \boldsymbol{E} \cdot \boldsymbol{J} dS \tag{26}$$

2.5 Simulation

Given the complexity and size of the simulation exercise intended, from the beginning it was decided to use a commercial software package to perform the numerical calculations. In that way, work could be applied to speeding up the computations by modeling rather than by developing numerical algorithms. A couple of software platforms were considered and tested: FlexPDE [55], and COMSOL Multiphysics [56]. Although, FlexPDE provided with the necessary tools to run complex simulations, it lacked built-in edge elements, required to simulate the chosen formulation at manageable computational speeds. On the other hand, besides including edge elements, COMSOL's built-in rotating machinery package made the choice simpler. Therefore no further efforts were invested in creating an electrical generator simulation tool from scratch.

2.6 The Finite Element Method and COMSOL Multiphysics

In this section, a short description of the finite element method is given. Also, a brief explanation of how integral constraints are implemented in COMSOL is provided.

Being COMSOL the chosen software for implementation of the numerical simulations, the treatment presented here follows closely the package's manuals [57] [58] and Zimmerman's work [59]. Although, the description follows a rather general approach, particular attention is given to the Eddy currents problem described in the previous sections. For those purposes, consider again Figure 7. Let equation (21) holds in the set $\Omega \subset \mathbb{R}^2$ with boundary $\partial\Omega$, then, the Eddy currents problem is reduced to find $\boldsymbol{H}$ such that equations (21) through (24) are met. The first step towards solving the problem using finite elements is to express it in weak form. The reminder of this chapter is intended to that end.

For simplicity, the double curl in the left hand side of equation (21) can be transformed using the summation convention as follows:

$$\nabla \times \rho \nabla \times \boldsymbol{H} = \frac{\partial \Gamma_{lj}}{\partial x_j} \hat{\boldsymbol{e}}_l \tag{27}$$

where $\hat{\boldsymbol{e}}_l$ is the l^{th} Cartesian canonical vector and $\Gamma = \rho((\nabla \boldsymbol{H})^T - \nabla \boldsymbol{H})$. Here $\nabla \boldsymbol{H}$, the gradient of $\boldsymbol{H}$, is also the Jacobian matrix of $\boldsymbol{H}$. Therefore using (27), equation (21) can be written as:

$$\frac{\partial \Gamma_{lj}}{\partial x_j} \hat{\boldsymbol{e}}_l = -\mu \frac{\partial \boldsymbol{H}}{\partial t} \quad in\ \Omega \tag{28}$$

Also, Dirichlet boundary conditions (22) can be rewritten as:

$$\boldsymbol{R}^{(1)} = 0 \quad in\ \partial\Omega \tag{29}$$

with

$$\boldsymbol{R}^{(1)} = \boldsymbol{H} - \left(\boldsymbol{H}_{self} + \boldsymbol{H}_{ext}\right) \tag{30}$$

In the same way, integral constraints (23) can be expressed as:

$$\boldsymbol{R}^{(0)} = 0 \tag{31}$$

where $\mathbf{R}^{(0)}$ is a vector with n_c components such that its k^{th} component is:

$$R_k^{(0)} = I_k(t) - \int_{C_k} J\, dA \tag{32}$$

Finally, for simplicity, zero initial values will be chosen, so that $\boldsymbol{H}|_{t=0} = \boldsymbol{0}$. Note however, that this selection fulfills the divergence free requirement in (24). The original problem becomes then finding $\boldsymbol{H}$ such that:

$$\frac{\partial \Gamma_{lj}}{\partial x_j} \hat{\boldsymbol{e}}_l = -\mu \frac{\partial \boldsymbol{H}}{\partial t} \ \ in\ \Omega, \quad \boldsymbol{R}^{(1)} = 0 \ \ on\ \partial\Omega, \quad \boldsymbol{R}^{(0)} = 0, \quad \boldsymbol{H}|_{t=0} = \boldsymbol{0} \tag{33}$$

The Eddy currents problem (33) can readily be rephrased in its weak form representation. Let v – called the vector test function – be a vector whose scalar components are sufficiently smooth and arbitrary functions defined in Ω. Dot multiplying the PDE in (33) by v and integrating on Ω yields:

$$\int_{\Omega} v_l \frac{\partial \Gamma_{lj}}{\partial x_j} \, dA + \int_{\Omega} v_l \mu \frac{\partial H_l}{\partial t} dA = 0 \tag{34}$$

where v_l is the l^{th} component of v and dA the area element. Alternatively, a divergence form for the space derivatives can be used as follows:

$$\int_{\Omega} v_l \, \nabla \cdot \Gamma_l \, dA + \int_{\Omega} v_l \mu \frac{\partial H_l}{\partial t} dA = 0 \tag{35}$$

with Γ_l being the l^{th} row of Γ. After integrating by parts and using Green's formula, yields:

$$\int_{\partial\Omega} v_l \Gamma_l \cdot \boldsymbol{n} ds - \int_{\Omega} \nabla v_l \cdot \Gamma_l dA + \int_{\Omega} v_l \mu \frac{\partial H_l}{\partial t} dA = 0 \tag{36}$$

where ds is the line element and **n** is the normal unitary vector pointing outward of $\partial\Omega$. As no flux source term is present in the boundary, generalized Neumann boundary conditions can be expressed as:

$$-\boldsymbol{n} \cdot \Gamma_l = \frac{\partial R_i^{(1)}}{\partial H_l} \lambda_i^{(1)} \quad on \ \partial\Omega \tag{37}$$

Here, $\mathrm{R}_i^{(1)}$ is the i^{th} component of $\mathbf{R}^{(1)}$, as described in (30), and $\lambda_i^{(1)}$ is the i^{th} Lagrange multiplier. Further substitution of (37) in equation (36) yields:

$$\int_{\partial\Omega} v_l \frac{\partial R_i^{(1)}}{\partial H_l} \lambda_i^{(1)} ds + \int_{\Omega} \left(\nabla v_l \cdot \Gamma_l - v_l \mu \frac{\partial H_l}{\partial t} \right) dA = 0 \tag{38}$$

In this way, the equation is augmented to include the Dirichlet boundary conditions as the introduction of the Lagrange multipliers allows for the simultaneous solution of both (38) and (29). Additional conditions can be added in a similar fashion. For instance, the integral constraints (31) can be included by augmenting (38) with the terms:

$$v_l \frac{\partial R_i^{(0)}}{\partial H_l} \lambda_i^{(0)} \tag{39}$$

Finally, the complete set of equations can be written as:

$$\int_{\partial\Omega} v_l \frac{\partial R_i^{(1)}}{\partial H_l} \lambda_i^{(1)} ds + \int_{\Omega} \left(\nabla v_l \cdot \Gamma_l - v_l \mu \frac{\partial H_l}{\partial t} \right) dA + v_l \frac{\partial R_i^{(0)}}{\partial H_l} \lambda_i^{(0)} = 0 \quad in \ \ \Omega \tag{40}$$

$$\boldsymbol{R}^{(1)} = \boldsymbol{0} \quad on \ \partial\Omega \tag{41}$$

$$\boldsymbol{R}^{(0)} = \boldsymbol{0} \quad on \ \ P \tag{42}$$

where P is a set of n_c mesh nodes used to associate the constraints in (42) with.

Notice that there is no explicit need to solve for the Lagrange multipliers. They are only used to introduce both the Dirichlet boundary conditions and the integral constraints in the weak formulation. Using a variational principle, the Lagrange multipliers can be eliminated. For that purpose, consider the following boundary conditions on the test functions:

$$v_l \frac{\partial R_i^{(0)}}{\partial H_l} = 0 \ \ on\ \partial\Omega \quad and \quad v_l \frac{\partial R_i^{(1)}}{\partial H_l} = 0 \ \ on\ P \tag{43}$$

After substituting (43) in (40), then the problem reduces to finding functions H_l such that:

$$\int_\Omega \left(\nabla v_l \cdot \Gamma_l - v_l \mu \frac{\partial H_l}{\partial t} \right) dA = 0 \quad in \ \ \Omega \tag{44}$$

$$\boldsymbol{R}^{(\mathbf{1})} = \mathbf{0} \quad on\ \partial\Omega \tag{45}$$

$$\boldsymbol{R}^{(\mathbf{0})} = \mathbf{0} \quad on \ \ P \tag{46}$$

For all test functions fulfilling conditions (43).

Equation system (44)-(46) can now be easily discretized. Using finite elements and basis functions, both the dependent variables H_l and the test functions v_l can be approximated as follows:

$$H_l = U_i\, \phi_i^{(l)} \tag{47}$$

and

$$v_l = V_i\, \phi_i^{(l)} \tag{48}$$

where U_i and V_i are the vectors of unknowns and $\phi_i^{(l)}$ are the basis functions related to the variable v_l. Basis functions are used to represent the dependent variable in a discrete way. In that sense, a mesh discretization of the space domain can be used. Each basis function has support only in one element. In this work two types of basis functions were used. Quadratic Lagrange elements are already implemented as part of the AC/DC module of COMSOL that was used to simulate the generator. For the H-formulation described above, linear edge elements were used.

Note, that equation (44) is linear in the test functions v_l. Then, if (44) is fulfilled for each basis function $\phi_i^{(l)}$, such that $v_l = \phi_i^{(l)}$, it will be satisfied for $v_l = V_i\, \phi_i^{(l)}$, a linear combination of them. Hence, after substituting the corresponding finite element approximations the discretization of the weak equation (44) is:

$$L\big(\boldsymbol{U}, \dot{\boldsymbol{U}}, t\big) = 0 \tag{49}$$

where $\boldsymbol{U}$ is the vector of unknowns U_i. The integrands in (49) are calculated using a numerical quadrature formula. A similar discretization procedure can be used for the constraints $\mathbf{R}^{(\mathbf{0})}$ and $\mathbf{R}^{(\mathbf{1})}$ in (45)-(46). Collecting these constraints together yields:

$$M(\boldsymbol{U}, t) = 0 \tag{50}$$

Finally, the problem is reduced to solving the Differential Algebraic System (49)-(50) in the unknown vector $\boldsymbol{U}$. This is accomplished by the IDA solver [60] implemented in COMSOL. This solver uses variable-order variable-step-size backward differentiation formulas. Furthermore, the IDA solver is equipped with a Newton solver, so that the nonlinear equations can be solved [57].

Chapter 3 Stacks and coils

This chapter explains the importance of modeling and simulation of HTS stacks as a building block for large scale applications such as cables, coils and rotating machinery. Some of the current challenges are exposed and a proposed strategy based upon the use of structured meshes is compared against previously published results showing good agreement. The method is further used for performing calculations in racetrack coils. The content of this chapter follows closely the works presented at the COMSOL 2009 conference held in Milan, the Applied Superconductivity Conference 2010 held in Washington DC; and three subsequent publications [61] [62] [63], all of which are included in appendixes A, B and C, respectively.

3.1 Importance of 2G HTS stacks

At the moment, motors, generators, transformers and large magnets are designed and/or built taking advantage of the high magnetic field achieved by superconducting coils in compact designs. In the same manner, superconducting cables such as the increasingly popular ROEBEL are being used for their high current capacity [64] [65]. Although some of these devices are designed so that their superconducting elements do not experience AC electric currents or magnetic fields, heating losses are expected during transient responses. Furthermore, transformers, asynchronous rotating machinery, and cables carrying AC currents are inherently burdened by hysteretic losses. Understanding and calculating these losses is fundamental for performance evaluation and design. As mentioned in chapter 1, in the particular case of a synchronous generator, AC losses in the rotor windings are not expected during normal operation. However, transient losses could emerge due to mechanical torque or electric load signals change.

The cross section of racetrack coils, as the ones conforming radial flux electric motors or generators, can be modeled as a couple of stacks transporting current in opposite directions. Pancake (circular) coils can be treated in a similar way for the case of sufficiently large internal radius. Finally, ROEBEL cables can be modeled as two parallel stacks of tapes where all the strands carry the same net current [64]. Hence, calculation of AC losses in large scale HTS devices typically boils down to computing the equivalent Eddy currents problem for stacks of tapes that are subjected to transport current.

Modeling and simulation of the AC response of HTS stacks has shown to be a cumbersome task. It has already been the subject of study by means of: integral equations using a thin conductor approximation [36]; anisotropic homogenous-medium approximations [39] [40] [41]; and 2D numerical solution of either partial differential equations [37] or quasi-variational inequalities [38] detailing the actual layout of just a few conductors.

Use of integral equations has demonstrated to provide fast solutions for the limiting cases where the configuration of the problem at hand can be reduced to solve one or two equations like for infinite stacks or windings [36]. However, for the general case of a finite stack, the number of equations will increase proportionally with the number of conductors. Use of nonlocal operators will likely imply having a fully coupled matrix in the numerical solution process by finite elements. Hence, the computational time involved in simulation of finite stacks will become much of a burden for cases involving more than a handful of conductors.

In the previous chapter, the strategy for 2D finite element solution of the PDEs describing the equivalent Eddy currents problem for a bundle of superconducting wires was already discussed. However, the large aspect ratio of 2G HTS tapes has become a matter of concern for the purpose of numerical simulations [36] [66]. Use of regular meshes with elements' aspect ratio close to unity produce a large number of degrees of freedom as the thin layers in the coated conductors require many of such elements. The superconducting layer of commercially available 2G HTS coated conductors presents aspects ratios in the order of 10^3 to 10^4. Hence, discretization of the layers in the coated conductor will be affected by this factor. Simulation of several conductors then proved to be a rather unmanageable task.

To overcome this issue without leaving the 2D modeling frame, a strategy involving the implementation of geometries with lower aspect ratios along with a scaled current density value was recently proposed [66]. Nevertheless, the problem persists as the aforementioned method is based upon extrapolation of calculations for lower aspect ratio domains.

The large aspect ratio of the thin films in coated conductors shows the multiscale nature of the layout: thickness and width are in different spatial scales. In the coming sections a strategy to simulate superconductors in a timely effective manner is presented. The simulation is based on the H-formulation as described in the previous chapter. As it will be shown, the use of this multiscale approach allows for simulation of stacks for many applications rapidly and with ease. The case for the anisotropic homogenous-medium approximations will be discussed in the next chapter, where the further improvements will be presented.

3.2 Structured (mapped) meshes

Typical free meshing techniques use mesh elements with aspect ratio close to unity to discretize a domain [67], hence avoiding elongated elements. Their use in discretizing thin layers poses a significant drawback. This is due to the fact that the number of elements increases heavily with the growing aspect ratio of the layer. As a result, the number of degrees of freedom is augmented and so is the computing time. This is of large importance while simulating 2G HTS coated conductors since the aspect ratio of the superconducting layer can be as high as 10^4.

This big aspect ratio in the conductor layer's width/thickness can be dealt with by means of a multiscale mesh. Up to some degree, the aspect ratio of such mesh elements should resemble the conductor's own aspect ratio and overall shape. This purpose is fulfilled by use of structured (mapped) meshes.

In this work, rectangular structured meshes were used to discretize all non-Air domains. Although the optimal aspect ratio for the mesh elements was not investigated, aspect ratios in excess of 100 provided good results. Structured meshes were implemented in all thin layers, allowing for 75 elements for the width and two (or four) for the thickness of each layer. Therefore, aspect ratios of 80 (or 160) were obtained for the mesh elements. Figure 8 shows a comparison of both free and structured meshing approaches. Use of free meshes required 17150 elements to discretize the thin layer shown. At the same time, only 150 were necessary while using mapped meshes. A reduction in excess to 3 orders of magnitude for the number of elements was achieved just for the superconducting strip. Furthermore, notice that the area around the layer also experienced a significant mesh reduction. This translates to an overall significant reduction in the number of unknowns and therefore in a computational speedup.

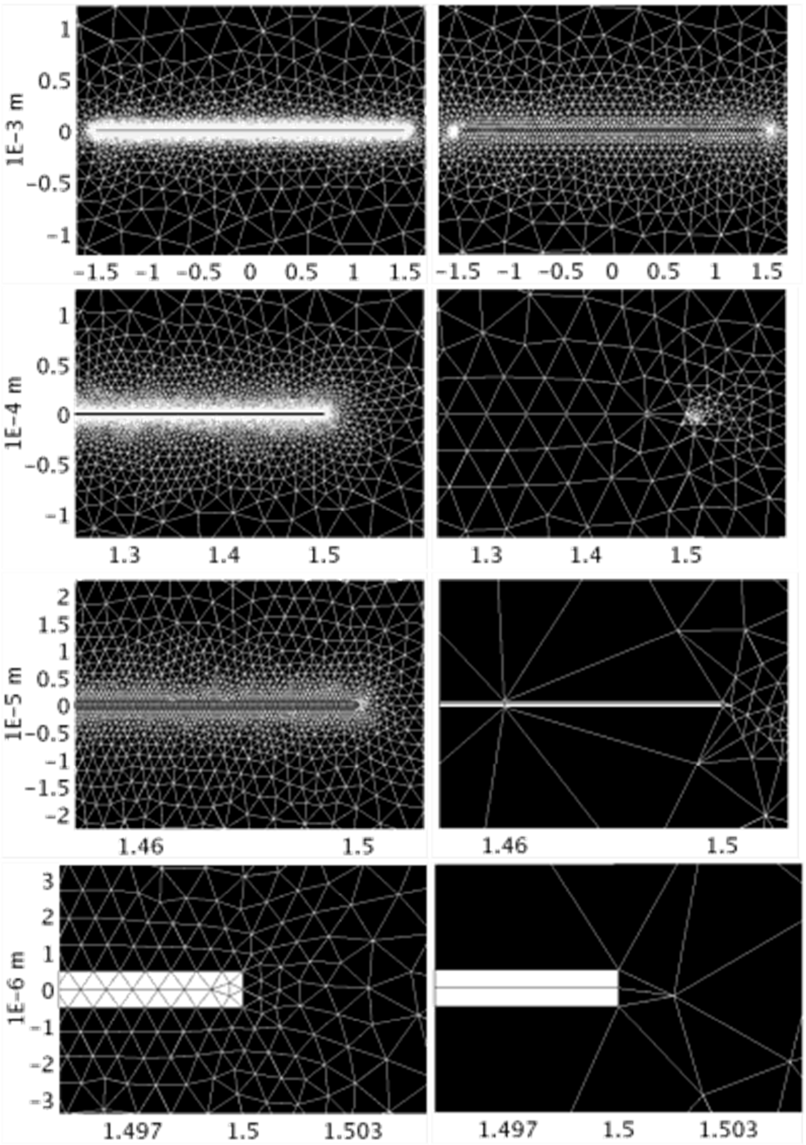
1E-3 m
1
0.5
0
-0.5
-1
-1.5 -1 -0.5 0 0.5 1 1.5
-1.5 -1 -0.5 0 0.5 1 1.5
1E-4 m
1
0.5
0
-0.5
-1
1.3 1.4 1.5
1.3 1.4 1.5
1E-5 m
2
1.5
1
0.5
0
-0.5
-1
-1.5
-2
1.46 1.5
1.46 1.5
1E-6 m
3
2
1
0
-1
-2
-3
1.497 1.5 1.503
1.497 1.5 1.503

Figure 8. Consecutive zoom views of the mesh in and around a superconducting strip of 3 mm by 1 µm [62]. The horizontal scale in all subfigures is in mm. *Left column:* using free meshes, with elements' aspect ratio close to unity, 17150 elements were needed for the superconducting region using 2 elements to discretize the thickness of the layer. *Right column:* using mapped meshes only 150 were necessary for the same purpose.

3.3 Validation

To test the proposed meshing technique, the cases of transport current and applied external field were considered just as presented by Brambilla et al. [28]. AC losses were calculated for a superconducting strip of 3 mm of width and thickness of 1 µm. The critical current J_c, and the power law exponent n, were assumed constants with values of 10^{10} A/m^2 and 25, respectively. For the air (or vacuum) surrounding the conductor, a finite resistivity of 1 Ω·m was used. A relative permeability equal to 1 was assumed for both air and the superconducting domains. All transport currents and externally applied fields were sinusoidal signals with frequency of 50 Hz. The comparison of the calculated values for several applied fields and transport currents is shown in Figure 9.

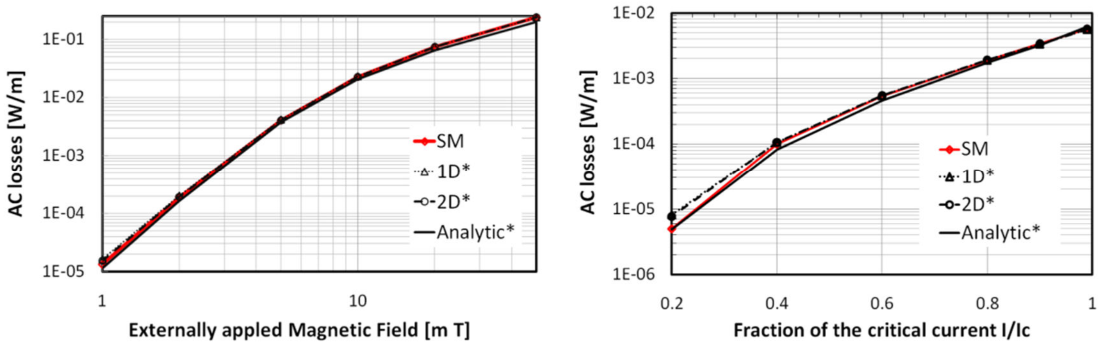

Figure 9. Comparison of calculated AC losses for several values of externally applied AC Magnetic Field (left) and of transport current (right) [62]. The SM label corresponds to the calculations made with the proposed discretization using structured meshes and the labels with the symbol * to published results in Brambilla et al. [28].

Note that for both cases considered, the numerical results are in good agreement with the previously published numerical computations. Only in the case of small current fractions a difference is seen when compared to the 1D model. However, this issue is considered to be a drawback of the 1D model [68] as both 2D computations match. Overall, it is seen that no accuracy is compromised when structured meshes are used as compared to other 2D methods using free meshes with elements' aspect ratio close to unity. To test the speed performance of both strategies, comparison of the computing time reported by Brambilla et al. [28] is shown in Figure 10.

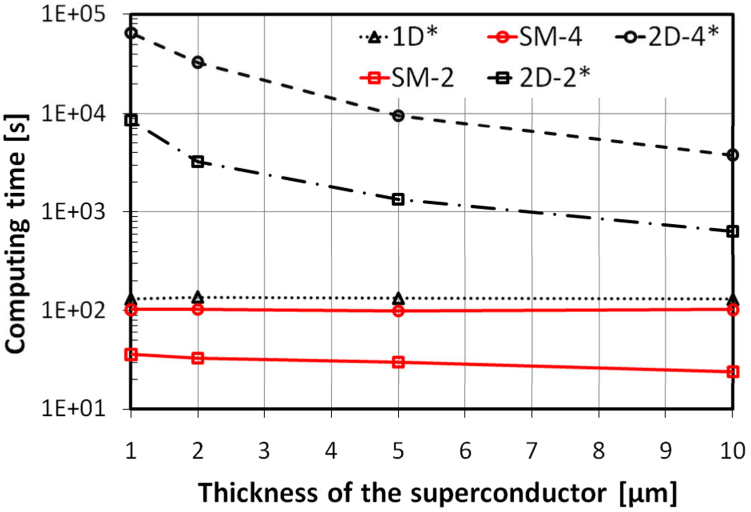

Figure 10. Computing time for a full cycle at 50 Hz [62]. The SM-2 and SM-4 curves refer to calculations made with the proposed discretization using structured meshes with 2 or 4 elements across the thickness respectively. The labels with the symbol * correspond to published results [28] for 1D models, and for 2D models with 2 and 4 mesh elements across the thickness.

It is relevant to point out that the use of mapped meshes allowed for calculations to be performed two to three orders of magnitude faster than with regular free meshing for full 2D simulations. The computational speed up is more significant for thin layers in the order of 1 μm as the ones used in commercially available 2G HTS coated conductors. Furthermore, calculations using mapped meshes with two and four elements used across the thickness were up to five times faster than the reported computing time for the 1D formulation. Therefore, using structured meshes, a fast and accurate approach has been implemented to calculate AC losses in superconducting thin layers.

3.4 Simulation of a racetrack coil

To illustrate the potential of the method presented, one of the racetrack coils of the Superwind project [69] was considered. The coil is composed of 57 turns of the commercially available Copper Laminated Amperium Wire from American Superconductor [70]. Figure 11 shows the actual architecture of the coil along with its corresponding modeled cross section along with successive zooms of the geometry used to perform simulations. The true thickness of the 1μm superconducting layer was taken into account. For simplicity and taking advantage of the symmetry, only one quarter of the cross section of the coil was simulated.

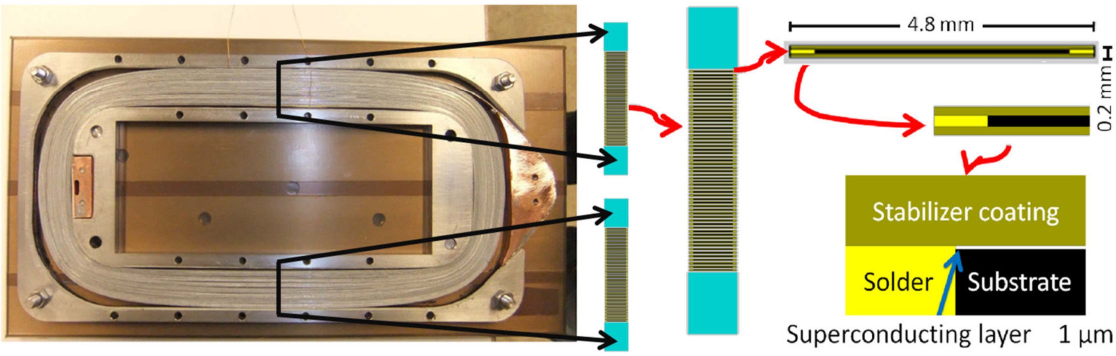

Figure 11. *Left:* Racetrack coil from the Superwind project [69]. *Right:* geometrical representation used to model the cross section of the coil [62]. Note that the actual topology (up to the μm scale) of the layered media in the 2G HTS coated conductors is considered.

In a first simulation, an AC current of 65.8 A, at 50 Hz was imposed to each of the 57 tapes in a vertical stack. While the thickness of each tape was 0.2 mm, the stack was 2 cm high, hence allowing for insulation and/or air among tapes. Values for the power law exponent n and the critical current density J_c of 21 and 2.375×10^{10} A/m^2, respectively were used. This corresponded to a critical current I_c of 95 A in a single tape. Values for the resistivity of the hardened copper coating (6 nΩ·m), solder (30 nΩ·m) and substrate (65 nΩ·m) were obtained from Nam et al. (2007). An operating temperature of 77 K was assumed. In this first study, the nonlinear permeability of the substrate was not considered [62]. However, a latter study for 2 parallel racetrack coils, each composed of 50 turns, included such property [63]. In what follows the substrate will be considered to be non-magnetic for consistency with the upcoming chapters. This corresponds to the case of 2G HTS tapes manufactured using the Ion Bean Assisted Deposition technique (IBAD) as the commercially available Superpower wires [18].

The magnetic field $\boldsymbol{H}$, for the whole cross section of the coil at peak current value is presented in Figure 12. Also, successive plots at different phase values are shown to depict a half AC cycle. For simplicity in comparison, only one quarter of the cross section of the whole coil is presented. Particularly, notice how the magnetic field is trapped inside the coil at both phase values of π and 2π (when the net current of each turn of the coil is zero). This is due to the remnant current profiles inside the superconducting layers.

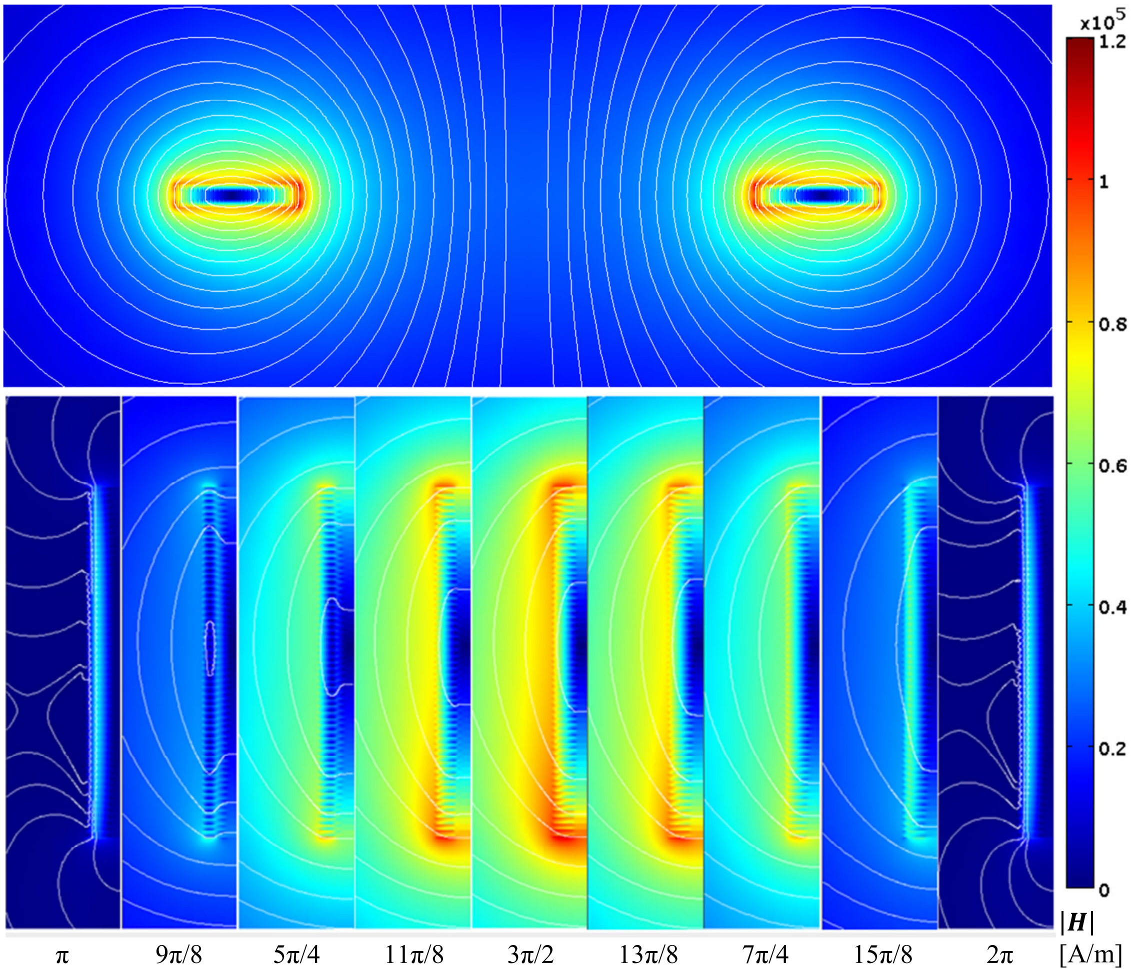

Figure 12. *Top:* magnetic field magnitude $|\boldsymbol{H}|$ [A/m] for the cross section of the coil at peak current value [62]. The stream lines show the magnetic field lines. For a better visualization, the geometric features such as domain edges were not plotted. *Bottom:* detailed cross sectional plots at different phase values. From π to 2π in π/8 increments (from left to right).

Although computational times changed depending on the fraction of the critical current imposed, simulation of a whole AC cycle was done well under 6 hours.

To study the effect of a non-constant value for the critical current density J_c, a second simulation was performed. The following empiric relation for the $\boldsymbol{B}$ dependence of the critical current $I_c(\boldsymbol{B})$, of a single tape was used:

$$I_c(\boldsymbol{B}) = \frac{1}{a + b|B_\perp|} \tag{51}$$

here, $a = 0.0104\, A^{-1}$, $b = 0.043\, \mathrm{T}^{-1} A^{-1}$ and $B_\perp$ is the component of the magnetic field perpendicular to the tape's surface. This relation was scaled to represent the $\boldsymbol{B}$ dependent value for the critical current density of the superconducting material as follows:

$$J_c(\boldsymbol{B}) = \frac{1/S_{HTS}}{a + b|B_\perp|} \tag{52}$$

where S_{HTS} is the surface area of the superconducting layer's cross section of a tape.
Although no significant differences were observed for the magnetic field profile in the coil with the new J_c characteristic, the overall current distribution in the

superconductors presented some changes. Figure 13 shows the normalized current density J/J_c in the tapes of the coil for the two considered cases. Note that when the $J_c(\boldsymbol{B})$ dependence is used, the current penetrates deeper into the stack. Recall that the net current flowing in each strand of the stack is the same for both examples (65.8 A, at 50 Hz). Also, the collective current profiles of the tapes for the case of $J_c(\boldsymbol{B})$ show a narrower "dog biscuit" like shape.

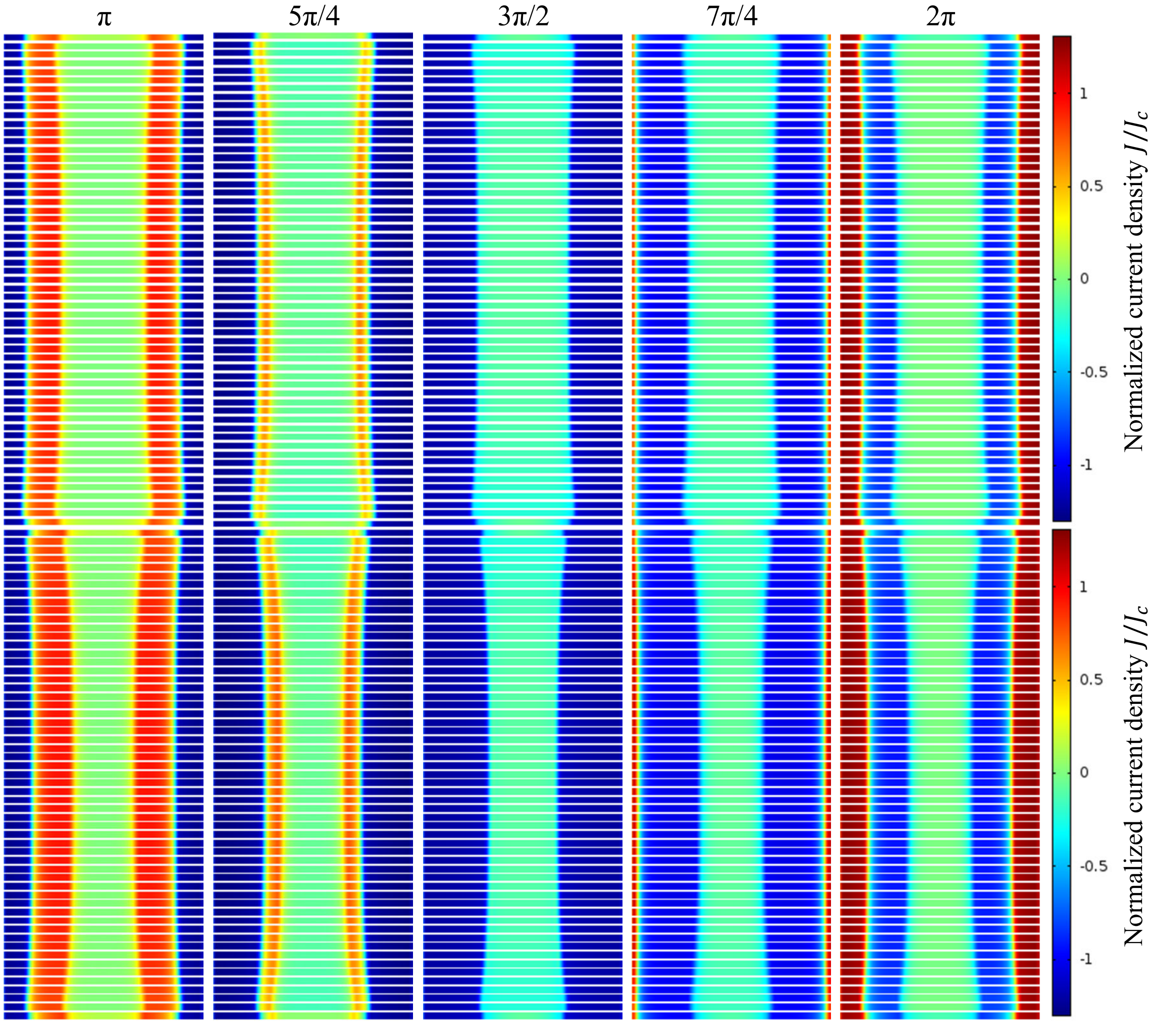

Figure 13. Normalized current density J/J_c. Top: considering a constant J_c value. Bottom: considering $J_c(\boldsymbol{B})$ as in equation (52). Results shown at different phase values: from π to 2π in π/4 increments (from left to right). For visualization purposes, only data for the superconducting layers' is plotted; the superconducting layers' actual thickness is artificially expanded in the vertical direction and the aspect ratio of the coil is halved. The actual width of the superconducting layers is 4 mm while the height of the stack is 2 cm.

The difference in the current density profiles of the tapes can be better understood by considering the normalized critical current density $J_c(\boldsymbol{B})/J_c(\boldsymbol{0})$ as shown in Figure 14. Notice that, at peak net current, the critical current density of the tapes in the stack drops below 75% of its zero field value $J_c(\boldsymbol{0})$ on the stack sides. Therefore, the current has to penetrate deeper into the superconducting layers to accommodate the desired net transport current as already shown in Figure 13. The pattern in the normalized critical current density $J_c(\boldsymbol{B})/J_c(\boldsymbol{0})$ can be compared to the magnetic field $\boldsymbol{H}$ already shown in Figure 12. Note that for a phase value of 3π/2, the magnetic field lines lie perpendicular to the tapes surface, hence minimizing the $J_c(\boldsymbol{B})$ value as defined in equation (52). Overall, as it would be expected, the local minima for $J_c(\boldsymbol{B})$ correspond to the interfacial regions of positive and negative current density.

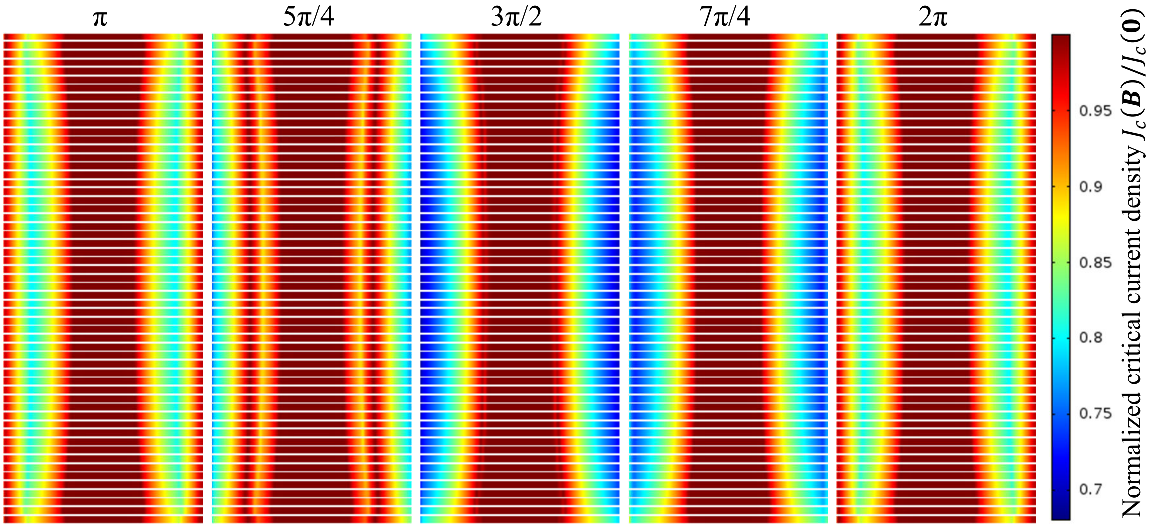

Figure 14. Normalized critical current density $J_c(\boldsymbol{B})/J_c(\boldsymbol{0})$ as in equation (52). Results shown at different phase values: from π to 2π in π/4 increments (from left to right). For visualization purposes, only data for the superconducting layers' is plotted; the superconducting layers' actual thickness is artificially expanded in the vertical direction and the aspect ratio of the coil is halved. The actual width of the superconducting layers is 4 mm while the height of the stack is 2cm.

3.5 Calculation of AC Losses

The energy loss Q (in J/cycle/m) was calculated for several net transport currents expressed as a fraction of the critical current I/I_c. Again, both cases considering the critical current density as a constant and as dependent of the magnetic flux density were studied. The obtained values (in J/cycle/m) are presented in Figure 15.

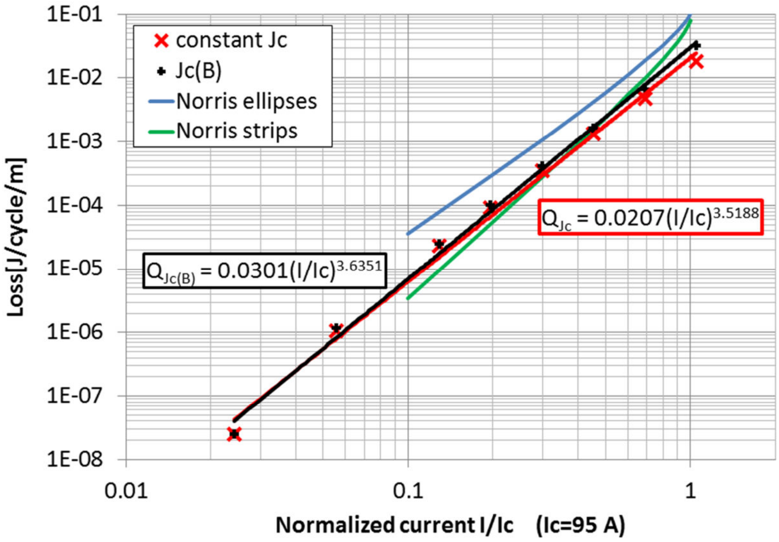

Figure 15. AC losses for several net transport currents expressed as fraction of the critical current $I_c = 95A$. Included, power law fits, $Q_{J_c}$and $Q_{J_{c(\boldsymbol{B})}}$ for both constant and $\boldsymbol{B}$ dependent critical current densities, respectively. For comparison, Norris' expressions for both ellipses and strips are also plotted. For Norris' expressions, the losses of one isolated conductor were scaled by the number of tapes in the stack.

Although both approaches present a similar behavior, the losses for a constant J_c are lower. Norris' expressions [71] for both ellipses and strips are also plotted for comparison with the obtained results. Exponents in the range 3.5-3.6 have been obtained and are in qualitative agreement with the analytical expressions for isolated conductors. Additional losses should be expected from the magnetic substrate, which as mentioned earlier were not considered here. For such analysis, the reader is directed to [63] were such effects were included.

3.6 Conclusion

The use of structured (mapped) meshes with large aspect ratio elements allowed simulating the electromagnetic properties of superconducting materials in thin geometries faster than when using free meshes. Both transport and applied field cases were studied. No significant accuracy compromise in the calculation of AC losses was observed in either case. For a single conductor, computational time was reduced by 2 to 3 orders of magnitude. Although further studies upon finding an optimal mesh distribution are yet to be performed, aspect ratio values of 80 and 160 for the mesh elements used in this work provided results consistent with previously published data.

Use of the proposed method allowed calculating AC losses in fairly large coated conductor problems with ease and within manageable time. This allows thinking about design optimization or simulations of further applications like large magnets or superconducting motors and generators in the near future as it is the main goal of this study.

Chapter 4 Homogenization

The last tool developed during the course of this PhD study leading to the simulation of an HTS generator is presented in this chapter. The underlying idea is to find a homogenized equivalent for the stack of tapes. This can be thought of as “washing out” the geometric internal features of the stack while keeping its overall electromagnetic behavior. The starting point of the analysis is in the previously published models considering this problem. The models are described and emphasis is made upon the choice of assumptions in each case. The model presented here relies on none of the aforementioned assumptions, thus providing with a more general scope. The proposed strategy is then validated by comparison with full scale 2D simulations, where good agreement is shown. Using this method, speedup of about 2 orders of magnitude was achieved for the simulation of a stack of 64 tapes.

4.1 Challenges in 2D formulations

In the previous chapter, a strategy for speeding up the calculation of AC losses in stacks of 2G HTS coated conductors using 2D finite element simulations was presented. The fastest approach in this sense relied upon the use of structured meshes. Overall, computational speed was increased by 2 to 3 orders of magnitude when compared to other 2D strategies and even performed faster than 1D formulations relying on integral equations. Despite all aforementioned improvements, the calculation time for one AC cycle of transport current in a racetrack coil of 57 turns was reported to be about 6 hours [62]. Large scale applications will typically require computation of larger stacks for longer periods of time, far exceeding the duration of an AC cycle. Furthermore, as the number of conductors increase, the numerical burden of performing simulations does so accordingly and computational time scales up. Therefore further improvements are necessary for speeding up computations.

4.2 State of the art

Several works have already modeled a stack of tapes as an anisotropic homogenous bulk. In a first work, Clem et al. [39] adhered to the following assumptions:

1. The critical current density J_c of the superconducting layer is constant.
2. Considering a stack as the one in Figure 16, the magnetic field is parallel to the tapes surfaces inside the subcritical region of the equivalent anisotropic bulk model. Therefore in that region, it can be assumed that $\partial J/\partial \mathrm{x} = 0$ (the current density does not depend on x).
3. The boundary between the critical and subcritical zones can be approximated with a straight line perpendicular to the tapes surfaces.

In a further work by Yuan et al. [40] this first assumption is discarded by allowing a Kim like model for the critical current density $J_c(\boldsymbol{B})$ dependence on the magnetic field $\boldsymbol{B}$. Although the second assumption is kept, the third is improved by using parabolas to fit the boundary between the critical and subcritical zones. More recently, a further model was presented by Prigozhin and Sokolovsky [41]. Their model for the anisotropic bulk limit, based on a quasi-variational inequality formulation, does not rely on any assumptions for the shape of boundaries separating the critical and subcritical zones in the stack. However, this formulation is based upon the critical state model using a Kim-like $Jc(\boldsymbol{B})$ dependence [46]. Hence, it assumes a zero electric field

$\boldsymbol{E}$ for all subcritical regions and does not allow for considering overcritical local currents.

4.3 Modeling Strategy

In the following sections, a further generalization for the anisotropic bulk model is described where none of the aforementioned assumptions is considered. The treatment is based upon the popular H-formulation using edge elements [31] as described in chapter 2 using a power law to describe the $\boldsymbol{E}-\boldsymbol{J}$ relationship. An scaled Kim-like model is used to characterize the $J_c(\boldsymbol{B})$ dependence. All calculations are implemented in the commercially available FEM software package COMSOL. The model for the homogenized stack is compared to a fully featured stack of tapes to evaluate the accuracy of the proposed method. Furthermore, the method presented here can also be used for ROEBEL cables, and pancake and racetrack coils given appropriate boundary conditions.

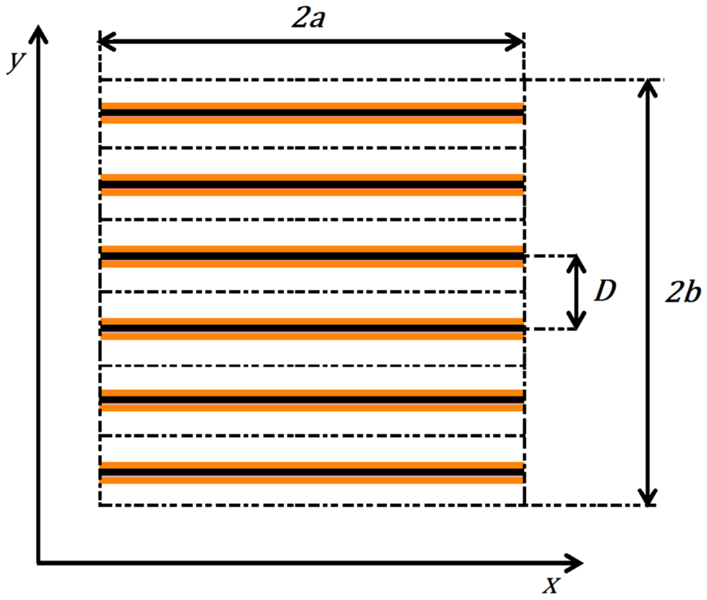

Figure 16. Cross section of the idealized stack of tapes considered. The transport current flows in the z direction (out of plane). The stack's height is denoted by $2b$, its width by $2a$ and the distance among tapes by D. Hence the number of tapes n_c is given by $n_c = 2b/D$.

4.4 Formulation

Consider the vertical stack of 2G HTS tapes as described in Figure 16. Although in a real application, the separation between the tapes D, could be a packing quality parameter changing throughout the stack, it will be considered constant in this study. The stack in Figure 17 shows a representation of the stack as a periodic linear array of unit cells. Up to the µm scale, this layout corresponds to a 2G HTS coated conductor as the one developed by Superpower [18]. A unit cell then, will be composed of layers of copper, silver, YBCO, substrate and the air/insulation separating it from the next tape. In order to consider an anisotropic bulk model, the actual topological features of the tapes are then "washed out". Therefore, material parameters have to be modified accordingly.

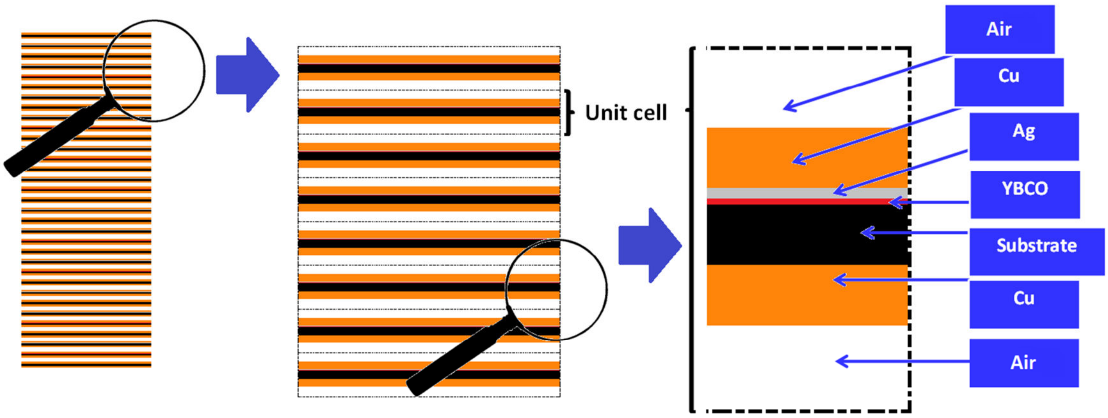

Figure 17. Stack of conductors as a periodic array of unit cells. The zoomed image (*right*) shows the internal layered structure of each unit cell.

Typical resistivity values of normal conductors are several orders of magnitude bigger than their corresponding counterparts for superconductors in the mixed state. For this reason, in the homogenization process only the superconductor and the vacuum will be considered.

The Kim like model for the $J_c(\boldsymbol{B})$ dependence has to be modified so that it is accordingly expressed in the homogeneous case. This is easily achieved by using the equivalent engineering critical current density $J_{c,Eq}(\boldsymbol{B}) = J_c(\boldsymbol{B})f_{HTS}$, where f_{HTS} is the volume fraction of the superconducting material per unit cell. Hence, following from Thakur et al. [48], the equivalent $J_{c,Eq}(\boldsymbol{B})$ dependence is given by:

$$J_{c,Eq}(\boldsymbol{B}) = \frac{J_{c_0} f_{HTS}}{\left(1 + \frac{\sqrt{k^2|B_\parallel|^2 + |B_\perp|^2}}{B_0}\right)^{\alpha}} \tag{53}$$

where $B_0 = 42.65\ \mathrm{mT}, J_{c_0} = 28\ \mathrm{GA/m^2}$, $k = 0.29515$, $\alpha = 0.7$, and $B_\parallel$ and $B_\perp$ are respectively, the parallel and perpendicular components of the magnetic flux density with respect to the tape's surface. In what follows and for ease, J_c alone will refer to the equivalent engineering critical current density $J_{c,Eq}(\boldsymbol{B})$ in the case of a homogenized stack and to $J_c(\boldsymbol{B})$ in the case of the superconducting layers of a tape.

2G HTS tapes manufactured using the Ion beam assisted deposition technique (IBAD), such as the commercially available wires manufactured by SuperPower [18] do not employ magnetic materials. Therefore, the relative permeability of the various layers is considered equal to one. Hence no homogenization is required for this material parameter.

The next step in considering the anisotropic bulk model is to use the Eddy currents problem derived in the previous chapter and adapt it for the homogenized case. Again, the start point will be the H-formulation. The governing equation, boundary conditions and initial values are as described in equations (21), (22) and (24). However, the integral constraints (23) need to be modified so that the use of a homogenized domain can be implemented. Although, described here in more detail, the new integral constraints follow from the previously mentioned pioneering work by Clem et al. [39].

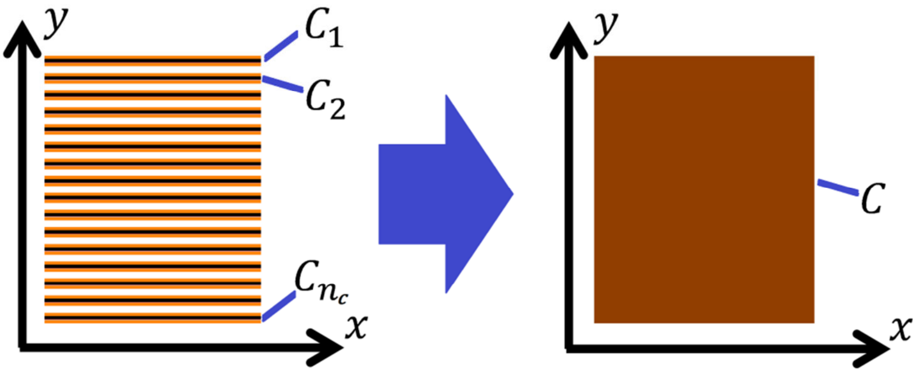

Figure 18. Homogenizing a stack of tapes. The labels $C_1, C_2, \dots, C_{n_c}$ and C denote each of the tapes in the actual stack (*left*), and the homogeneous-medium equivalent (*right*), respectively.

Recall from the discussion in chapter 2, that to model a stack of n_c conductors, each carrying a prescribed current $I_k(t)$ $\forall k \in \{1,2,\dots,n_c\}$, one constraint per conductor C_k ensured the requirement was met:

$$I_k(t) = \int_{C_k} J(x,y,t)dxdy \qquad \forall k \in \{1,2,\dots,n_c\} \tag{54}$$

However, the use of a homogenized domain for an anisotropic bulk model as shown in the right half of Figure 18, does not allow for implementing the integral constraints described. Hence, a new constraint will be required to assure the intended transport current. In the limiting case of a tightly packed stack composed by infinitely thin conductors, this condition can be expressed as:

$$K(y,t) = \int_C J(x,y,t)dx \tag{55}$$

here, $K(\tilde{y},t)$ is the current density per height transported by the thin conductor at $y = \tilde{y}$ in the stack C. Clearly, an interpolation function can provide with an estimate for $K(y,t)$ in terms of the $I_k(t)$ constraints for the general case (each tape carrying a different current). In the situation when all tapes transport the same current $I(t)$, such relationship takes the much simpler form:

$$K(y,t) = \frac{I(t)}{D} \tag{56}$$

4.5 Validation strategy

To validate the proposed strategy, parallel simulations were carried out. A first simulation, following the methodology described in the previous chapter, considered a fully featured stack where all layers (up to the µm scale) are included. The second simulation relied on the homogenization technique proposed here. In both cases, stacks of 16, 32 and 64 tapes were considered. Furthermore, both magnetization and transport current events were studied.

For the transport current case, AC currents at 50 Hz were imposed to each of the tapes in the vertical stacks. Amplitudes of the applied currents were 70 A, 60 A and 50 A for the stacks of 16, 32 and 64 tapes, respectively. For the magnetization case, vertical AC magnetic fields at 50 Hz were applied to each stack. Amplitudes of the applied magnetic fields were 90 mT, 100 mT and 110 mT for the stacks of 16, 32 and 64 tapes, respectively.

Structured meshes were used for the original stacks, just as described in the previous chapter. Although other meshes were also considered for the anisotropic bulk, the results presented here correspond to structured rectangular meshes as rough as 19X50 elements for the whole bulk domain. Unless otherwise stated, the remaining parameter values used in the simulations are as presented in Table 1. These correspond to the commercially available 2G HTS tapes manufactured by Superpower [18].

Parameter	Value	Description
h_I	200 µm	Insulation/Air layer thickness
h_{Cu}	40 µm	Copper layer thickness
h_S	50 µm	Substrate layer thickness
h_{Ag}	2 µm	Silver layer thickness
h_{HTS}	1 µm	YBCO layer thickness
D	293 µm	Unit cell thickness
a	2 mm	Tape half width
ρ_{Ins}	1 Ω·m	Insulation/Air resistivity
ρ_{Ag}	2.70 nΩ·m	Silver resistivity [72]
ρ_{Cu}	1.97 nΩ·m	Copper resistivity [72]
ρ_{Subs}	1.25 µΩ·m	Substrate resistivity [73]
n	38	Power-law exponent
E_c	10^{-4} V/m	Electric field at critical Current

Table 1. Parameter values used for simulations.

4.6 Transport current

Figure 19 shows the magnetic flux density for half AC cycle in both an original stack of 32 tapes and its anisotropic bulk model representation for the transport current case studied. The normalized critical current density J/J_c is presented in Figure 20, where the "dog biscuit" like shape for the boundary of the critical and subcritical zones appear in both cases. In general, the profiles for both magnetic flux density and normalized critical current J/J_c in the original stack are reproduced by the anisotropic bulk model. Also, since a power law was used for the $\boldsymbol{E}-\boldsymbol{J}$ relation, local overcritical current values are reached as seen in Figure 20. As reported by Tharkur et al [48], this is expected to have an impact in the critical current of the stack.

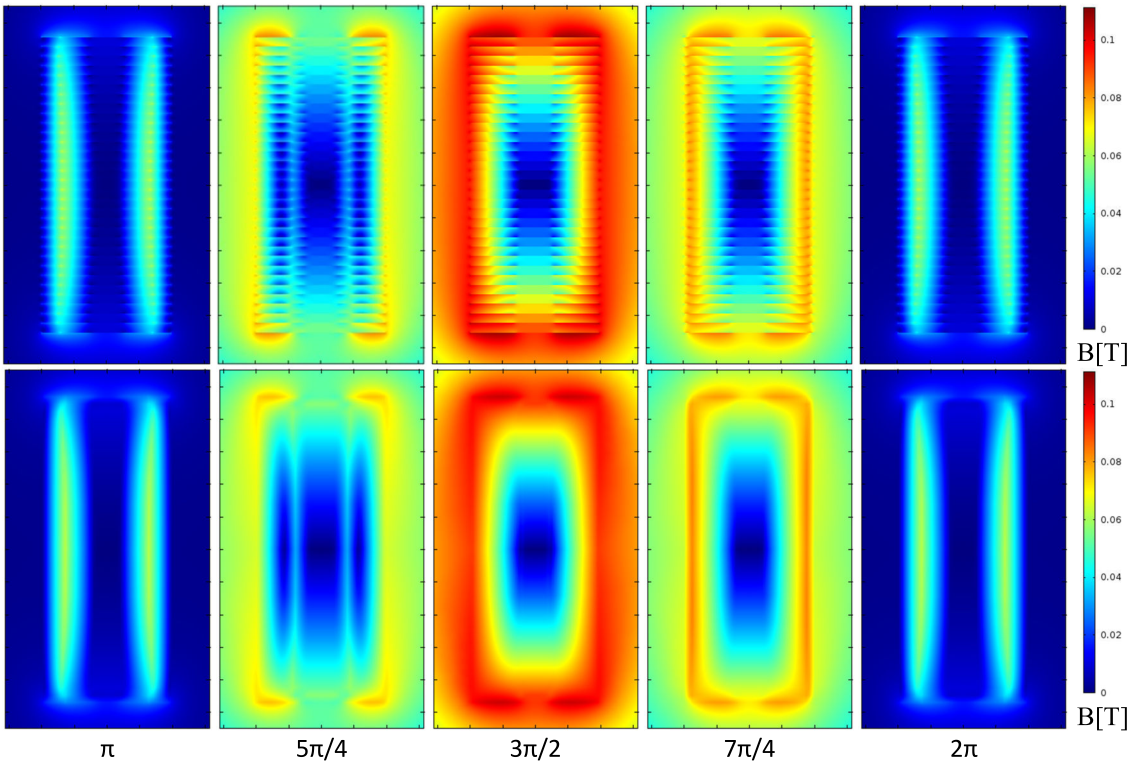

Figure 19. Magnetic flux density magnitude B [T] for half AC cycle in a stack of 32 tapes in the transport current case. Each tape carries a sinusoidal net current of 60 A at 50 Hz. *Top:* Actual tapes. For visualization purposes, geometric features such as domain edges were not plotted. *Bottom:* Anisotropic bulk model. Results shown at different phase values: from π to 2π (from left to right) in π/4 increments. The actual width of the superconducting layers is 4 mm while the height of the stack is 9.376 mm. The separation between ticks in the plot frames is 1 mm.

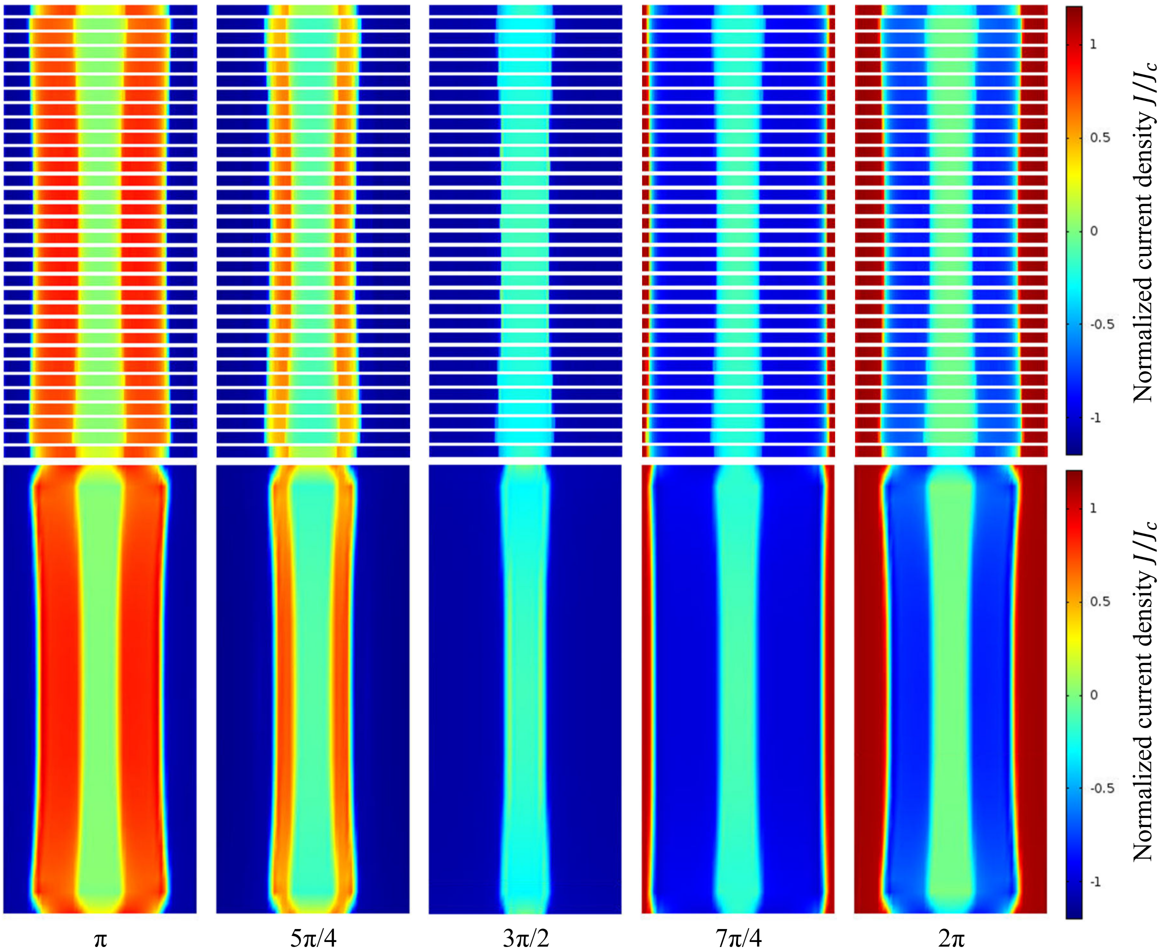

Figure 20. Normalized current density J/J_c for half an AC cycle in a stack of 32 tapes in the transport current case. Each tape carries a sinusoidal net current of 60 A at 50 Hz. *Top:* Actual stack of tapes. For visualization purposes, only data for the superconducting layers' is plotted and the superconducting layers' actual thickness is artificially expanded in the vertical direction. *Bottom:* Anisotropic bulk model. Results shown at different phase values: from π to 2π in π/4 increments (from left to right). The actual width of the superconducting layers is 4 mm while the height of the stack is 9.376 mm.

Agreement was also found in calculating the instantaneous losses $\xi = \int_S \boldsymbol{E} \cdot \boldsymbol{J} dS$ for an AC cycle as shown in Figure 21. The first lower "hump" was due to the transient caused by the zero initial conditions for the simulation. Only small discrepancies were presented. Those can easily be attributed to the fact that the normal conducting layers of the tapes were ignored in the bulk model. Overall, exact reproduction of the calculations is not likely to happen as information is lost in the homogenization process. However, the results are considered to be good enough to pursue further studies.

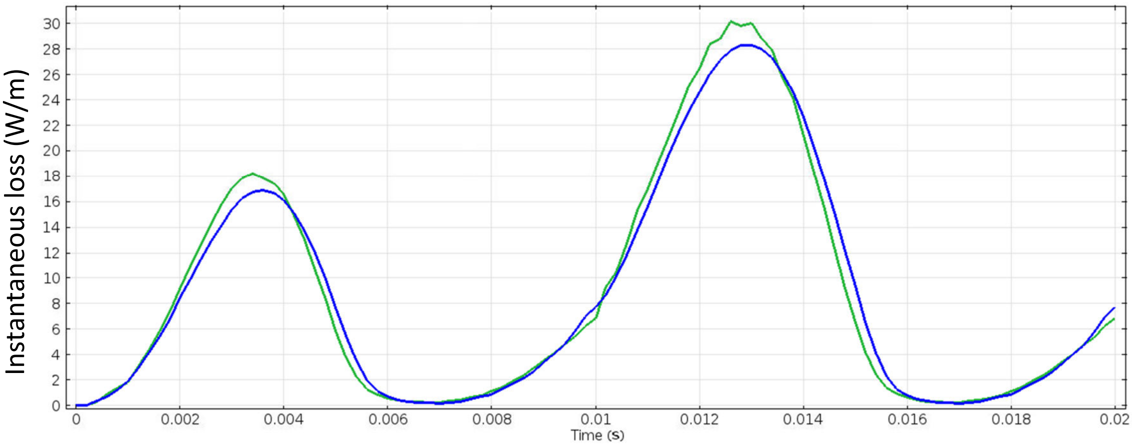

Figure 21. Instantaneous loss ξ [W/m] for the actual stack of 32 tapes (blue line) and its antistrophic bulk model (green line) in the transport current case.

Values for the average AC loss (in W/m) are shown in Table 2. Overall, the agreement of the homogenized model with the original stack is good. Furthermore, the error decreased for the bigger stacks. This could be explained by noticing that with the increasing number of tapes in a stack, the border effects caused by the top and bottom conductors have a lesser impact for the whole stack and the periodic structure dominates. However, since this simple test with three coils does not provide enough data to support a strong conclusion in this matter, further investigations should be latter performed so that other factors such as mesh density are taken into account.

Transport current			
	AC loss @ 50 Hz (W/m)		
# of tapes	Original stack	Homogenized stack	Error (%)
16	6.74	6.86	1.72
32	11.33	11.40	0.61
64	15.44	15.47	0.20

Table 2. Comparison of the calculated AC losses in the transport current case for both original and homogenized stacks.

Computing times for both modeling strategies are shown in Table 3. Overall, the performance is better for the homogenized model than for the original stack. Furthermore, the speedup increases with the number of conductors considered. Almost two orders of magnitude speedup was achieved for the 64 tapes stack. This is clearly explained by the fact that while more mesh elements – and consequently, degrees of freedom – where needed to simulate the original stack, no mesh increase was needed in the homogenized model. However, simulating even larger stacks with the bulk model will likely require more mesh elements to achieve accurate results. Nonetheless, this mesh increase should be expected to have a weak impact in the overall computing time when compared to full scale simulations.

Transport current			
	Computation time (s)		
# of tapes	Original stack	Homogenized stack	Speedup factor
16	3251	639	5.09
32	8583	472	18.18
64	31206	426	73.25

Table 3. Comparison of the computing times for simulating one AC cycle in the transport current case for both original and homogenized stacks.

4.7 Applied magnetic field

Figure 22 shows the magnetic flux density for half AC cycle for both an original stack of 32 tapes and its anisotropic bulk model representation for the applied magnetic field case. The normalized critical current density J/J_c is presented in Figure 22. Again, as in the transport current, the profiles for both the magnitude of the magnetic flux density $\boldsymbol{B}$ and the normalized critical current J/J_c in the original stack are well reproduced by the anisotropic bulk model.

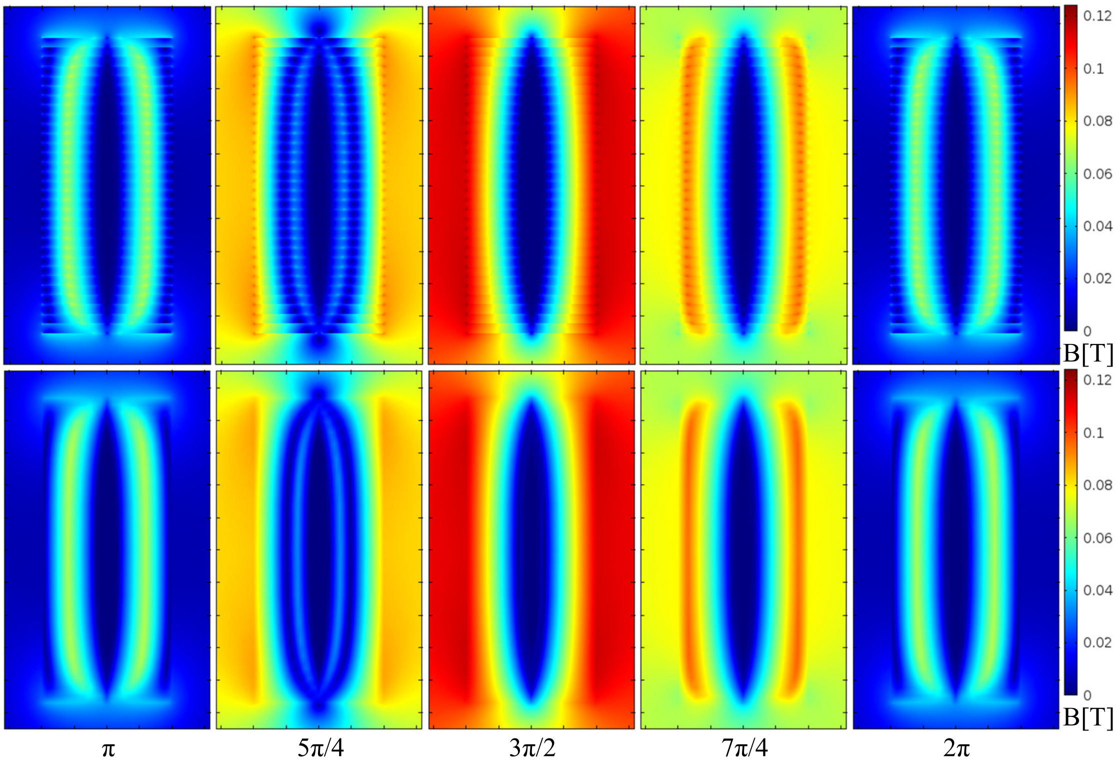

Figure 22. Magnetic flux density magnitude B [T] in a stack of 32 tapes for the magnetization case. A sinusoidal magnetic flux density of 100 mT at 50 Hz was applied vertically to the stack. *Top:* Actual tapes. For visualization purposes, geometrical features such as domain edges were not plotted. *Bottom:* Anisotropic bulk model. Results shown at different phase values: from π to 2π (from left to right) in π/4 increments. The separation between ticks in the plot frames is 1 mm. The actual width of the superconducting layers is 4 mm while the height of the stack is 9.376 mm.

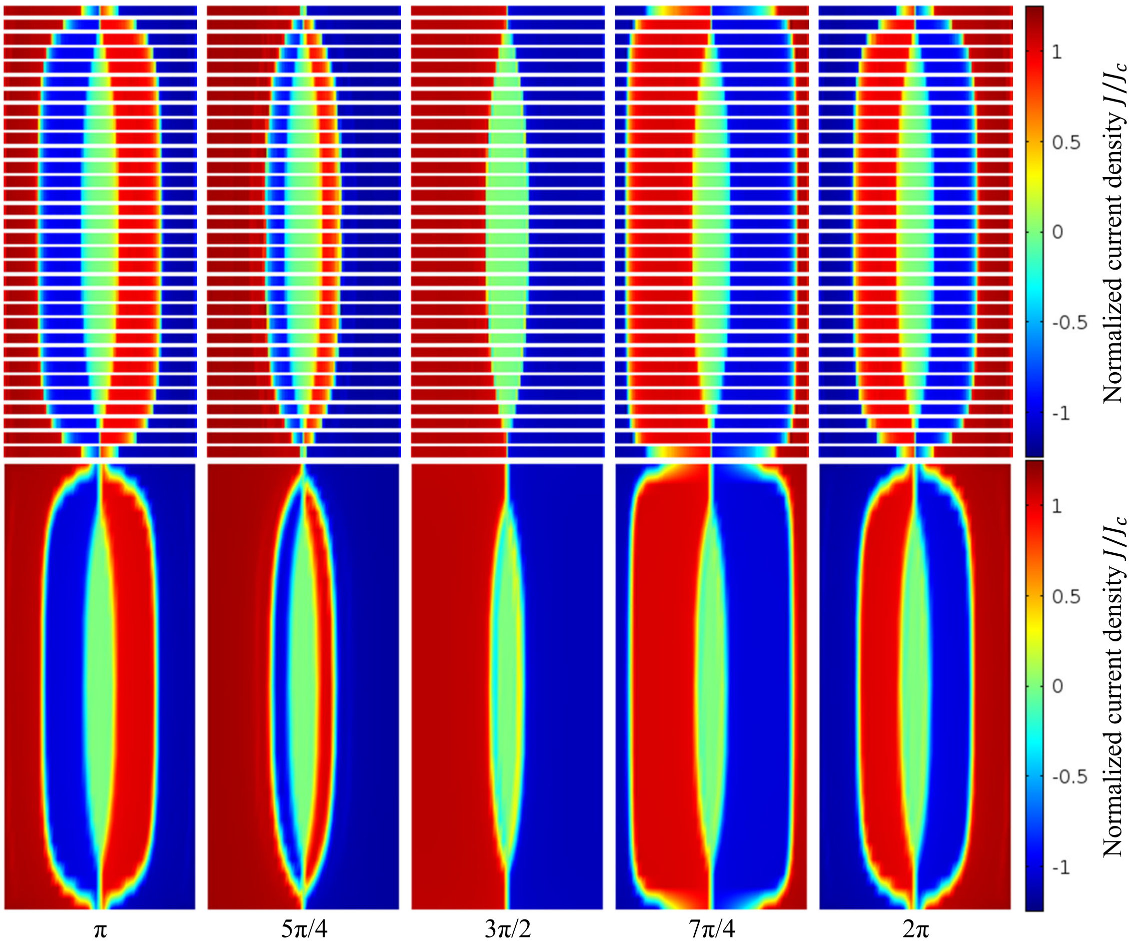

Figure 23. Normalized current density J/J_c for half an AC cycle in a stack of 32 tapes in the magnetization case. A sinusoidal magnetic flux density of 100 mT at 50 Hz was applied vertically to the stack. *Top:* Actual stack of tapes. For visualization purposes, only data for the superconducting layers' is plotted. The superconducting layers' true thickness is artificially expanded in the vertical direction. *Bottom:* Anisotropic bulk model. Results shown at different phase values: from π to 2π in π/4 increments (from left to right). The actual width of the superconducting layers is 4 mm while the height of the stack is 9.376 mm.

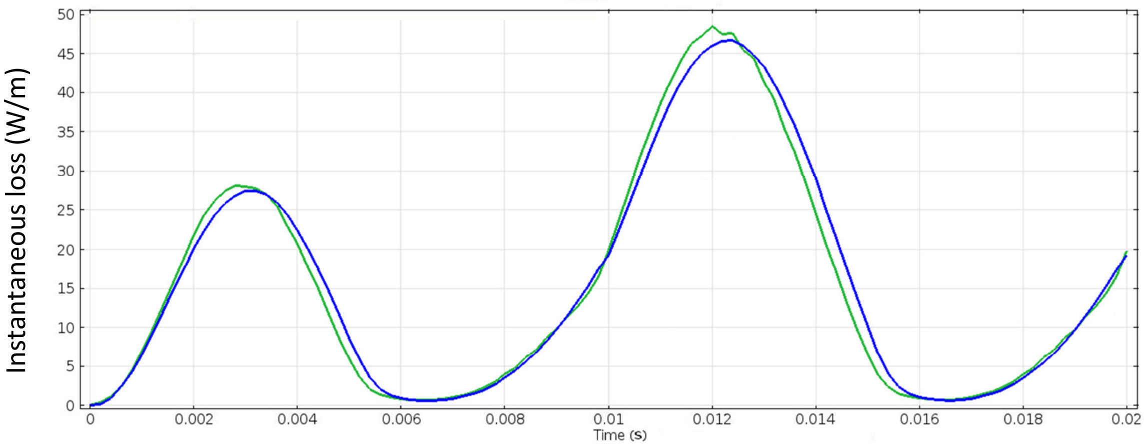

Figure 24. Instantaneous loss ξ [W/m] for the actual stack of 32 tapes (blue line) and its antistrophic bulk model (green line) in the magnetization case.

Again, as in the transport current case, good agreement was found between both calculations for the instantaneous losses $\xi = \int_S \boldsymbol{E} \cdot \boldsymbol{J} dS$ for an AC cycle as shown in

Figure 24. Once more, only small discrepancies were seen and results are considered to be good enough to pursue further studies.

Values for the average AC loss (in W/m) for the magnetization study are shown in Table 4. Just like for the transport current case, the agreement of the homogenized model with the original stack is good with a decreasing error for bigger stacks.

Applied magnetic field			
	AC loss @ 50 Hz (W/m)		
# of tapes	Original stack	Homogenized stack	Error (%)
16	10.30	10.05	2.45
32	19.86	19.49	1.88
64	41.28	40.61	1.61

Table 4. Comparison of the calculated AC losses in the magnetization case for both original and homogenized stacks.

Computing times for the magnetization case in both modeling strategies are shown in Table 5. Again, the performance is better for the homogenized model than for the original stack. Speedup above two orders of magnitude was achieved for the 64 tapes stack.

Applied magnetic field			
	Computation time (s)		
# of tapes	Original stack	Homogenized stack	Speedup factor
16	3702	539	6.87
32	12207	647	18.87
64	76734	676	113.51

Table 5. Comparison of the computing times for simulating one AC cycle in the magnetization case for both original and homogenized stacks.

4.8 Conclusions

The anisotropic bulk model for a stack of tapes was extended by the use of a continuous $\boldsymbol{E}-\boldsymbol{J}$ relationship, so that local overcritical current densities could be considered. Furthermore, the model presented did not make any assumptions upon the shape of the boundaries between the critical and subcritical regions.

The proposed strategy showed good agreement when compared to full 2D simulations performed with the method described in the previous chapter. Both current transport and magnetization cases in stacks of 16, 32 and 64 tapes were considered.
In particular, calculation of AC losses was performed yielding errors under 2.5%.

In general, the anisotropic bulk model outperformed the full 2D simulations in terms of computational speed. Particularly, a speedup factor of about two orders of magnitude was achieved for the larger coil. Although, other mesh types were tested for the anisotropic bulk model, good results were obtained with a rough structured mesh with as little as 19X50=950 elements for the whole bulk. No explicit investigation was carried out to find an optimal mesh distribution, as the speedup was deemed to be significant enough to pursued further modeling and simulation goals.

Chapter 5 Simulation of a HTS generator

As already discussed in chapter 1, during normal operation, superconducting generators are exposed to ripple fields that could be produced from a wide variety of sources: the teeth in the stator, load change, rotational speed fluctuations, etc. Unlike in the DC conditions case, superconductors experience high losses when exposed to AC fields. Thus, calculation of such losses is relevant for machine design, cryostat optimization and for increasing the overall performance. In this chapter, transient simulation of a synchronous generator with superconducting rotor windings is presented. The model is driven by both rotational speed and electric load signals. A two-stage segregated model approach is used to separate the electromagnetic fields calculation in the generator from the superconducting coils. Calculation of AC losses is accomplished by using the homogenization technique described in the previous chapter. For the sake of simplicity and to deepen the analysis, only the events of startup and load change are studied. Results are analyzed and issues such as coil design, critical current ratting, electric load change rate limits, cryocooler design, identification of *quench-prone* regions and overall transient performance are addressed.

5.1 Background

The work reported in this chapter follows from previously presented results at the *Joint Centennial Conference on Applied Superconductivity* held in 2011 at The Hague, The Netherlands. The submitted manuscript has already been accepted for publication in a special issue of Physics Procedia by July 2012. A copy of said manuscript is included as Appendix D. In that previous work, the critical current density of the superconducting materials was assumed to be constant. However, in this chapter, no such simplification was made since a $\boldsymbol{B}$ field-dependence for the critical current is considered just as described in Chapter 4.

5.2 Simulation Strategy

The simulation goal was set on computing the AC losses in an electric generator with rotor windings made of 2G HTS coated conductors during transient behavior. In that way, heating losses are to be computed as a response to the electric load and rotational speed signals. To cope with the size of the modeling problem at hand and for simplicity, a two-stage segregated model was pursued. In that way, the generator electromagnetic computation could be decoupled from the superconducting coils.

Considering tightly packed coils, if each conductor in the rotor windings carries a net given current $I(t)$, the magnetic field $\boldsymbol{H}$ in the coupling boundary, as shown in Figure 25, has a weak dependence upon the actual current density distribution inside each conductor. Hence, the magnetic field $\boldsymbol{H}$ at the coupling boundary is mainly due to the global effect of the current in the coils, rather than the actual current distribution inside each conductor. This allows simulating the electromagnetic response of the generator without taking into account the geometrical internal features of the rotor's coils, or the $\boldsymbol{E}-\boldsymbol{J}$ characteristic relationship of its constituent materials. In fact, that is the standard method used to simulate conventional rotating machinery, where a uniform current density is typically assumed in the rotor windings. Although some studies such as coil optimization in HTS based machines can be performed following this principle [74], calculation of AC losses in the superconducting materials requires knowledge of the local current density.

Following from the assumption described above, the actual current density distribution in the conductors of the rotor's coils can be recalculated from the generator simulation data. Using the previously computed magnetic field $\boldsymbol{H}$ in the coupling boundary as a Dirichlet condition, a second simulation can be performed to calculate the AC losses. Consistent with the original assumption, no feedback is considered from the second to the first model. In what follows and for convenience, the first model will be referred as the "generator model" and the second as "the coils model". Hence, the overall strategy as depicted in Figure 25 can be summarized as follows:

1) Both rotational speed and electric load are used as input signals for the generator model where the current distribution in the rotor windings is assumed uniform.
2) The coils model uses the previously computed magnetic field $\boldsymbol{H}$ on a coupling boundary to calculate the actual current density distribution and the AC losses in the superconducting windings of the rotor's coils.

For simplicity, in what follows, the coils will be referred to by their number as shown in Figure 25.

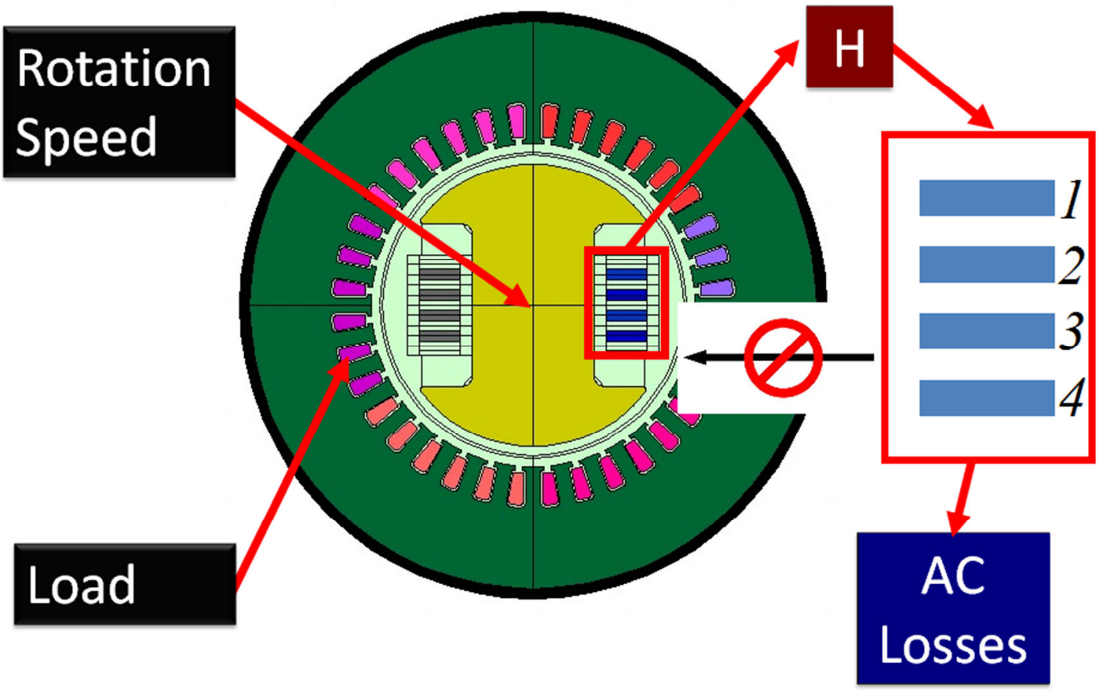

Figure 25. Simulation strategy. In the generator model (*center*), both electric load and rotation speed are considered as known inputs. Using this model, and assuming a uniform current distribution in the coils, the magnetic field $\boldsymbol{H}$ is calculated on a coupling boundary (*red rectangle*) around the rotor's windings. The coils model (*right*) uses this as a Dirichlet boundary condition to compute the actual current distribution in the rotor's coils and calculate the AC losses. No feedback is considered from the coils model to the generator model. The stator's outer and inner diameters are 28 cm and 16 cm respectively. The rotor's diameter is 14 cm. The axial length of the machine is 15 cm [8].

Generator model

The generator model (Figure 25) was developed by Nenad Mijatovic, a fellow colleague at the department of Electrical Engineering of the Technical University of Denmark. It follows design parameters as reported in [7] and [8]. This provided with a test bench for running transient problems. The model is driven solely by the rotor speed and electric resistive load signals. For uniformity, every superconducting coil was assumed to be comprised of 50 turns of the 2G HTS coated conductor manufactured by Superpower [18] each carrying 50 A. In the generator model, this corresponded to a bulk conductor with a uniform current density such that a net 2500 A were carried in each of the four coils. The model uses the AC/DC module of COMSOL Multiphysics for rotating machinery. This module solves the magnetic vector potential formulation of Maxwell's equations [75]. The magnetic field $\boldsymbol{H}$ is then calculated with $H = (\nabla \times A)/\mu$. At the coupling boundary, data is stored for further analysis in the coils model.

Coils model

The superconducting coils were modeled using the homogenization technique with a power law $\boldsymbol{E}-\boldsymbol{J}$ relationship as described in the previous chapter. Hence, all geometric features in the coils were "washed out" and four anisotropic bulks were used to model the generator windings. All parameters, including the superconducting material properties, were as described in chapter 4. This corresponded to coils made of 4 mm wide 2G HTS coated conductor with a DC critical current in zero external field of 99.227 A. Integral constrains as previously described in equation (56) were implemented in each bulk. In this way, an equivalent sinusoidal net current per conductor of 50 A was imposed. To couple with the generator model, Dirichlet boundary conditions were used at the coupling boundary.

5.3 Case study: Load change

To test the proposed modeling strategy, a simple load change was implemented as shown in Figure 26. All events were simulated using smooth functions so that sharp transients could be avoided. Therefore, load changes were not instantaneous as small smoothing periods were allowed. For clarity in the narrative, reference to events will not include this smoothing period into account.

At $t = 0.0s$ the generator was stationary with its rotor coils already cooled down to 77 K. The coils were not energized and no electric load was connected to the terminals of the stator windings. From $t = 0.0s$ to $t = 1.0s$, the current in the rotor's coils was increased linearly until the desired value of 50 A was reached. The rationale behind this selection for the current value will be explained in the discussion section. In what followed, that current was kept constant. From $t = 1.0s$ to $t = 7.0s$, the machine was kept static, with no electric load applied. This period was intended to let the system relax and allow for the transient behavior of the ramp up process to settle and fade. At $t = 7.0s$ the generator's shaft started rotating in counterclockwise direction at 1.91 Hz. At $t = 8.0s$, a resistive electric load of $1\,\Omega$ was connected to every phase of the generator (taking into account $0.32\,\Omega$ for the self-resistance of the copper windings). At $t = 10.0s$, the resistive load was changed to $0.5\,\Omega$. Finally, at $t = 12.0s$, the load was reverted to its previous value of $1\,\Omega$.

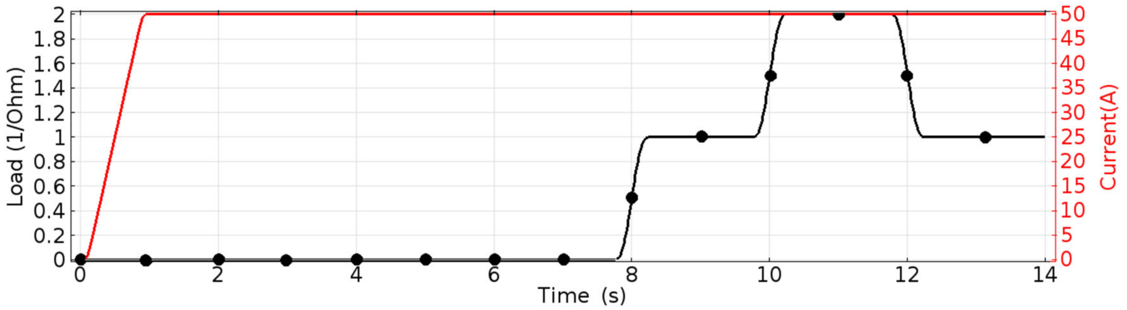

Figure 26. Ramp-up current in each of the superconducting rotor coils (*red* —). The electric load signal in the stator windings (*black* ●) is presented as an equivalent conductance.

5.4 Results

Simulation of the whole transient of 14 seconds was carried out as described in the previous sections. The coils model required 2.5 hours to run. This showed to be a not so big computational surcharge, given that simulation of the generator model alone took more than 8 hours to complete. In reporting the transient response, a selection of images describing it is presented from Figure 27 to Figure 32. The images are presented in a sequential array, so that the transient can be followed in a comic strip-like fashion. Figure 27 shows the magnetic flux density magnitude B as calculated by the generator model. Notice the symmetry at $t = 7.9\ s$. However, starting at $t = 8.0\ s$, a gradual shift – or lag – is seen. As expected, this event corresponds to the moment when the electric resistive load is connected to the generator.

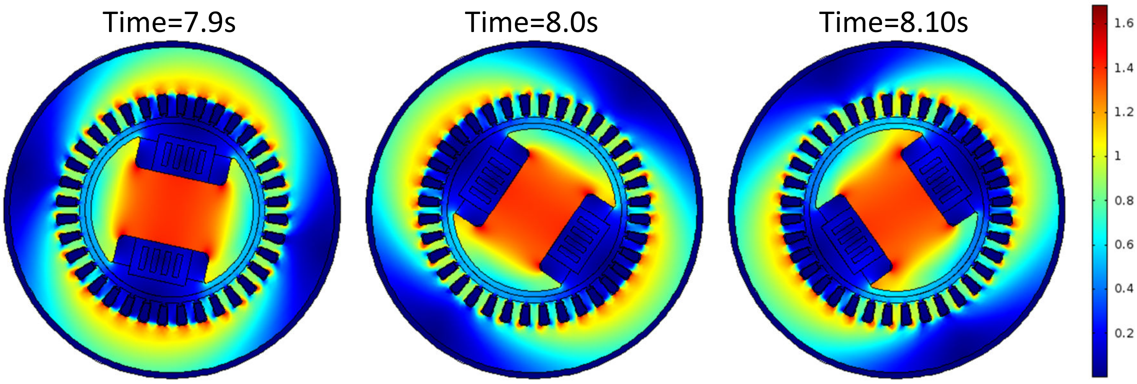

Figure 27. Magnetic flux density magnitude B [T] as calculated by the generator model. The rotor moves in counterclockwise direction at 1.91 Hz**.**

Figure 28 shows the magnetic flux density magnitude B as calculated by the generator model in half of the rotor's windings. The ramp up transient and subsequent relaxation period is not displayed. At $t = 7.0\ s$, the field is symmetric and two regions with low magnetic flux density are observed in coils 2 and 3. At $t = 8.0\ s$, magnetic flux penetrates from the upper right corner of the coils. The two low field regions in coils 2 and 3 are shifted down. The pattern remains relatively unchanged until when at $t = 10.0\ s$, a higher intensity field enters from the upper right corner pushing the low field regions even lower. At $t = 12.0\ s$, the magnetic flux density returns to its previous state. In the same way, the magnetic flux density magnitude B as calculated by the coils model is presented in Figure 29. Notice the overall agreement with Figure 28. To ease the comparison, both scales are set to display the same range of values. The most noticeable difference is that in the coils model a low field region in the lower left part of coil 1 remains throughout the simulation.

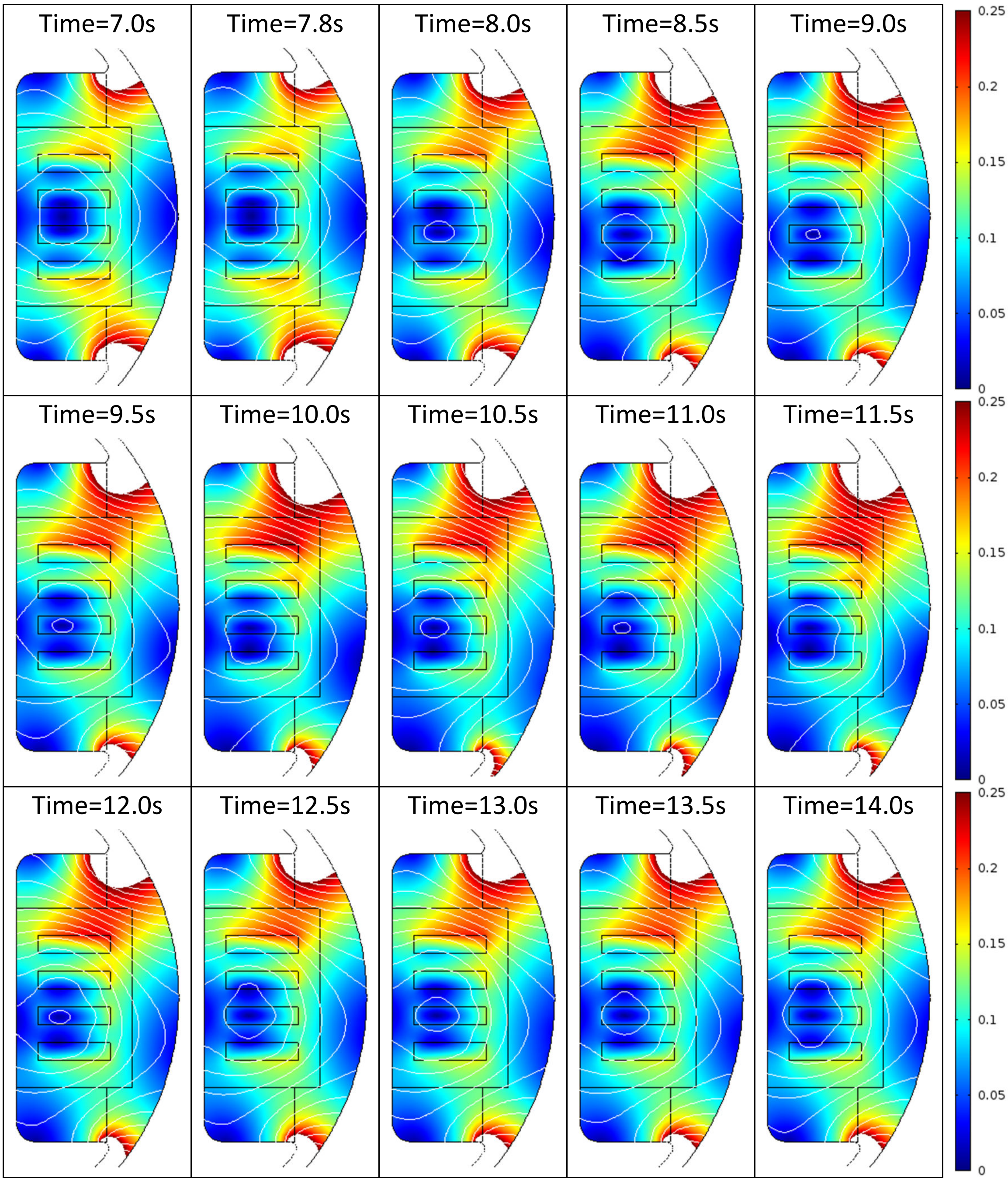

Figure 28. Magnetic flux density magnitude *B* [T] as calculated by the generator model. For easier comparison with Figure 29, data values above 0.25 were not plotted. Streamlines follow the magnetic field lines.

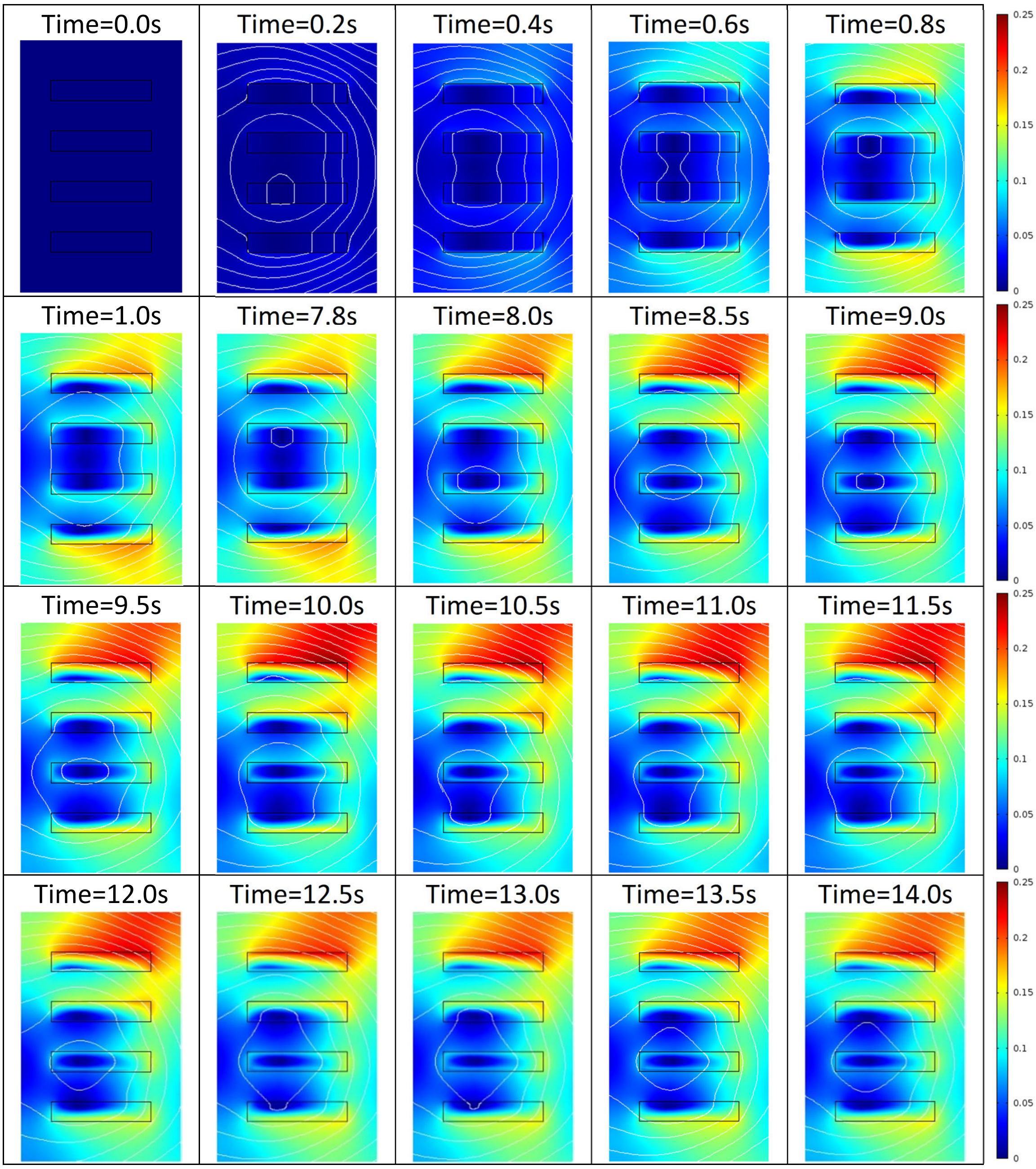

Figure 29. Magnetic flux density magnitude B [T] as calculated by the coils model. Since no significant variation was observed from $t = 1\ s$ to $t = 7.8\ s$, no images of that period are presented. Streamlines follow the magnetic field lines.

Figure 30 shows the normalized current density J/J_c in the superconducting coils. While the ramp up of the coils takes place, transport currents appear in all coils. However, magnetization currents also appear in coils 1 and 4. For this reason, coils 2 and 3 show bigger subcritical regions (yellow) than coils 1 and 4. At $t = 7.8\ s$, after the transitory has passed, a small reduction in the amplitude of the normalized current density in the transport region is observed. This is compensated with the corresponding reduction of the subcritical regions. At $t = 8\ s$, when the electric load is connected, overcritical current densities (dark red) are observed in the upper right corners of coils 1 and 2, and to a smaller extent in coils 3 and 4. After this moment, small magnetization currents begin to appear in all coils and all subcritical regions are shrunk, in fact by $t = 8.5\ s$, coil 1 no longer has such a region. At $t = 10\ s$, when the electric load is increased, the overcritical zones grow covering the upper part of coil 1 and the upper right corners of the other coils. Overcritical current densities relax and subcritical regions withdraw even further during the small relaxation period before the new load change. At $t = 12\,s$, when the electric load is reduced to its previous value, small overcritical regions appear in the lower right corner of the coils. These regions faded after a small relaxation transient. In the last image, at $t = 14\,s$, all coils present magnetization currents. No further studies were performed upon the relaxation time for the after transient load change.

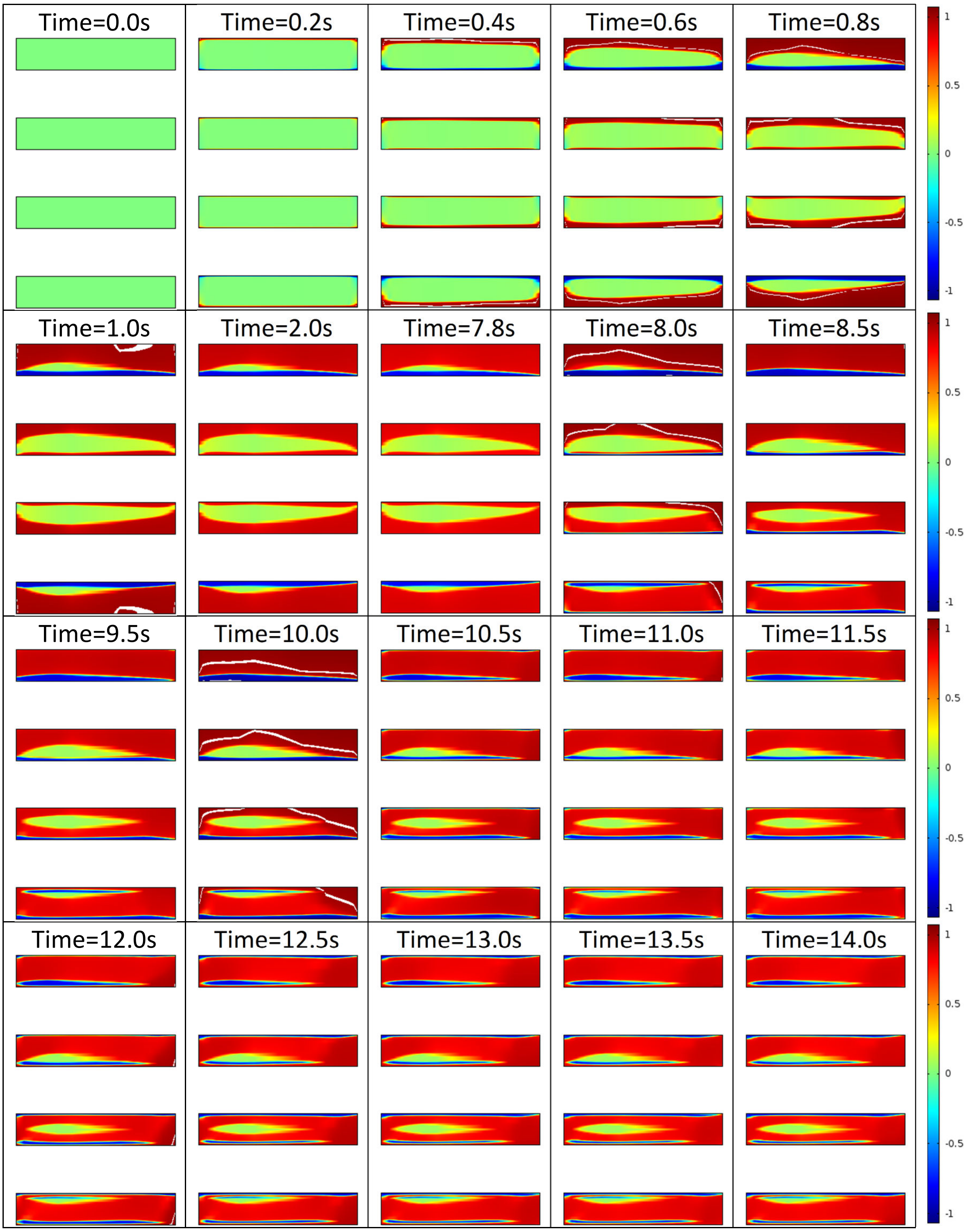

Figure 30. Normalized current density J/J_c in the superconducting coils. As an aid to the eye to identify the supercritical regions, a white contour line is drawn at $J/J_c = 1$.

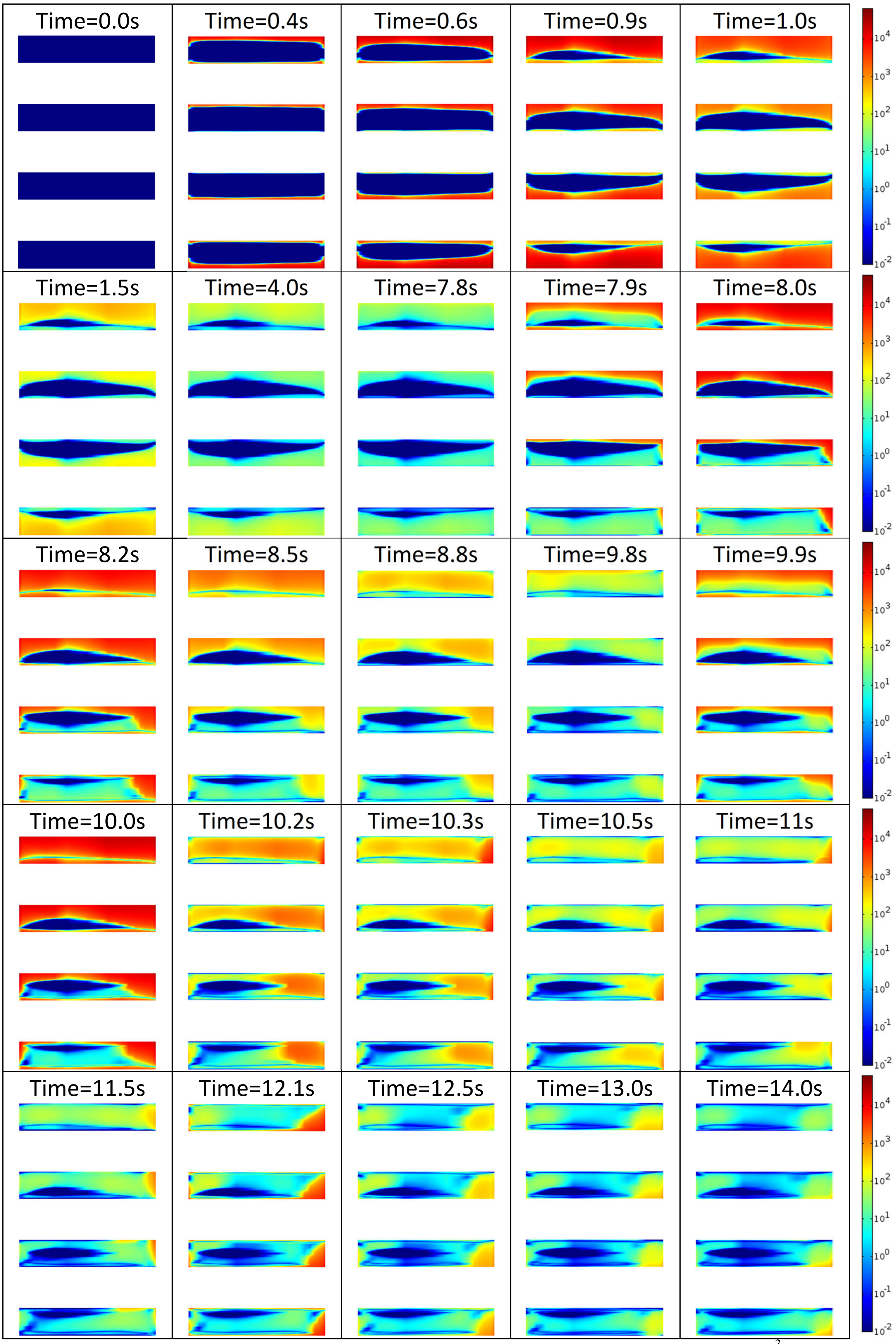

Figure 31. Instantaneous power loss density ($\boldsymbol{E} \cdot \boldsymbol{J}$) in the rotor's windings (in W/m^3). For easier visualization, a logaritmic scale is used. Data displayed was capped under the 10^{-2} value. Hence, all values from 0 to $10^{(-2)}$ were plotted with the darkest shade of blue.

Calculation of the instantaneous power loss density ($\boldsymbol{E} \cdot \boldsymbol{J}$) in the rotor's windings is presented in Figure 31. In what follows, regarding their power loss density value, red and blue regions will be referred to as hot or cold respectively. During the ramp-up of the coils, the losses profile follows closely the current distribution pattern as already shown in Figure 30. The hot regions cool down rapidly, by $t = 7.8\,s$ a reduction of almost three orders of magnitude is seen for the power loss density. This confirms the fading out of the transient. At $t = 8.0\ s$, hot regions appear in the upper part of coils 1,2 and 3 and the upper right corner of coil 4. Again, this transient loss decrease and by $t = 9.8\ s$, most hot regions are already cooling down. The load change at $t = 10\ s$ heats up most of coil 1, the upper region of coils 2 and 3 and the upper right corner of coil 4. Once more, the transient loss fades rapidly. The load change at $t = 12\ s$, produces small hot regions at the lower right corners of each coil. Towards the end of the simulation, all coils continue their cooling down trend.

A broader perspective can be provided by considering the instantaneous loss $\xi = \int \boldsymbol{E} \cdot \boldsymbol{J} dS$ in all coils and multiplying it by the length of the machine (15 cm). This corresponds to the total instantaneous loss in the straight section of the superconducting race track windings. Figure 32 presents such result. The highest loss was found during the ramp up of the coils at t =0.85 s, reaching a peak value of 0.69 W. Peaks of 0.43 W ($t = 8.1\ s$) and 0.5 W ($t = 10.1\ s$) were also observed during the increasing load changes. A smaller peak of 0.016 W ($t = 12.16\,s$) was also observed during the decreasing load change. Qualitatively, all this is consistent in both schedule and amplitude with the planned transient and the results previously shown in Figure 31. However, an unexpected local maxima of 0.026 W was also found at $t = 8.6\ s$.

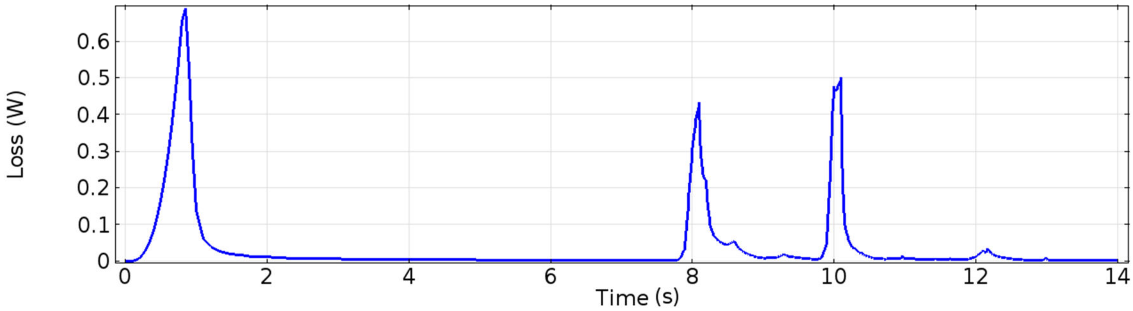

Figure 32. Total instantaneous loss in the superconducting coils of the generator.

5.5 Discussion

Values for the magnetic flux density computed with the coils model (Figure 29) were in good agreement with the previous calculations made by the generator model (Figure 28). This reassured confidence in the original two-stage segregated model assumption for the simulation strategy. During normal operation, but specially at increasing load changes, the upper part of coil 1 experienced the highest magnetic fields. Design tools such as coil optimization or the use of multiple excitation currents [74] could be used to allow the other coils to take a better share of this burden.

One important issue that can be clearly observed in Figure 30, is that coil design should consider the actual layout of the generator. The current density profile of an isolated coil as shown in Figure 13 and Figure 20 has little to do with the actual profile it will display once it is located inside a generator. Hence, information of the DC critical current of an isolated coil is of little relevance without considering the electromagnetic environment it will finally face. Further improvements on coil design could be achieved by considering the normal operation requirements and the transitory load changes.

Several other values for the transport current in the superconducting coils were tested, however, the choice of 50 A was justified since during both ramp-up and increasing load change, large regions of the coils reached overcritical current density values as seen in Figure 30. It could be argued that the overcritical zones can be avoided or reduced with longer and smoother transition periods. This idea is supported by noticing that after a small transitory, the current density in the coils returns to subcritical values, even at the highest load test. However, that is where the actual value of this simulation tool pays off. In that sense, simulations can be performed to find the maximum load change rates allowed for a given current rating without running into overcritical currents.

Furthermore, this simulation tool can be used in cryocooler design. Notice that during the ramp-up period, the hot zones show a symmetric pattern. The top of coils 1 and 2 and the bottom of coils 3 and 4 present the hottest regions. However, the hot areas in coils 3 and 4 vary for changing electric loads. This is especially noticeable in the upper right corner. Hence, cryocooler design should take this issue into account. For instance, heat sinks located on top of all coils and covering their right side could secure a better heat removal during transient response, than if placed only at the bottom of the coils. In the same manner, the hot regions are at risk of becoming normal if excess heat is not removed fast enough. This phenomenon is known as quenching [76]. Once a region becomes normal, ohmic losses appear with a corresponding further increase in temperature. This process can damage the superconducting materials; hence quench protection is essential for safe operation [26]. The simulation tool presented here could allow for *quench-prone* regions to be easily identified. Thus, sensors can be better located, and monitoring and quench protection optimized.

The last plot presented, Figure 32, can be used for comparison with experimental data. It provides with a compact lumped description of the overall hysteresis losses in a given machine design during transient operation.

5.6 Conclusions

A two-stage segregated model strategy to calculate the hysteresis losses in a superconducting generator during transient operation was developed. The strategy relied upon a one-way coupling form the generator model to the coils model. The latter used a homogenization technique to model the coils in the rotor windings. This allowed for computation of the coils model to run in about 2.5 hours. This was deemed to be a very reasonable time considering that the generator model required more than 8 hours to run. The proposed model was used to simulate ramp-up and electric load change events. Analysis of results allowed considering important factors such as critical current ratting of a coil designed for operation in an electric generator. The issues of electric load change rate limit, cryocooler design and identification of *quench-prone* regions was also addressed. Finally, calculation of the overall hysteresis losses during transient response of the machine was presented. Further studies must be carried out to compare and match the simulation results with experimental data and calibrate the simulator to make tailored predictions for specific transient operation cases. As an additional remark, it is also important to notice that this strategy can easily be implemented to analyze and study other large scale superconducting machines and devices like motors, transformers, ROEBEL cables and magnet coils.

Chapter 6 Summary of Publications

Some of the results obtained during the course of this PhD study have already been published or submitted for publication. Below, a brief description of them is presented. The first four articles dealt with calculation of AC losses in large scale devices. Each new article provided an improved model that included either a new material property or a computational speed up technique. All four were in the path towards the simulation of an electric generator with superconducting rotor windings. The fifth article considered a feasibility study for a 5 MW superconducting wind turbine generator. The final article presented dealt with optimization of the coils inside a superconducting generator. Although the author of this thesis has coauthored other publications [8] [77] [78], they are not included here, as his involvement in those works was to a lower degree and they do fall out of the intended scope of these this PhD thesis.

Appendix A:

Article 1 presented the first findings upon computational speed increase in simulating superconducting thin-film superconductors carried out during this PhD study. The method relied on implementing a multiscale meshing technique based on mapped meshes that resembled the aspect ratio of the conductors involved. The proposed technique performed two to three orders of magnitude faster than previously reported results without compromising accuracy.

Appendix B:

In Article 2, the multiscale meshing method developed in article 1 was used to simulate a racetrack coil composed of 57 turns of 2G HTS coated conductor. The model depicted the actual layout (up to the μm scale) of the layered media conductors. However, the nonlinear permeability of the substrate was not considered. Calculation of transport AC losses was performed at different peak current values. Both cases of constant and magnetic field dependent critical current density were considered. Simulation of a whole AC cycle was performed in well under 6 hours.

Appendix C:

A further improvement to the previous works was presented in article 3. Here two parallel coils composed of 50 turns each was simulated. In this work, both non-magnetic and nonlinear magnetic substrates were considered. Simulation results showed that for coils of tapes with magnetic substrate, a significantly higher loss was found in the central windings when compared to coils of tapes with non-magnetic substrate. Calculation of AC losses was carried out. It was concluded that the superconducting coil would experience higher losses that its equivalent copper counterparts at 50 Hz. Cooling requirements, AC losses and electrical machines are further discussed. It is concluded that investigations on mitigation of AC losses must be carried out in the case of machines with both rotor and stator superconducting windings.

Appendix D:

Article 4 presented modeling and simulation of a synchronous generator with superconducting rotor windings. Calculations relied upon a two-stage segregated model. In a first model, the electromagnetic response of the generator was computed. A second model used this information to calculate the hysteresis losses in the superconducting windings. To speed up calculations, the second model was based on a homogenization technique as described in chapter 4 of this work but considered a constant critical current density for the HTS material. The transient response of a generator under ramp-up of the rotor coils and a subsequent electric load change was performed. Finally, the corresponding heating losses were calculated.

Appendix E:

In article 5, a feasibility study for the installation of a 5 MW superconducting wind turbine generator was carried out. Weight restrictions and price target estimates for both 2G HTS coated conductors and turbine installation by the year 2020 were considered. The study showed that such a superconducting generator is feasible as long as it uses coated conductors with a high engineering critical current density, such as the ones manufactured by Superpower. The study concluded by providing a 24 pole generator design with a 4.2 m outer diameter, active length of 1.2 m and weight of 32 tons.

Appendix F:

Article 6 carried out a study intended to obtain optimal coil designs for the rotor of a 3 T HTS machine. The aim was set to minimize coil prices while keeping the rated air-gap magnetic flux density. Several commercially available HTS coated conductors were considered. Optimal coil designs are obtained and further studies are proposed such as the introduction of multiple excitation power supplies or the use of coils with several types of HTS tapes.

Chapter 7 Concluding Remarks

As a whole, this thesis work presents a bottom-up approach towards the simulation of a generator with superconducting rotor windings. For that purpose, tools for speed-up calculation of hysteresis losses in stacks of 2G HTS coated conductors were developed. A first strategy, based on the use of a multiscale mesh, achieved a reduction of computational time by two to three orders of magnitude in a single tape without compromising accuracy. The technique was based upon using mesh elements with large aspect ratios resembling the layered media in the conductors. This method alone, allowed for calculating AC losses of racetrack coils intended for use in actual generators within manageable computing times. Further improvements were achieved by extending the anisotropic bulk method to include a power law $\boldsymbol{E}-\boldsymbol{J}$ relationship. This allowed for overcritical current densities to be considered. The method did not rely on any a priori assumptions for the topology or shape of the critical and subcritical regions. Using the developed anisotropic bulk model, calculation of AC losses in superconducting stacks was achieved in a just a few minutes. Overall, this provided an additional speedup of about two orders of magnitude when compared to the previously developed method. Again, no significant reduction in accuracy was observed.

Simulation of the transient response of a generator with superconducting rotor coils was presented in Chapter 5. For that purpose, a two-stage segregated model strategy was used. A one-way coupling from the generator model to the coils model was implemented. This allowed calculating the transient response of the coils without having to build the whole generator model from scratch. Since the coils model was built based on the anisotropic bulk model previously developed, computation of the transient response was performed very fast. Simulation of a 14 second long transient including ramp-up of rotor coils, load connection and change was performed in about 10.5 hours. Out of those, only 2.5 hours were required by the coils model, a rather modest computational surcharge. Analysis of the simulation results allowed discussing important design and performance issues such as critical current of the superconducting coils, electric load change rate, cryostat design or identification of *quench-prone* regions.

The overall results of this work were consistent with the originally intended goals for a successful model as described in section 1.4. The tools presented here allowed spanning spatially the more than five orders of magnitude required for simulating the superconducting generator proposed. Calculations were performed well within reasonable programing and computation times. All calculations were performed using the commercially available software package COMSOL Multiphysics based in the Finite Element Method. The two-stage model allowed for including normal conductors and magnetic materials with nonlinear properties in the generator model. Finally, design and analysis of a generator with superconducting windings became a rather uncomplicated task.

7.1 Future work

The model proposed in this work has managed to simulate the response of a superconducting generator under transient conditions. However, comparison with experimental data is a very desirable next step.

Although only the cases of ramp-up of rotor coils and electric load change were considered, a large collection of case scenarios can be analyzed, including: short circuit of the stator’s windings, connection to active loads, unbalanced loads, rotational speed change or the effect of including a damper cage, among others. Furthermore, a mechanical model could be added to the generator model so that dynamics include the torque change due to wind speed variations.

A natural next step would be to simulate the 5 MW, 24 pole machine as described in Appendix 5 [6] so that cryogenic design and quench protection can be properly evaluated. In the same manner, the modeling strategy can be used to aid in the design of other superconducting generators.

As described in chapter 4, calculation of AC losses in stacks of 2G HTS coated conductors is of big importance for many applications such as ROEBEL cables, magnet coils, transformers, motors and generators. Further work can be carried out towards analyzing cables and coils with the homogenization method alone. In the same way, transient response of transformers and motors can be calculated with the two-stage segregated model just as in the case of the generator described in chapter 5.

Bibliography

[1] European Commission, Directorate-General for Energy, "Energy Roadmap 2050 - State of Play," 03 05 2011. [Online]. Available: http://ec.europa.eu/energy/strategies/2011/doc/roadmap_2050/20110503_energy_roadmap_2050_state_of_play.pdf. [Accessed 11 11 2011].

[2] European Commission, Directorate-General for Energy, "Energy 2020: A strategy for competitive, sustainable, and secure energy," 2011.

[3] European Wind Energy Association, "EU Energy Policy to 2050- Achieving 80-95% emissions reductions," 2011.

[4] World Wind Energy Association, "World Wind Energy Report 2010," WWEA, Bonn, Germany, 2011.

[5] UpWind, "Design limits and solutions for very large wind turbines," 2011.

[6] A. Abrahamsen, B. Jensen, E. Seiler, N. Mijatovic, V. Rodriguez-Zermeno, N. Andersen and J. Oestergaard, "Feasibility study of 5 MW superconducting wind turbine generator," *Physica C: Superconductivity,* vol. 471, no. 21-22, p. 1464–9, 2011.

[7] N. Mijatovic, A. Abrahamsen, C. Traeholt, E. Seiler, M. Henriksen, V. Rodriguez-Zermeno and N. Pedersen, "Superconducting generators for wind turbines: Design considerations," in *IOP Publishing*, 2010.

[8] N. Mijatovic, B. Jensen, C. Traholt, A. Abrahamsen, V. Rodriguez-Zermeno, N. Petersen, M. Henriksen, E. Seiler, N. Andersen and J. Ostergard, "High temperature superconductor machine prototype," in *IEEE*, Beijing, 2011.

[9] A. Abrahamsen, N. Mijatovic, E. Seiler, T. Zirngibl, C. Traeholt, P. Noergaard, N. Pedersen, N. Andersen and J. Oestergaard, "Superconducting wind turbine generators," *Superconductor Science and Technology,* vol. 23, p. 034019, 2010.

[10] Vestas Wind Systems A/S, "Vestas," 2011. [Online]. Available: http://www.vestas.com/. [Accessed 11 11 2011].

[11] Goldwind USA Inc, "Goldwind," 2011. [Online]. Available: http://www.goldwindamerica.com/ . [Accessed 11 11 2011].

[12] Siemens AG, "Siemens Energy," 2011. [Online]. Available: http://www.energy.siemens.com/. [Accessed 11 11 2011].

[13] General Electric, "General Electric Company," 2011. [Online]. Available: http://www.ge-energy.com/ . [Accessed 11 11 2011].

[14] A. Walters, P. Lusty and A. Hilla, "Rare Earth Elements profile," British Geological Survey's Centre for Sustainable Mineral Development, Keyworth, Nottingham, UK., 2011.

[15] R. Moss, E. Tzimas, H. Kara, P. Willis and J. Kooroshy, "Critical Metals in Strategic Energy Technologies: Assessing Rare Metals as Supply-Chain Bottlenecks in Low-Carbon Energy Technologies," European Commission, Joint Research Centre, Institute for Energy and Transport, 2011.

[16] Lynas Corporation LTD, "2011 Annual Report," 2011.

[17] M. Lesser and J. Muller, "Superconductor technology generating the future of offshore wind power," Colonge, 2009.

[18] SuperPower Inc., "SuperPower," 2011. [Online]. Available: http://www.superpower-inc.com/ . [Accessed 11 11 2011].

[19] C. R. Hammond, "The Elements," in *Handbook of Chemistry and Physics*, 6. e. CRC, Ed., Weast, R.C., Ed. CRC Press, 1988, p. 33.

[20] S. Kalsi, K. Weeber, H. Takesue, C. Lewis, H. Neumueller and R. Blaugher, "Development status of rotating machines employing superconducting field windings," *Proceedings of the IEEE,* vol. 92, no. 10, pp. 1688-1704, 2004.

[21] V. Selvamanickam, *Second-generation HTS Wire for Wind Energy Applications,* Barcelona: Presented at Symposium on Superconducting Devices for Wind Energy Systems. Available online at www.superpower-inc.com, 2011.

[22] B. Gamble, G. Snitchler and T. MacDonald, "Full Power Test of a 36.5 MW HTS Propulsion Motor," *Applied Superconductivity, IEEE Transactions on,* no. 99, pp. 1-1, 2011.

[23] American SuperConductor, "American SuperConductor," 2011. [Online]. Available: http://www.amsc.com. [Accessed 11 11 2011].

[24] AML, "AML Energy," 2009. [Online]. Available: http://www.amlcleanenergy.com/. [Accessed 13 2 2012].

[25] C. Lewis and J. Muller, "A direct drive wind turbine HTS generator," in *Power Engineering Society General Meeting. IEEE* , 2007.

[26] J. Schwartz, T. Effio, X. Liu, Q. Le, A. Mbaruku, H. Schneider-Muntau, T. Shen, H. Song, U. Trociewitz and X. e. a. Wang, "High field superconducting solenoids via high temperature superconductors," *Applied Superconductivity, IEEE Transactions on,* vol. 18, no. 2, pp. 70--81, 2008.

[27] E. Brandt, "Superconductors of finite thickness in a perpendicular magnetic field: Strips and slabs," *Physical review B,* vol. 54, no. 6, p. 4246, 1996.

[28] R. Brambilla, F. Grilli, L. Martini and F. Sirois, "Integral equations for the current density in thin conductors and their solution by the finite-element method," *Superconductor Science and Technology,* vol. 21, p. 105008, 2008.

[29] A. Campbell, "A direct method for obtaining the critical state in two and three dimensions," *Superconductor Science and Technology,* vol. 22, p. 034005, 2009.

[30] N. Amemiya, S. Murasawa, N. Banno and K. Miyamoto, "Numerical modelings of superconducting wires for AC loss calculations," *Physica C: Superconductivity,* vol. 310, no. 1-4, pp. 16-29, 1998.

[31] R. Brambilla, F. Grilli and L. Martini, "Development of an edge-element model for AC loss computation of high-temperature superconductors," *Superconductor Science and Technology,* vol. 20, p. 16, 2007.

[32] A. Stenvall and T. Tarhasaari, "An eddy current vector potential formulation for estimating hysteresis losses of superconductors with FEM," *Superconductor Science and Technology,* vol. 23, p. 125013, 2010.

[33] L. Prigozhin, "Analysis of critical-state problems in type-II superconductivity," *Applied Superconductivity, IEEE Transactions on,* vol. 7, no. 4, pp. 3866-3873, 1997.

[34] Y. Mawatari, "Critical state of periodically arranged superconducting-strip lines in perpendicular fields," *Physical Review B,* vol. 54, no. 18, p. 13215, 1996.

[35] J. Gilchrist, "Flux diffusion and the porous medium equation," *Physica C: Superconductivity,* vol. 291, no. 1-2, pp. 132-142, 1997.

[36] R. Brambilla, F. Grilli, D. Nguyen, L. Martini and F. Sirois, "AC losses in thin superconductors: the integral equation method applied to stacks and windings," *Superconductor Science and Technology,* vol. 22, p. 075018, 2009.

[37] F. Grilli, R. Brambilla and L. Martini, "Modeling high-temperature superconducting tapes by means of edge finite elements," *Applied Superconductivity, IEEE Transactions on,* vol. 17, no. 2, pp. 3155-3158, 2007.

[38] J. Souc, E. Pardo, M. Vojenciak and F. Gomory, "Theoretical and experimental study of AC loss in high temperature superconductor single pancake coils," *Superconductor Science and Technology,* vol. 22, p. 015006, 2009.

[39] J. Clem, J. Claassen and Y. Mawatari, "AC losses in a finite Z stack using an anisotropic homogeneous-medium approximation," *Superconductor Science and Technology,* vol. 20, p. 1130, 2007.

[40] W. Yuan, A. Campbell and T. Coombs, "A model for calculating the AC losses of second-generation high temperature superconductor pancake coils," *Superconductor Science and Technology,* vol. 22, p. 075028, 2009.

[41] L. Prigozhin and V. Sokolovsky, "Computing AC losses in stacks of high-temperature superconducting tapes," *Supercond. Science and Tech.,* vol. 24, p. 075012, 2011.

[42] S. Foltyn, L. Civale, J. MacManus-Driscoll, Q. Jia, B. Maiorov, H. Wang and M. Maley, "Foltyn, SR and Civale, L. and MacManus-Driscoll, JL and Jia, QX and Maiorov, B. and Wang, H. and Maley, M.," *Nature materials,* vol. 6, no. 9, pp. 631-642, 2007.

[43] Q. Du, M. Gunzburger and J. Peterson, "Analysis and approximation of the Ginzburg-Landau model of superconductivity," *SIAM Review,* pp. 54-81, 1992.

[44] A. Bossavit, "Numerical modelling of superconductors in three dimensions: a model and a finite element method," *Magnetics, IEEE Trans. on,* vol. 30, no. 5, pp. 3363-3366, 1994.

[45] C. Bean, "Magnetization of hard superconductors," *Physical Review Letters,* vol. 8, no. 6, pp. 250-253, 1962.

[46] Y. Kim, C. Hempstead and A. Strnad, "Magnetization and critical supercurrents," *Physical Review,* vol. 129, no. 2, p. 528, 1963.

[47] J. Rhyner, "Magnetic properties and AC-losses of superconductors with power law current--voltage characteristics," *Physica C: Superconductivity,* vol. 212, no. 3-4, pp. 292-300, 1993.

[48] K. Thakur, A. Raj, E. Brandt, J. Kvitkovic and S. Pamidi, "Frequency-dependent critical current and transport ac loss of superconductor strip and Roebel cable," *Superconductor Science and Technology,* vol. 24, p. 065024, 2011.

[49] K. Kajikawa, T. Hayashi, R. Yoshida, M. Iwakuma and K. Funaki, "Numerical evaluation of AC losses in HTS wires with 2D FEM formulated by self magnetic field," *Applied Superconductivity, IEEE Transactions on,* vol. 13, no. 2, pp. 3630-3633, 2003.

[50] R. Pecher, M. McCulloch, S. Chapman, L. Prigozhin and C. Elliot, "3D-modelling of bulk type-II superconductors using unconstrained H-formulation," 2003.

[51] Z. Hong, A. Campbell and T. Coombs, "Numerical solution of critical state in superconductivity by finite element software," *Superconductor Science and Technology,* vol. 19, p. 1246, 2006.

[52] D. Nguyen, S. Ashworth, J. Willis, F. Sirois and F. Grilli, "A new finite-element method simulation model for computing AC loss in roll assisted biaxially textured substrate YBCO tapes," *Superconductor Science and Technology,* vol. 23, p. 025001, 2010.

[53] W. Smythe, Static and dynamic electricity, McGraw-Hill, 1967.

[54] J. Jackson, Classical electrodynamics, Wiley, 1975.

[55] PDE Solutions Inc, "FlexPDE," 2011. [Online]. Available: http://www.pdesolutions.com. [Accessed 11 11 2011].

[56] COMSOL Multiphysics, "COMSOL," 2011. [Online]. Available: www.comsol.com. [Accessed 11 11 2011].

[57] COMSOL Multiphysics, COMSOL Multiphysics Reference Guide, 2011.

[58] COMSOL Multiphysics, COMSOL Multiphysics User's Guide, 2011.

[59] W. Zimmerman, Multiphysics modelling with finite element methods, World Scientific, 2006.

[60] A. Hindmarsh, P. Brown, K. Grant, S. Lee, R. Serban, D. Shumaker and C. Woodward, "SUNDIALS: Suite of nonlinear and differential/algebraic equation solvers," *ACM Transactions on Mathematical Software (TOMS),* vol. 31, no. 3, pp. 363-396, 2005.

[61] V. Rodriguez-Zermeno, M. Soerensen, N. Pedersen, N. Mijatovic and A. Abrahamsen, "Fast 2D Simulation of Superconductors: a Multiscale Approach," in *Proceedings of the COMSOL Conference*, Milan, 2009.

[62] V. Rodriguez-Zermeno, N. Mijatovic, C. Traeholt, T. Zirngibl, E. Seiler, A. Abrahamsen, N. Pedersen and M. Sorensen, "Towards Faster FEM Simulation of Thin Film Superconductors: A Multiscale Approach," *Applied Superconductivity, IEEE Transactions on,* no. 99, pp. 1-1, 2011.

[63] M. Ainslie, V. Rodriguez-Zermeno, Z. Hong, W. Yuan, T. Flack and T. Coombs, "An improved FEM model for computing transport AC loss in coils made of RABiTS YBCO coated conductors for electric machines," *Superconductor Science and Technology,* vol. 24, p. 045005, 2011.

[64] S. Terzieva, M. Vojenciak, E. Pardo, F. Grilli, A. Drechsler, A. Kling, A. Kudymow, F. Gomory and W. Goldacker, "Transport and magnetization ac losses of ROEBEL assembled coated conductor cables: measurements and calculations," *Superconductor Science and Technology,* vol. 23, p. 014023, 2010.

[65] W. Goldacker, A. Frank, A. Kudymow, R. Heller, A. Kling, S. Terzieva and C. Schmidt, "Status of high transport current ROEBEL assembled coated conductor cables," *Superconductor Science and Technology,* vol. 22, p. 034003, 2009.

[66] K. Thakur, M. Staines, L. Lakshmi and N. Long, "Numerical computation of AC losses and flux profiles in high-aspect-ratio superconducting strips in perpendicular AC magnetic

field," *App. Supercond., IEEE Trans.,* vol. 19, no. 6, pp. 3770-3778, 2009.

[67] P. Knupp, "Remarks on mesh quality," in *45th AIAA Sciences Meeting and Exhibit*, Reno NV , 2007.

[68] F. Grilli, F. Sirois, S. Brault, R. Brambilla, L. Martini, D. Nguyen and W. Goldacker, "Edge and top/bottom losses in non-inductive coated conductor coils with small separation between tapes," *Superconductor Science and Technology,* vol. 23, p. 034017, 2010.

[69] E. Seiler, T. Zirngibl, N. Mijatovic, C. Tr{\ae}holt, J. Christensen and A. Abrahamsen, "AC loss in superconducting wires operating in a wind turbine like generator," in *IOP Publishing*, 2010.

[70] American Superconducor Corporation, "AMSC," 2011. [Online]. Available: http://www.amsc.com/. [Accessed 11 11 2011].

[71] W. Norris, "Calculation of hysteresis losses in hard superconductors carrying ac: isolated conductors and edges of thin sheets," *Journal of Physics D: Applied Physics,* vol. 3, p. 489, 1970.

[72] D. Lide, CRC handbook of chemistry and physics: a ready-reference book of chemical and physical data, CRC Press, 2004.

[73] J. Lu, E. Choi and H. Zhou, "Physical properties of Hastelloy C-276™ at cryogenic temperatures," *Journal of Applied Physics,* vol. 103, p. 064908, 2008.

[74] N. Mijatovic, B. Jensen, A. Abrahamsen, V. Zermeno, C. Traeholt and N. Pedersen, "Coil Optimization for High Temperature Superconductor Machines," *Applied Superconductivity, IEEE Transactions on,* vol. 21, no. 3, pp. 1136-40 , 2011.

[75] COMSOLl Multiphyscs, AC/DC Module Model Library (COMSOL 3.5a), 2008.

[76] Y. Iwasa, Case studies in superconducting magnets: design and operational issues, Springer Verlag, 2009.

[77] N. Mijatovic, A. B. Abrahamsen, C. Traeholt, E. Seiler, M. Henriksen, V. M. Rodriguez-Zermeno and N. F. Pedersen, "Superconducting generators for wind turbines: design considerations," in *Journal of Physics: Conference Series 234 (2010) 032038. Presented at the 9th European Conference on Applied Superconductivity (EUCAS 09)*, 2010.

[78] N.Mijatovic, B.B.Jensen, C.Traeholt, A.B.Abrahamsen, V. Zermeno and N.F.Pedersen, "An HTS machine laboratory prototype (submited)," in *Proc. of the Joint Centennial Conference on App.Supercond. held in 2011 at The Hague, The Netherlands*, 2011.

Appendix A

Article 1

Rodriguez Zermeno, Victor Manuel; Sørensen, Mads Peter; Pedersen, Niels Falsig; Mijatovic, Nenad; Abrahamsen, Asger Bech. "*Fast 2D Simulation of Superconductors: a Multiscale Approach*". Presented at the 2009 COMSOL Conference, Milano, Italy. In proceedings (ISBN: 978-0-9825697-2-6) , pages: 1-6, 2009, COMSOL Inc.

Excerpt from the Proceedings of the COMSOL Conference 2009 Milan

Fast 2D Simulation of Superconductors: a Multiscale Approach

Victor M. Rodriguez-Zermeno*[1], Mads P. Sørensen[1], Niels Falsig Pedersen[2], Nenad Mijatovic[2]
and Asger B. Abrahamsen[3]
[1]DTU Mathematics, Lyngby, Denmark
[2]DTU Electrical Engineering, Lyngby, Denmark
[3]Materials Research Division, Risø - DTU, Roskilde, Denmark
*Corresponding author: Technical University of Denmark, Matematiktorvet, Building 303S,
2800 Kgs. Lyngby, Denmark, V.Zermeno@mat.dtu.dk

Abstract: This work presents a method to calculate AC losses in thin conductors such as the commercially available second generation superconducting wires through a multiscale meshing technique. The main idea is to use large aspect ratio elements to accurately simulate thin material layers. For a single thin superconductor, several standard test cases are simulated including transport current, externally applied magnetic field and a combination of both. The results are in good agreement with recently published numerical simulations and show even faster time to solution. A couple of examples involving several thin conductors in different circumstances are also shown.

Keywords: Superconductors, Multiscale Methods, AC-losses, Mapped Mesh, Coupling Variables.

1. Introduction

The increasing use of superconducting coated conductors and the recent introduction of High Power superconducting machines (1) (2) (3), demand a fast and reliable tool to simulate the performance of electromagnetic devices with superconducting components.

One of the biggest issues regarding 2D simulation of AC loses in superconductors for various power applications is the substantial invested time to obtain realistic results. This includes both the actual computing time and, more importantly, the time spent modeling every single application. Therefore, necessary steps must be taken to reduce both contributors to a minimum and make simulation of the electromagnetic properties of superconductors as easy and fast as possible.

In the last years, several approaches have been proposed to address this problem relying on the use of the finite element simulations a few are found in (4) (5) (6) (7) (8) and references therein. However, all PDE based formulations are still limited by the expensive computation of superconducting materials and the increased number of elements in the case of thin conductors such as the second generation superconducting wires that contain a micron thick superconducting layer.

Here, we present a way to simulate superconductors in a timely effective manner. The simulation is based on previously published models (5) (8) and an existing implementation using COMSOL (9). Use of a multiscale approach allows creating custom made applications rapidly and with ease.

2. Governing Equations

Following a formulation originally proposed in (8), the magnetic field strength is calculated by solving:

$$\nabla \times (\rho \nabla \times \boldsymbol{H}) = -\mu \frac{\partial}{\partial t} \boldsymbol{H}$$

here, ρ is constant for regular conductors but for superconductors:

$$\rho = \frac{E_c}{J_c} \left(\frac{|\boldsymbol{J}|}{J_c} \right)^{n-1}$$

where $\boldsymbol{J} = \nabla \times \boldsymbol{H}$ is the current density, μ is the permeability of the material, E_c is the electric field strength of 1 μV/cm obtained when the current density reaches the critical current density J_c and n characterizes how abruptly the transition from the superconducting to normal state is taking place. Coated conductors are generally anisotropic with $J_c(\theta, |B|)$ and $n(\theta, |B|)$ depending on the angle between the conductor and the magnetic flux density, but here they are assumed isotropic and constant. Finally, following a procedure similar to the one described in (5), an initial condition $\boldsymbol{H} = \boldsymbol{0}$ at $t = 0$ is used to satisfy the uniqueness of the solution $\boldsymbol{H}$ for $t > 0$.

For the case where no external field is applied, Neumann boundary conditions are used in a large enough domain. Dirichlet boundary conditions are used to include the contribution of external magnetic fields. Also, in the case of several conductors, integral constrains are utilized to ensure that currents are limited to their respective conductors. Finally, the AC losses per unit length for a periodic current signal can be calculated following:

$$Q = \oint dt \int \boldsymbol{E} \cdot \boldsymbol{J}\, dS$$

3. Use of COMSOL Multiphysics

All computations take place inside a domain at least 10 times larger than the maximum length of the conductor or array of conductors under consideration.

Recalling the resistivity dependence upon the current density for superconducting materials, it is important to point out that this dependence on the current density, makes it impossible to use COMSOL's AC/DC module, otherwise a circular reference would be created for $\boldsymbol{J}$. Therefore the PDE mode application is used to simulate the above described model:

$$\mathrm{e_a}\frac{\partial^2 \mathbf{u}}{\partial \mathrm{t}^2} + \mathrm{d_a}\frac{\partial \mathbf{u}}{\partial \mathrm{t}} + \nabla \cdot \Gamma = \mathrm{F}$$

where:

$$\mathbf{u} = \boldsymbol{H} = \begin{bmatrix} H_\mathrm{x} \\ H_\mathrm{y} \end{bmatrix},$$

$$\mathrm{e_a} = \begin{bmatrix} 0 & 0 \\ 0 & 0 \end{bmatrix},$$

$$\mathrm{d_a} = \begin{bmatrix} \mu & 0 \\ 0 & \mu \end{bmatrix},$$

$$\Gamma = \rho\left(\frac{\partial H_\mathrm{y}}{\partial \mathrm{x}} - \frac{\partial H_\mathrm{x}}{\partial \mathrm{y}}\right)\begin{bmatrix} 0 & 1 \\ -1 & 0 \end{bmatrix} \quad \text{and}$$

$$\mathrm{F} = \begin{bmatrix} 0 \\ 0 \end{bmatrix}$$

For regular conductors ρ is a positive constant, but for superconducting materials the following relation holds:

$$\rho = \frac{E_c}{J_c}\left(\frac{\left|\frac{\partial H_\mathrm{y}}{\partial \mathrm{x}} - \frac{\partial H_\mathrm{x}}{\partial \mathrm{y}}\right|}{J_c}\right)^{n-1} \qquad \text{and}$$

The initial conditions are as follows:

$$\boldsymbol{H}|_{\boldsymbol{t=0}} = \begin{bmatrix} 0 \\ 0 \end{bmatrix}$$

As described in the previous section, for the case of zero external applied Magnetic Field, Neumann boundary conditions can be used. In the case of externally applied field, Dirichlet boundary conditions are applied, such that at the boundary of the overall domain the Magnetic field equals the sum of both self and external contributions. The self contributions $\boldsymbol{H}_\mathbf{s} = [H_\mathrm{sx}, H_\mathrm{sy}]$ are calculated using Ampere's law. Whereas the external contributions are simply put as $\boldsymbol{H}_\mathbf{e} = [H_\mathrm{ex}, H_\mathrm{ey}]$. The boundary conditions are then as follows:

$$\boldsymbol{H}|_{\boldsymbol{\partial\Omega}} = \begin{bmatrix} H_\mathrm{sx} + H_\mathrm{ex} \\ H_\mathrm{sy} + H_\mathrm{ey} \end{bmatrix}$$

For the case of conductors carrying externally applied electric currents and following (8), integral constrains are used. An integration coupling variable is defined in every conductor to obtain an expression for the total current passing through, the k^{th} conductor C_k:

$$I_k = \int_{C_k} J_z dS$$

An integral constrain is then defined at a given point (it can also be edge or subdomain) to force a net current.

The most important original contribution of this work refers to the use of structured meshes or mapped meshes as referred to in COMSOL. The most significant drawback in using free meshes for the formulation published in (4-8) is the fact that for thin material layers (either normal or superconducting), the number of elements increases heavily with the growing aspect ratio of the layer. This is because the meshing algorithm builds elements with individual aspect ratio close to unity. Therefore individual elements "resemble" either equilateral triangles or squares. It is this large difference in aspect ratios that makes the number of elements increase heavily. In consequence, the number of degrees of freedom (DOF) is largely augmented and so is the computational time as it depends upon the square of the number of DOF.

This has large consequences for the simulation of second generation superconducting wires such as the commercially available 344 coated conductors manufactured by American Superconductor since the aspect ratio of the superconducting layer in such wires can be higher than 4000. It is important to notice that this big scale difference in the conductor width/thickness could be addressed with a multiscale mesh; such mesh elements should have an aspect ratio between 1 and the aspect ratio of the conductor itself. Although no complete study of the optimal aspect ratio for the mesh elements was carried out, aspect ratios in excess of 100 provided good results.

To cope with this multiscale problem, in this work, structured (mapped) meshes were used inside the thin layers, allowing 75 elements for the width and 2 (or 4) for the thickness of the layer. This gives a mesh element aspect ratio of 80 (or 160). As a mere exercise, as many as 20 elements were used for the thickness with no significant differences in the overall computed AC-losses (data not reported here).

Finally, AC losses are computed directly in COMSOL by means of an integrator i.e. adding one ODE as a global equation to calculate Q as defined in section 2 as follows:

$$\dot{\xi} = f\,P,\ \ t \in \left(t_0, t_0 + \frac{1}{f}\right) \text{ and } \xi(t_0) = 0$$

where ξ is a dummy variable, f is the reciprocal of the period of the current signal (or external magnetic field), t_0 is an arbitrary time value such that the transitory behavior of the solutions has already passed and P is a subdomain integration coupling variable defined in the regions of interest as:

$$P = \int E_z\,J_z dS$$

Use of integrators has proven to be the most efficient way in terms of time as does not add any significant time to the simulation and requires no external postprocessing with its implied manual data export.

For the case of sinusoidal currents (or external magnetic field), only half a cycle is used in the integrator ξ to calculate the losses.

Unless otherwise stated all simulations were performed in complete domains without making symmetry simplifications. All times referred in the following sections correspond to calculations performed using the blade server of the Technical University of Denmark (DTU): dual quad-core Intel(R) Xeon(R) E5440 CPUs running at 2.83Ghz with 32GB memory available (2GB per processor). All simulations were carried out with the UMFPACK solver which essentially uses only one processor, however in practice; use of two processors increases the speed by 40%. No increase in speed was noticed when using more than two processors.

4. Results

Following the procedure mentioned above, the cases of transport current and applied external field were considered as in (10). AC losses were calculated for a conductor of width 3mm and thickness of 1μm. J_c and n were assigned values of 10^{10}A m^{-2} and 25 respectively. A finite resistivity of 1 Ω·m was used for the air surrounding the superconducting material. The permeability was assumed to be equal to its free space value. Finally, all signals were sinusoidal with frequency of 50 Hz. Figure 1 depicts the overall domain, along with its corresponding mesh.

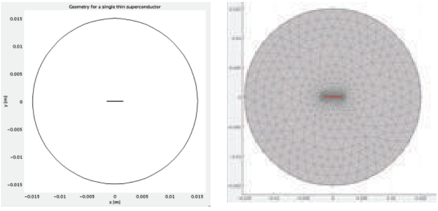

Figure 1. Thin superconductor surrounded by air (axes display longitudes in meters).

As described in the previous section, a mapped mesh was used in the superconducting region Figure 2 shows an overall picture of the mesh and some close ups.

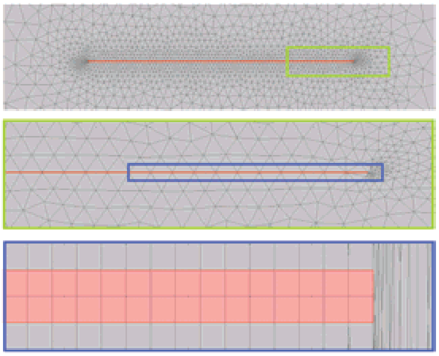

Figure 2. Mesh. The superconductor domain is colored in pink. The two upper figures show details of the mesh close to the superconducting region. The lower figure is deformed to allow the mesh elements in the superconductor to have an apparent aspect ratio of 1 rather than 80.

The instantaneous AC losses for a single tape carrying 90% of its critical current value are shown in Figure 3. Every single peak accounts for half a cycle of the original sinusoidal signal. Notice that after the first one all the following peaks are equal, thus the transitory effects after the first cycle can be disregarded. This allows to calculate the AC losses by simulating only one cycle.

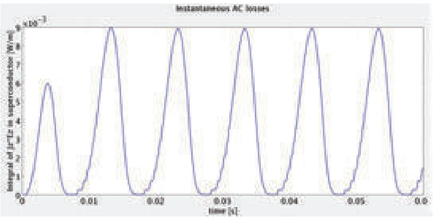

Figure 3. Instantaneous losses.

In order to validate the approach proposed in this work and its relevance, in Figures 4 and 5 the calculated results are compared with the ones published in the one that to the best of our knowledge, offered the fastest strategy to accurately calculate AC-losses in superconducting thin layers (10). Notice that our calculations are in good agreement with the aforementioned previously published numerical calculations.

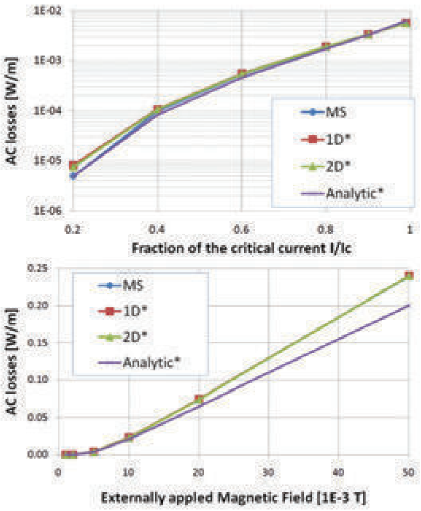

Figure 4. Comparison of calculated AC losses for different values of transport current (top) and for different values of the externally applied Magnetic Field (bottom). The "MS" curve refers to our calculations. * (10)

In the same way, computing time for the same publication is compared with our calculations in Figure 5. Here, it is important to notice that the use of mapped meshes allowed us to perform calculations 2 to 3 orders of magnitude faster than with regular meshing for a full 2-D simulation. Moreover, both our 2 and 4 elements calculations ran up to five times faster than the reported computing time for the 1D formulation proposed in (10).

Finally, in Figures 6 to 10, we present a few examples of computations involving several conductors.

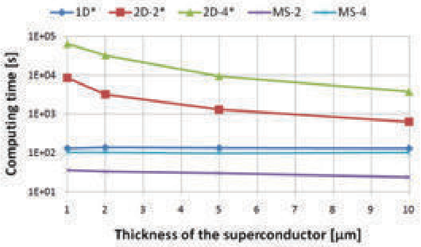

Figure 5. Comparison of computing times. The "MS-

2(4)" curve refers to our calculations when 2(4) elements were used across the thickness. * (10)

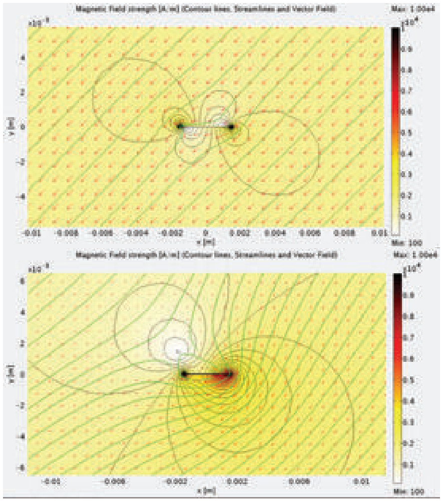

Figure 6. Comparison of the Magnetic Field Intensity for a thin superconductor when a sinusoidal Magnetic Field of 2 mT is applied (peak value shown). Both cases when no current (top) and 80% critical current is applied (bottom).

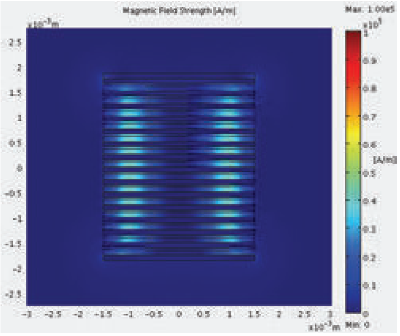

Figure 7. AC electric currents ($0.9Ic$, $50Hz$, in phase) are applied to a stack of 15 coated conductors. Magnetic field strength at 0 phase. For this particular application, a substrate with a relative permeability of 50 was considered.

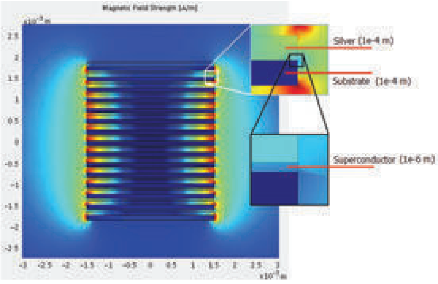

Figure 8. AC electric currents ($0.9Ic$, $50Hz$, in phase) are applied to a stack of 15 coated conductors. Magnetic field strength at peak value. As in Figure 7, a substrate with a relative permeability of 50 was considered. The insert shows the thickness of the different layers.

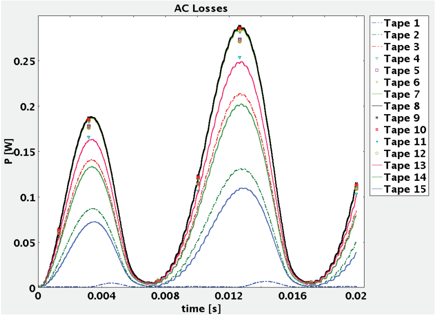

Figure 9. Instantaneous AC losses in the conductors depicted in Fig. 7 and 8 (enumerated from the top). Observe that the higher losses are experienced by the central conductors. Also, notice that the top conductors (tapes 1, 2 and 3) experience less loss than their bottom counterparts (tapes 13, 14 and 15).

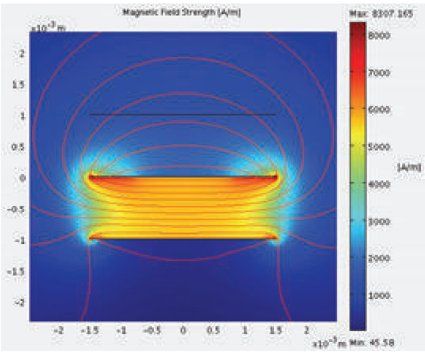

Figure 10. Interaction among several thin conductors. Top: Silver, no external current. Center: superconducting, imposed AC transport current ($0.9Ic$,

$50Hz$). Bottom: superconducting, no external transport current. Notice how the field is expelled from the bottom conductor.

The results shown in this work correspond to a full domain 2D simulation and no symmetry simplifications were used to reduce the computing time. Although all the calculations were performed in DTU's blade server as described in Section 3, a simple test calculation of AC losses in commercially available coated conductors was carried out in less than two minutes using a laptop.

5. Conclusions

Use of mapped meshes and specifically, use of large aspect ratio elements, provides a considerable increase in the computing speed for calculation of AC losses in superconductors. Numerical simulations were performed showing a decrease up to 3 orders of magnitude in the computing time when compared with other 2D simulation were no mapped meshes are used.

Furthermore, although it could be argued that the computer used in the present work is different than the one used in the reference, the proposed approach offers a method that can be used just like any other Multiphysics module in COMSOL, allowing to couple as many conductors as required in one single module. In this way, the time spent modeling every single application while using large aspect ratio elements does not depend heavily in the number of conductors and offers similar computing time than the 1D formulation. Therefore, the work presented here offers a faster time to solution strategy for calculating AC losses.

Finally, the ease to set a problem using the proposed formulation makes it possible to think of further applications such as superconducting coils, and superconducting induction machinery, among others in the near future.

6. References

1. **Superconductor, American.** Superconductor Motors & Generators. [Online] [Cited: September 1, 2009.] http://www.amsc.com/products/motorsgenerators/index.html.

2. *5 MW High Temperature Superconductor Ship Propulsion Motor Design and Test Results.* **Eckels, P. W., Snitchler, G.** Naval Engineers Journal, Vol. 117, No. 4. (2005), pp. 31-36.

3. *Basic concepts, status, opportunities, and challenges of electrical machines utilizing high-temperature superconducting (HTS) windings.* **J Frauenhofer, J Grundmann, G Klaus and W Nick.** 2008, 8th European Conference on Applied Superconductivity (EUCAS 2007) J. Phys.: Conf. Ser. 97 012189.

4. *Numerical analysis of high-temperature superconductors with the critical-state model.* **Farinon, S. Fabbricatore, P. Gomory, F. Greco, M. Seiler, E.** IEEE Transactions on Applied Superconductivity June 2005, Volume: 15, Issue: 2, Part 3, pages: 2867- 2870.

5. *"Numerical Evaluation of AC Losses in HTS Wires With 2D FEM Formulated by Self Magnetic Field".* **Kazuhiro Kajikawa, Toshihiro Hayashi, Ryoji Yoshida, Masataka Iwakuma, and Kazuo Funaki,.** IEEE TRANS. ON APPLIED SUPERCONDUCTIVITY, VOL. 13, NO. 2, JUNE 2003.

6. *AC losses in high-temperature superconductors: revisiting the fundamentals of the loss modelling.* **Lahtinen, Jaakko Paasi and Markku.** Physica C: Superconductivity Volume 310, Issues 1-4, December 1998, Pages 57-61.

7. *Numerical modelings of superconducting wires for AC loss calculations.* **Naoyuki Amemiya, Shun-ichi Murasawa, Nobuya Banno and Kengo Miyamoto.** Physica C: Superconductivity Volume 310, Issues 1-4, December 1998, Pages 16-29.

8. *"Development of an edge-element model for AC loss computation of high-temperature superconductors".* **R. Brambilla, F. Grilli, and L. Martini.** Superconductor Science and Technology, vol. 20, pp. 16–24, 2007.

9. *ACDC Module/Model Library/Superconducting wire.* **FILES, COMSOL DOCUMENTATION.**

10. *Integral equations for the current density in thin conductors and their solution by the finite-element method.* **Roberto Brambilla, Francesco Grilli, Luciano Martini and Frédéric Sirois.** Superconductor Science and Technology (2008) Volume 21, Number 10.

Appendix B

Article 2

Rodriguez-Zermeno, V.M.; Mijatovic, N.; Traeholt, C.; Zirngibl, T.; Seiler, E.; Abrahamsen, A.B.; Pedersen, N.F.; Sorensen, M.P.; “Towards Faster FEM Simulation of Thin Film Superconductors: A Multiscale Approach”. IEEE TRANSACTIONS ON APPLIED SUPERCONDUCTIVITY, VOL. 21, NO. 3, JUNE 2011

Towards Faster FEM Simulation of Thin Film Superconductors: A Multiscale Approach

V. M. Rodriguez-Zermeno, N. Mijatovic, *Student Member, IEEE*, C. Træholt, T. Zirngibl, E. Seiler,
A. B. Abrahamsen, N. F. Pedersen, and M. P. Sørensen

***Abstract*—This work presents a method to simulate the electromagnetic properties of superconductors with high aspect ratio such as the commercially available second generation superconducting YBCO tapes. The method is based on a multiscale representation for both thickness and width of the superconducting domains. A couple of test cases were successfully simulated and further investigations were made by means of structured (mapped) meshes. Here, large aspect ratio elements were used to simulate thin material layers with a reduced number of elements. Hence, more complex geometries can be studied at considerable lower computational time. Several test cases were simulated including transport current, externally applied magnetic field and a combination of both. The results are in good agreement with recently published numerical simulations. The computational time to solve the present multiscale approach in 2D is estimated as two orders of magnitude faster than other 2D methods.**

***Index Terms*—AC losses, finite element methods, high temperature superconductors, superconducting coils.**

I. INTRODUCTION

THE large aspect ratio of 2G superconducting tapes is a matter of concern for the numerical simulation of its electromagnetic properties [1], [2]. Meshing of thin layers using elements with aspect ratio close to unity puts a big constrain in the number of degrees of freedom to be solved for. In the particular case of 2G superconducting wires, the layers have aspect ratios in the order of $10^3 \sim 10^4$. Therefore, simulation of systems involving several conductors proves to be a rather cumbersome task.

So far, several methods have been proposed to overcome this burden: use of 1D approaches that neglect the thickness of the superconducting layer [1] and implementation of geometries with a lower aspect ratio along with scaled current density values [2], among others. However, the problem persists as the aforementioned methods are either based upon extrapolation of calculations for lower aspect ratio domains; or do not provide very accurate results for the case where low transport currents and small separation among multiple conductors.

The large aspect ratio of the thin film conductors makes clear that the superconducting material is located in a multiscale domain: thickness and width are in different spatial scales. Here, we present a way to simulate superconductors in a timely effective manner. The simulation is based on previously published models [3], [4] and an existing implementation using COMSOL [5]. The use of this multiscale approach allows creating custom made applications rapidly and with ease.

II. GOVERNING EQUATIONS

Following a formulation originally proposed in [4], the magnetic field strength is calculated by solving:

$$\nabla \times (\rho \nabla \times H) = -\mu \frac{\partial H}{\partial t}, \tag{1}$$

where μ is the permeability; the resistivity ρ is a constant for normal conductors but for superconductors it is given by the following power law:

$$\rho = \frac{E_c}{J_c} \left(\frac{|J|}{J_c} \right)^{n-1}, \tag{2}$$

here the current density $J = \nabla \times H$; E_c is the electric field strength of 1 $\mu\mathrm{V/cm}$ obtained when the current density reaches the critical current density J_c and n characterizes how abruptly the transition from the superconducting to normal state is taking place.

To impose an explicit transport current in each of several conductors, integral constraints are used, so that the total electric current can be arbitrarily specified by means of a function of time. In this case, Neumann boundary conditions were used. For the case when an external magnetic field was applied, appropriate Dirichlet boundary conditions were selected.

III. STRUCTURED (MAPPED) MESHES

Traditional meshing techniques use elements with aspect ratio close to unity to discretize a domain [6]. Their use in thin layers (either normal or superconducting) poses a significant drawback. This is due to the fact that the number of elements increases heavily with the growing aspect ratio of the layer. As a result, the number of degrees of freedom is augmented and so is the computing time. This has important consequences for the simulation of second generation superconducting tapes since the aspect ratio of the superconducting layer in such conductors can be as high as 10^4.

Manuscript received August 18, 2010; accepted October 31, 2010. Date of publication December 17, 2010; date of current version May 27, 2011. This work was supported in part by the Technical University of Denmark, The Research School of the Danish Center for Applied Mathematics and Mechanics, Vestas Wind Systems and SEP-Mexico.

V. M. Rodriguez-Zermeno and M. P. Sørensen are with the Department of Mathematics, Technical University of Denmark, Kgs. Lyngby 2800, Denmark (e-mail: V.Zermeno@mat.dtu.dk).

N. Mijatovic, C. Træholt, and N. F. Pedersen, are with the Department of Electrical Engineering, Technical University of Denmark Kgs. Lyngby 2800, Denmark.

A. B. Abrahamsen, T. Zirngibl and E. Seiler are with Risø National Laboratory for Sustainable Energy, Materials Research Division, Technical University of Denmark, Roskilde, Denmark.

Color versions of one or more of the figures in this paper are available online at http://ieeexplore.ieee.org.

Digital Object Identifier 10.1109/TASC.2010.2091388

1051-8223/$26.00 © 2010 IEEE

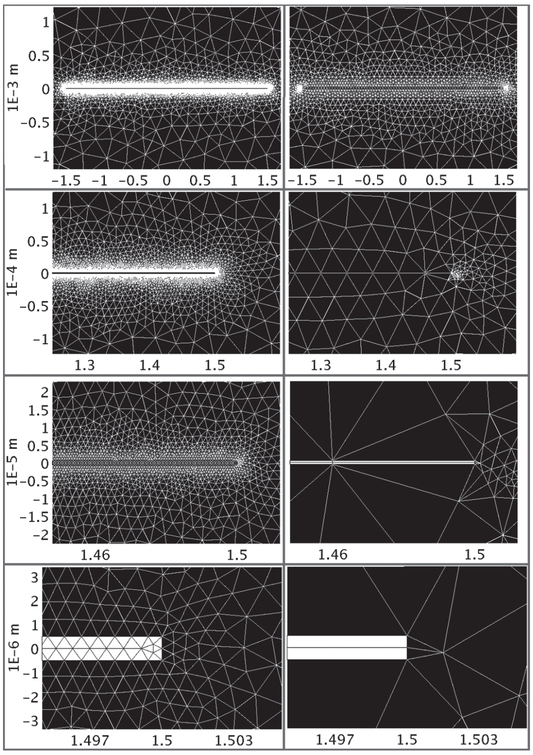

Fig. 1. Consecutive zoom of the mesh in and around a superconducting strip of 3 mm by 1 $\mu\mathrm{m}$. The horizontal scale is in mm in all subfigures. Left column: using free meshes 17150 elements were needed to discretize the superconducting region. Right column: using mapped meshes only 150 were necessary for the same purpose.

The big scale difference in the conductor width/thickness can be dealt with by means of a multiscale mesh. The aspect ratio of such mesh elements should, up to some degree, resemble the conductor's own aspect ratio. In this work, aspect ratios in excess of 100 provided good results, but the optimal aspect ratio for the mesh elements was not investigated.

Structured (mapped) meshes were implemented in all thin layers, allowing for 75 elements for the width and 2 (or 4) for the thickness of each layer. Therefore, mesh element aspect ratios of 80 (or 160) were obtained. Fig. 1 shows a comparison of both free and structured meshing approaches.

IV. RESULTS

A. Validation

To test the proposed meshing technique, the cases of transport current and applied external field exposed in [1] were considered. AC losses were calculated for a superconducting strip of 3 mm of width and thickness of 1 $\mu\mathrm{m}$. J_c and n were assigned values of $10^{10}\ \mathrm{A/m^2}$ and 25 respectively. For the air (or vacuum) surrounding the conductor, a finite resistivity of $1\ \Omega\cdot\mathrm{m}$ was used. The relative permeability was assumed to be equal to unity. All transport currents and externally applied fields were sinusoidal signals with frequency of 50 Hz. The comparison of the calculated values is shown in Figs. 2 and 3.

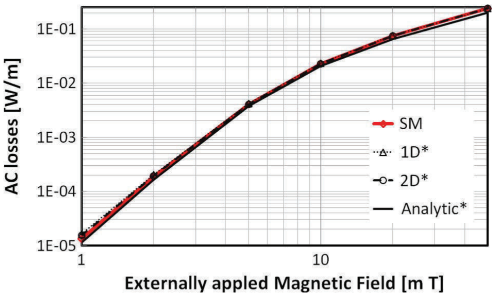

Fig. 2. Comparison of calculated AC losses for different values of externally applied AC Magnetic Field. The SM label corresponds to our calculations and the labels with the symbol $*$ to published results in [1].

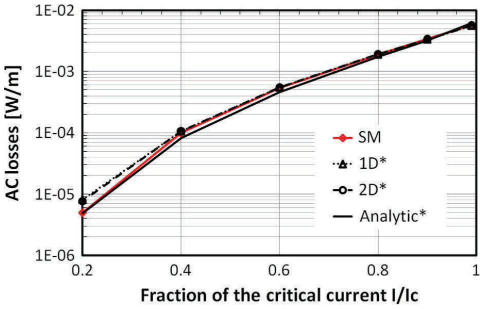

Fig. 3. Comparison of calculated AC losses for different values of AC transport current. The SM label corresponds to our calculations and the labels with the symbol $*$ to published results in [1].

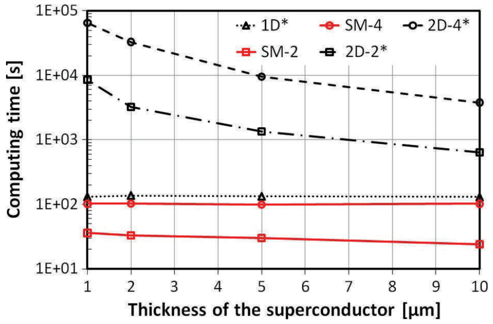

Fig. 4. Computing time for a full cycle at 50 Hz. The SM-2 and SM-4 curves refer to our calculation with 2 or 4 elements across the thickness, respectively. The labels with the symbol $*$ correspond to results published in [1].

Note that for both considered cases, the numerical results are in good agreement with the previously published numerical computations. Comparison of the computing time for the same publication [1] with our calculations is shown in Fig. 4.

It is relevant to point out that the use of mapped meshes allowed for calculations to be performed 2 to 3 orders of magnitude faster than with regular free meshing for a full 2-D simu-

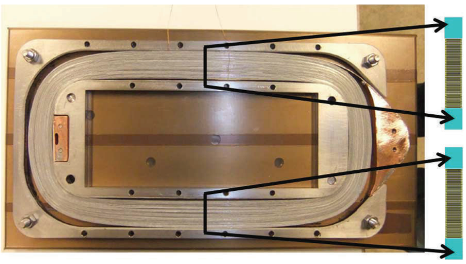

Fig. 5. Left: Racetrack coil from the Superwind project [7]. The coil consists of 57 turns of the commercially available Copper Laminated Amperium Wire from American Superconductors [8]. Right: geometrical representation used to model the cross section of the coil.

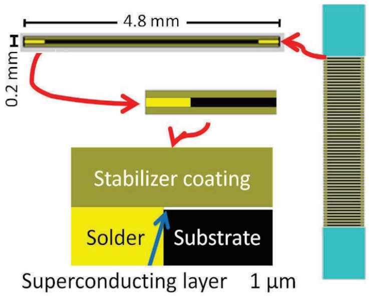

Fig. 6. Model of the coil used for simulations. Left: Wire structure including all layers in true aspect ratios. Each tape is an accurate reproduction of the commercially available Copper Laminated Amperium Wire from American Superconductors [8]. Right: cross section of the racetrack coil.

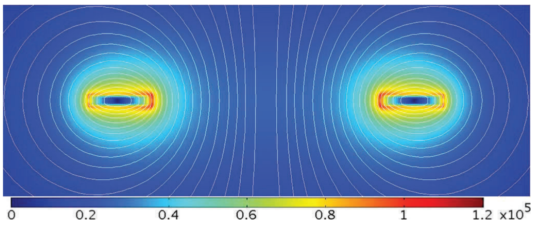

Fig. 7. Magnetic Field Intensity [A/m] for the cross section of the coil at peak current value. The stream lines show the magnetic field lines. For simplicity the geometric features were removed.

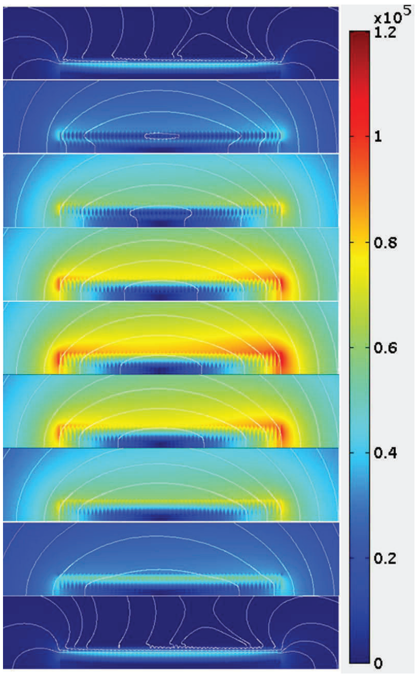

Fig. 8. Magnetic field intensity [A/m] at different phase values (from top to bottom, from π to 2π in $\pi/8$ increments. The stream lines show the magnetic field lines. The geometric features were removed for clarity.

lation. Furthermore, calculations using mapped meshes with 2 and 4 elements used across the thickness were up to five times faster than the reported computing time for the 1D formulation proposed in [1].

B. Calculation of the Magnetic Field of a Racetrack Coil

To illustrate the potential of the method, the magnetic field produced by a racetrack coil of the Superwind project [7] was simulated. The coil is composed of 57 turns of the commercially available Copper Laminated Amperium Wire from American Superconductors [8]. Fig. 5 shows the actual architecture of the coil along with its corresponding modeled cross section.

Fig. 6 shows the model geometry used to perform simulations. The true thickness of the 1 $\mu\mathrm{m}$ superconducting layer is taken into account. For simplicity and taking advantage of the symmetry, only one quarter of the cross section of the coil was simulated. An AC current of $I = 65.8$ A, assuming a critical current value $I_c = 95$ A, at 50 Hz was evaluated for a tape with a n-value of 21 and a critical current density of J_c of $2.375 \times 10^{10}\ \mathrm{A/m^2}$. The simulation of a whole AC cycle was done under 6 hours using a single processor solver (UMFPACK).

Values for the resistivity of the hardened copper coating (6 $\mathrm{nOhm \cdot m}$), solder (30 $\mathrm{nOhm \cdot m}$) and substrate (65 $\mathrm{nOhm \cdot m}$) were obtained from [9] assuming an operating temperature of 77 K. The Magnetic Field Intensity for the whole cross section of the coil at a peak current value of 65.8 A is presented in Fig. 7. Also, the Magnetic Field Intensity at different phase values is shown in Fig. 8. For simplicity in comparison, only one quarter of the cross section is presented.

C. Calculation of AC Losses

AC losses were calculated for the previously mentioned Racetrack coil from the Superwind project [7]. Two approaches were followed, one assuming a constant value for $\mathrm{J_c} = 2.375^{\circ} \times 10^{10}\ \mathrm{A/m^2}$ and the other with the following empiric $\mathrm{J_c}(B)$ dependence: $J_c = 1/(a + bB_{||})$, where $B_{||}$ is the component of the magnetic field parallel to the c-axis, $a = 0.0104\ \mathrm{A^{-1}}$ and $b = 0.043\ \mathrm{A^{-1}T^{-1}}$. This relation was found experimentally testing the Copper Laminated Amperium

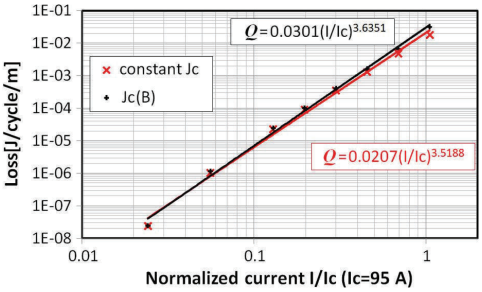

Fig. 9. Simulated AC losses Q at different values of $\mathrm{I}/\mathrm{I}_{\mathrm{c}}$.

Wire from American Superconductors [8] used to wind the coil (data not shown).

The calculated values for the AC losses Q (in J/cycle/m) are reported in Fig. 9. A power fit for both sets of data is also shown. Note that although both approaches with J_{c} being constant and as dependent on the magnetic field present a similar behavior, the losses assuming J_{c} as a constant are lower.

V. DISCUSSION

Use of mapped meshes with large aspect ratio elements allowed simulating the electromagnetic properties of superconducting materials in thin geometries faster than when using free meshes without compromising accuracy in the calculation of AC losses. Both transport and applied field cases were presented here. In the case of a single conductor, computational time was reduced by more than 2 orders of magnitude. Even though other electromagnetic formulations could be implemented, given enough validation, use of mapped meshes could be implemented to reduce the time to solution.

Although the aspect ratio values of 80 and 160 for the mesh elements used in this work provided accurate results consistent with previously published data, further studies upon finding an optimal mesh distribution are yet to be performed.

Whereas it could be argued that the computing time is similar to the one using integral equations for a single conductor, the 2D formulation with mapped meshes allows for simulating several conductors in arbitrary arrangements in one single equation, making the interaction among them natural and reducing the programming time.

Calculation of AC-losses was performed well under 6 hours for a real application racetrack coil conformed of 57 tapes. The obtained dependence of the AC loss on the current has been fitted by a power law as shown on Fig. 9. Exponents in the range 3.5–3.6 have been obtained and are in qualitative agreement with the analytical expression of an elliptical conductor [10].

Additional hysteretic losses should be expected from the magnetic substrate, which are not considered in this work. Future work will include such effects as well as comparison with experimental data.

VI. CONCLUSIONS

It has been shown how the use of mapped meshes allows simulating complex and fairly large coated conductor problems with ease and within manageable time. This permits to think about optimization or simulations of further applications like large magnets or superconducting motors and generators in the near future.

REFERENCES

[1] R. Brambilla, F. Grilli, L. Martini, and F. Sirois, "Integral equations for the current density in thin conductors and their solution by the finite element method," *Supercond. Sci. Technol.*, vol. 21, no. 10, pp. 105 008-1–105 008-8, Jul. 2008.

[2] K. P. Thakur, M. P. Staines, L. S. Lakshmi, and N. J. Long, "Numerical computation of AC losses and flux profiles in high-aspect-ratio superconducting strips in perpendicular AC magnetic field," *IEEE Trans. Appl. Supercond.*, vol. 19, no. 6, pp. 3770–3778, Dec. 2009.

[3] K. Kajikawa, T. Hayashi, R. Yoshida, M. Iwakuma, and K. Funaki, "Numerical evaluation of AC losses in HTS wires with 2D FEM formulated by self magnetic field," *IEEE Trans. Appl. Supercond.*, vol. 13, no. 2, Jun. 2003.

[4] R. Brambilla, F. Grilli, and L. Martini, "Development of an edge-element model for AC loss computation of high-temperature superconductors," *Supercond. Sci. Technol.*, vol. 20, pp. 16–24, 2007.

[5] COMSOL Multiphysics, "Superconductive wire," 2008 [Online]. Available: http://www.comsol.com/showroom/documentation/model/689/superconducting_wire_sbs.pdf

[6] P. M. Knupp, "Remarks on mesh quality," in *45th AIAA Aerospace Sc. Meeting Exhibit*, Reno, NV, Jan. 7–10, 2007.

[7] E. Seiler *et al.*, "AC loss in superconducting wires operating in a wind turbine like generator," *J. Physics: Conf. Series*, vol. 234, p. 032051, 2010.

[8] American Superconductor, "Amperium wire: Copper laminated," 2010 [Online]. Available: http://www.amsc.com/products/amperiumwire/copper.html

[9] K. Nam, C. Lee, D. K. Park, T. K. Ko, and B.-Y. Seok, "Thermal and electrical analysis of coated conductor under AC over-current," *IEEE Trans. Appl. Supercond.*, vol. 17, no. 2, pp. 1923–1926, Jun. 2007.

[10] W. T. Norris, "Calculation of hysteresis losses in hard superconductors carrying ac: Isolated conductors and edges of thin sheets," *J. Phys. D: Appl. Phys.*, vol. 3, p. 489, 1970.

Appendix C

Article 3

Mark D Ainslie, **Victor M Rodriguez-Zermeno**, Zhiyong Hong, Weijia Yuan, Timothy J Flack and Timothy A Coombs. “An improved FEM model for computing transport AC loss in coils made of RABiTS YBCO coated conductors for electric machines”. Supercond. Sci. Technol. 24 (2011) 045005 (8pp)

IOP PUBLISHING SUPERCONDUCTOR SCIENCE AND TECHNOLOGY

Supercond. Sci. Technol. **24** (2011) 045005 (8pp) doi:10.1088/0953-2048/24/4/045005

An improved FEM model for computing transport AC loss in coils made of RABiTS YBCO coated conductors for electric machines

Mark D Ainslie[1], **Victor M Rodriguez-Zermeno**[2], **Zhiyong Hong**[3], **Weijia Yuan**[1], **Timothy J Flack**[1] **and Timothy A Coombs**[1]

[1] Department of Engineering, University of Cambridge, 9 J J Thomson Avenue, Cambridge CB3 0FA, UK
[2] Department of Mathematics, Technical University of Denmark, Kongens Lyngby 2800, Denmark
[3] School of Electronic, Information and Electrical Engineering, Shanghai Jiao Tong University, Shanghai, People's Republic of China

E-mail: mda36@cam.ac.uk

Received 11 October 2010, in final form 6 January 2011
Published 27 January 2011
Online at stacks.iop.org/SUST/24/045005

Abstract

AC loss can be a significant problem for any applications that utilize or produce an AC current or magnetic field, such as an electric machine. The authors investigate the electromagnetic properties of high temperature superconductors with a particular focus on the AC loss in superconducting coils made from YBCO coated conductors for use in an all-superconducting electric machine. This paper presents an improved 2D finite element model for the cross-section of such coils, based on the H formulation. The model is used to calculate the transport AC loss of a racetrack-shaped coil using constant and magnetic field-dependent critical current densities, and the inclusion and exclusion of a magnetic substrate, as found in RABiTS (rolling-assisted biaxially textured substrate) YBCO coated conductors. The coil model is based on the superconducting stator coils used in the University of Cambridge EPEC Superconductivity Group's all-superconducting permanent magnet synchronous motor design. To validate the modeling results, the transport AC loss of a stator coil is measured using an electrical method based on inductive compensation by means of a variable mutual inductance. Finally, the implications of the findings on the performance of the motor are discussed.

(Some figures in this article are in colour only in the electronic version)

1. Introduction

The expected improved performance and efficiency over conventional devices has seen continued interest in introducing superconducting materials to electric power applications, such as transformers, cables, motors and generators. In electric machines, in particular, increasing the current and/or magnetic flux density increases the power density, which leads to reductions in both size and weight. High temperature superconductor-based (HTS) electric machines are said to be particularly attractive for low speed, high torque applications, such as wind turbines [1], and in electric-based transport applications where space and weight are at a premium, such as ship and aircraft propulsion [2, 3].

Investigating and modeling the electromagnetic behavior of superconductors is crucial to the design of superconductor-based electrical devices. In order for these devices to be cost- and performance-competitive with conventional devices, the use of superconducting materials and the associated cooling system must be shown to possess improved properties in comparison to their conventional counterparts. Although lossless for DC, superconductors do experience AC losses,

© 2011 IOP Publishing Ltd Printed in the UK & the USA

which can be a significant problem in any device exposed to a time-varying current or magnetic field. These AC losses increase the refrigeration load, which decreases the overall efficiency and increases the technological complexity of the design. Significant efforts have been made to understand the complex interactions between multiple superconducting coated conductors in quite simple geometries, but no reliable technique exists to both model and measure AC losses in more complex geometries, such as superconducting coils.

The finite element method (FEM) has been intensively used for modeling the electromagnetic properties of superconductors and for calculating the AC loss in HTS coated conductors. There are three main formulations used in this type of modeling: the A–V formulation (based on the magnetic vector potential **A**) [4–7], the T–Ω formulation (based on the current vector potential **T**) [8], and the H formulation (based on directly solving the magnetic field in 2D) [9–12]. Maxwell's equations can be written in each of these formulations and these formulations are equivalent in principle, but the solutions of the corresponding partial differential equations (PDEs) can be very different [13]. When designing superconductor devices, the choice of the formulation depends on a number of different factors, including accuracy and computational speed [14].

Methods based on the H formulation converge faster than other methods and it is easy to impose boundary conditions related to the current flowing in the coated conductor(s) and/or externally applied magnetic fields. In this paper, models based on the H formulation in 2D using edge elements [11, 13] are compared using different parameters. The cross-section of a racetrack coil used in the University of Cambridge's superconducting permanent magnet synchronous motor (hereafter, PMSM) design [15–17] is modeled using constant and magnetic field-dependent critical current densities, and the inclusion and exclusion of a magnetic substrate.

The model has been improved in comparison with previous models [17–19] by using a mapped mesh in and between the superconducting tapes to achieve a decrease of two orders of magnitude in the number of mesh elements, allowing the real superconducting layer thickness to be modeled without increasing computation time. Furthermore, the formulation has been enhanced to allow the inclusion of the magnetic substrate present in some YBCO coated conductors, whereas previous models have investigated only the YBCO layer itself.

The research was carried out using an Intel i7 2.67 GHz processor with 6 Gb of memory, and the software used is COMSOL Multiphysics 3.5a [20]. The time-dependent solver used is COMSOL's default linear system solver, UMFPACK. The default time stepping method uses variable-order, variable-step-size backward differentiation formulas (BDF), and the time steps are automatically selected by the solver.

2. Model, equations and results

A photograph and the dimensions of the superconducting racetrack coil under test are shown in figures 1 and 2, respectively, and the specification of the superconductor under analysis is listed in table 1. The coil consists of a double layer of YBCO coated conductor wound into a racetrack shape. There are 50 turns in each layer, resulting in 100 series turns for the coil. Approximately 60 m of American Superconductor's type 344 second generation (2G) coated conductor [21] was used to wind the coil.

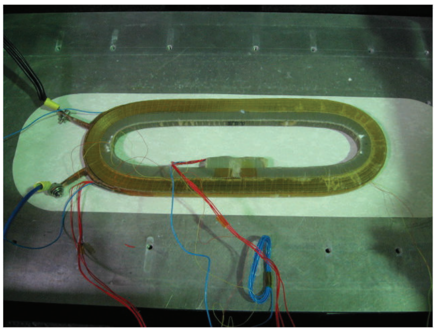

Figure 1. The superconducting racetrack coil under test.

Table 1. Specification of the superconductor under analysis.

Manufacturer	AMSC
Tape type	344
Critical current, I_c (self-field, 77 K)	100 A
n-value, n	21
Conductor width, w	4.35 mm
Conductor thickness, d_c	0.2 mm
YBCO layer thickness, d_{sc}	1 μm
Critical current density, YBCO layer, J_c	2.3×10^{10} A m^{-2}
Ferromagnetic (Ni–W) substrate thickness, d_{mag}	80 μm
Frequency, f	50 Hz

The model is a two-dimensional stack of coated conductors representing the cross-section of the coil. The coated conductors are assumed to be infinitely long in the z-direction, with the cross-section in the x–y plane. The model consists of three types of subdomains—the superconducting layer of each turn, the magnetic substrate, and the surrounding air. The geometry of the 2D model and its mesh is shown in figure 3—this is for the model using the actual thickness for the YBCO layer and including the magnetic substrate.

In a previous study by the authors [19], the artificial expansion of the YBCO layer in the model was investigated to improve the speed and convergence of the coated conductor model. Therefore, the number of mesh elements can be reduced without significant loss of accuracy, provided that the thickness of the layer is not artificially increased past a certain limit [19]. Significant improvements were made in [22, 23] by using large aspect ratio mapped meshes, hence reducing the number of mesh elements in and between the coated conductors. Overall, a reduction of about two orders of magnitude in the number of elements was achieved in comparison with previous simulations using free meshes, increasing the computation speed. Accordingly, the actual thickness of the YBCO layer can be modeled without a significant increase in computational time, allowing other

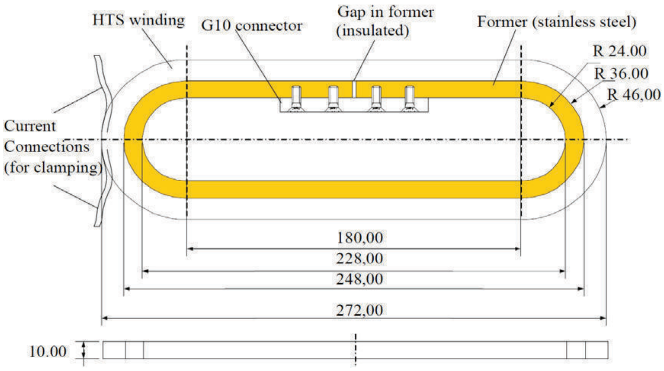

Figure 2. Dimensions (in mm) of the superconducting coil under test.

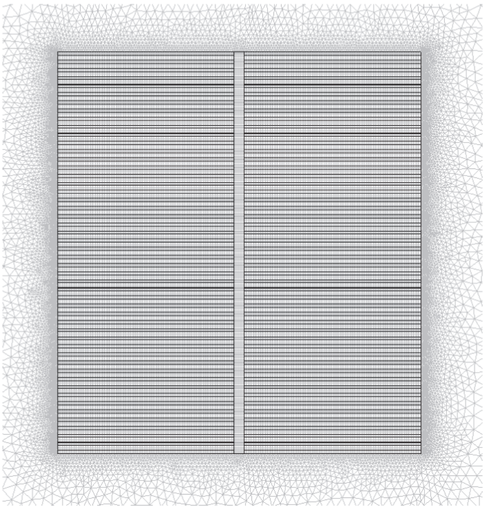

Figure 3. 2D model geometry and mesh using the actual thickness for the YBCO layer and including the magnetic substrate.

layers of the coated conductor, such as the stabilizer layer and substrate, to be implemented using accurate geometrical dimensions. As mentioned previously, edge elements (Nedelec elements implemented using the 'shcurl' element in COMSOL) are used instead of conventional Lagrange elements, which are the default element types in most commercial software packages.

The simplest approximation regarding the critical current density is that it is independent of ambient magnetic field [24]—although in reality, as Kim and Anderson showed in [25, 26], the critical current depends not only on the magnitude, but also the direction of the field. Field dependence of the critical current can be included in this model by modifying the equation for J_c, and examples of this modification can be found in [27–29]. The equation used in this model for the B-dependence of J_c is given by (1) and is based on manufacturer-supplied data for the tape's in-field performance for parallel and perpendicular fields:

$$J_c(\mathbf{B}) = \frac{J_c(\text{self field, 77 K})}{1 + 4|\mathbf{B}_y|}. \tag{1}$$

The effect of a ferromagnetic substrate on the superconductor layer for a single tape and simple stack configurations was investigated in [29–31]. For coated conductors with a ferromagnetic substrate, such as in the coil under test, the total AC loss consists of contributions from both the superconductor layer and the substrate. The hysteretic loss dominates the ferromagnetic loss for high AC currents and applied fields [29, 30, 32] and this finding should be amplified in the case of a coil consisting of many turns. The addition of the substrate into the model requires modification of the equations used by the authors in [17–19]—this modification is described below. Eddy current losses in the normal metal stabilizer layer of the superconductor are assumed negligible.

The governing equations are derived from Maxwell's equations—Faraday's law (2) and Ampere's law (3). These equations give a resulting set of PDEs, which differ depending on the permeability of the material being modeled. For non-magnetic subdomains (with a relative permeability of $\mu_r = 1$), such as the superconducting layer and air, the resulting PDEs are described by (4*a*), (4*b*) and (6). This was used in previous works [17–19], where the effect of the magnetic substrate was ignored. For magnetic subdomains—with a relative permeability $\mu_r \neq 1$ that is not a constant, but varies with magnetic field as in real materials, i.e. $\mu_r(H)$, where H is the magnitude of the magnetic field—the resulting PDEs are described by (5*a*), (5*b*) and (6). Additionally, the E–J power law (7) is used to describe the macroscopic behavior of the HTS.

$$\nabla \times \mathbf{E} = -\frac{\partial \mathbf{B}}{\partial t} = -\frac{\partial(\mu_0\mu_r\mathbf{H})}{\partial t} \tag{2}$$

$$\nabla \times \mathbf{H} = \mathbf{J} \tag{3}$$

$$\frac{\partial E_z}{\partial x} = \mu_0 \frac{\partial H_y}{\partial t} \tag{4a}$$

$$\frac{\partial E_z}{\partial y} = -\mu_0 \frac{\partial H_x}{\partial t} \tag{4b}$$

$$\frac{\partial E_z}{\partial x} = \mu_0 \left[\frac{\partial \mu_{\rm r}(H)}{\partial t} H_y + \mu_{\rm r}(H) \frac{\partial H_y}{\partial t} \right] \tag{5a}$$

$$\frac{\partial E_z}{\partial y} = -\mu_0 \left[\frac{\partial \mu_{\rm r}(H)}{\partial t} H_x + \mu_{\rm r}(H) \frac{\partial H_x}{\partial t} \right] \tag{5b}$$

$$\mathbf{J}_z = \frac{\partial H_x}{\partial y} - \frac{\partial H_y}{\partial x} \tag{6}$$

$$\mathbf{E}_z = E_0 \left(\frac{J_z}{J_{\rm c}} \right)^{n-1} \frac{\mathbf{J}_z}{J_{\rm c}}. \tag{7}$$

In the 2D model, there are two dependent variables, H_x and H_y, representing the components of the magnetic field in the x and y directions, respectively. The induced electric field and current density have only a z-component, and these are represented by E_z and J_z. The electrical behavior of the superconducting material is modeled by the E–J power law with the characteristic voltage $E_0 = 1\ \mu\text{V cm}^{-1}$ and $n = 21$. The n-value is identified from DC measurements of the superconductor's highly nonlinear I–V characteristic, and is usually within the range of 5–30 for type-II superconductors [33]. E_0 is the voltage across the superconductor when it is carrying the critical current density $J_{\rm c}$.

The model requires appropriate settings for the boundary conditions and since no externally applied magnetic field exists, Dirichlet boundary conditions are applied to the air subdomain with $H_x = 0$ for the y axis boundaries and $H_y = 0$ for the x axis boundaries. Neumann boundary conditions are applied to the boundaries of the superconductor and magnetic substrate subdomains.

To include the field dependence of the relative magnetic permeability of the Ni–W ferromagnetic substrate of the RABiTS YBCO coated conductor, the fitting function presented in [30] is used, which is based on the experimental results published in [34]. The function is represented by (8) [30]:

$$\mu(H) = 1 + 30\,600(1 - \exp(-(H/295)^{2.5}))H^{-0.81} + 45\exp(-(H/120)^{2.5}) \tag{8}$$

where H is the amplitude of the magnetic field strength $H = \sqrt{H_x^2 + H_y^2}$.

For all models, the superconductor hysteretic loss $Q_{\rm sc}$ is calculated using the critical current density and the electric field distribution across the cross-section of each YBCO layer. For the model including the magnetic substrate, the additional ferromagnetic loss $Q_{\rm fe}$ is calculated using the fitting function presented in [30], which is again based on the experimental results published in [30]. The loss, in J/cycle m^{-3}, is calculated based on the maximum value of the magnetic flux density seen by the substrate and is represented by (9) [30]:

$$Q_{\rm fe}(B_{\rm max}) = \begin{cases} 4611.4 B_{\rm max}^{1.884} & B_{\rm max} \leqslant 0.164 \\ 210(1 - \exp(-(6.5 B_{\rm max})^4)) & B_{\rm max} > 0.164. \end{cases} \tag{9}$$

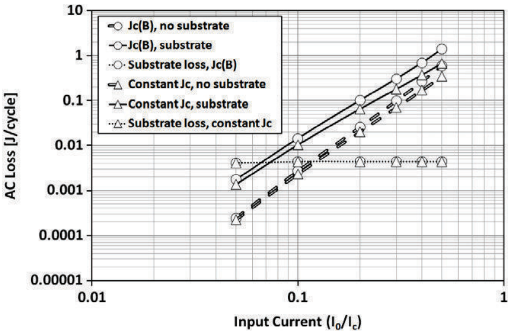

Figure 4. Comparison of calculated AC loss for constant $J_{\rm c}$ and $J_{\rm c}(B)$ dependence and inclusion and exclusion of the magnetic substrate.

Figure 4 shows the calculated AC loss for four different cases. Firstly, the individual turns are modeled without the magnetic substrate using a constant $J_{\rm c}$, then using the $J_{\rm c}(B)$ equation introduced earlier. Next, the magnetic substrate is included in the model with a constant $J_{\rm c}$, then $J_{\rm c}(B)$. The substrate loss is indicated by the dotted lines. The $J_{\rm c}(B)$ dependence increases the AC loss as the magnetic flux front penetrates further into the stack of tapes along the y axis due to the reduced $J_{\rm c}$ from the edges inwards where the magnetic field is strongest. The inclusion of the magnetic substrate in the model also increases the AC loss, but not necessarily due to the ferromagnetic substrate loss itself, and the reason for the loss increase will be discussed in more detail below. For the range of current investigated in the model (5–50 A), the substrate is saturated (or very close to saturation), and the loss in the superconductor layer is larger than the substrate loss by an order of magnitude or higher for current in excess of about 20 A (20% of the tape $I_{\rm c}$, 40% of the coil $I_{\rm c}$). In this range, the effect of the substrate loss itself on the overall AC loss is minimal and can be neglected; however, for low current, the substrate loss cannot be neglected, and can exceed the superconductor hysteretic loss for a suitably low current. Additionally, the total AC loss for the model with the magnetic substrate and B-dependent $J_{\rm c}$ can be seen to be the sum of the AC loss calculated in the constant $J_{\rm c}$/substrate and $J_{\rm c}(B)$/no substrate models.

Figures 5 and 6 show the magnetic flux density profiles of the magnetic field perpendicular to the tape faces $|\mathbf{B}_y|$, which has the greatest impact on the AC loss due to the large aspect ratio of the coated conductor, for models excluding (figure 5) and including (figure 6) the magnetic substrate, both with $J_{\rm c}(B)$. Without a magnetic substrate, the magnetic flux front penetrates from the edges of the tape towards the center in a fairly consistent manner from the top tape in the stack to the bottom. However, when the magnetic substrate is included, the flux front changes shape to an almost triangular one, and penetrates furthest in the middle of the stack and least in the top and bottom tapes. The same trend is observed when a constant $J_{\rm c}$ is used, which is not included here.

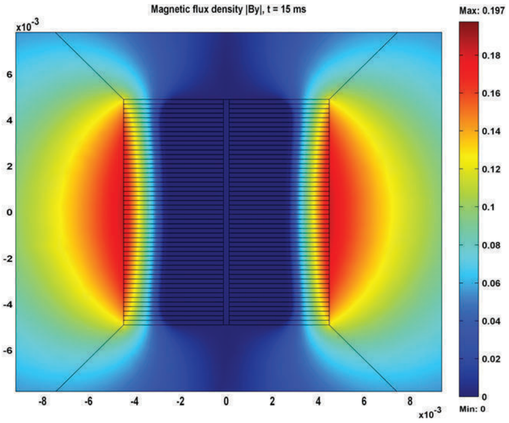

Figure 5. Magnetic flux density profile of the magnetic field perpendicular to the tape faces $|\mathbf{B}_y|$ without a magnetic substrate and with $J_c(B)$ at $t = 15$ ms (peak of applied current $|\mathbf{I}_0| = 50$ A).

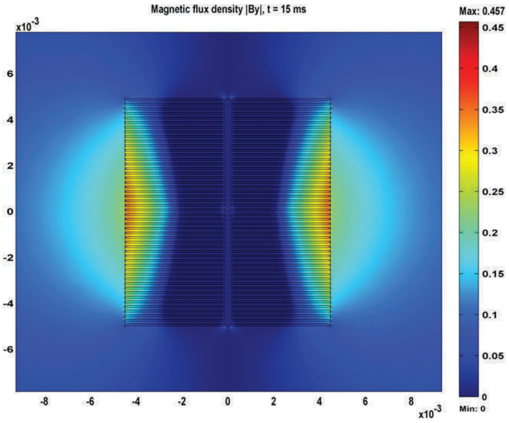

Figure 6. Magnetic flux density profile of the magnetic field perpendicular to the tape faces $|\mathbf{B}_y|$ with a magnetic substrate and $J_c(B)$ at $t = 15$ ms (peak of applied current $|\mathbf{I}_0| = 50$ A).

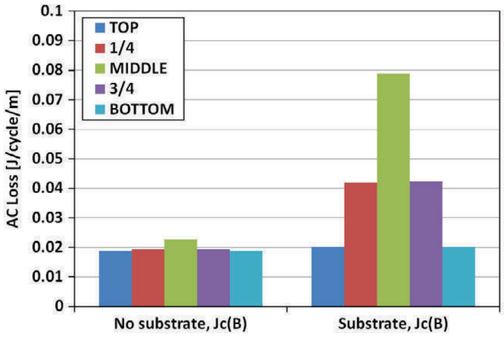

Figure 7. Comparison of AC loss for tapes at different locations within the cross-section for $J_c(B)$ models with and without a magnetic substrate for an applied current $\mathbf{I}_0 = 50$ A.

The increase in loss can be attributed to (1) the increased penetration into the middle of the stack, and (2) the higher magnetic flux density within the penetrated region of the superconducting tapes. The higher magnetic flux density in the superconductor is due to the presence of the magnetic substrate and the increased penetration arises due to a local region of large permeability around the middle of the entire stack at the peak of the input current—although the magnetic field strength $|\mathbf{H}|$ in this region is relatively low in comparison to $|\mathbf{H}_{\max}|$ for the whole stack ($<10^4$ A m^{-1}), according to (8), the peak in the curve of the relative magnetic permeability for the substrate is around 400 A m^{-1}. As shown in figure 4, the contribution of $Q_{\rm fe}$ (the ferromagnetic substrate loss) is negligible.

Figure 7 shows a comparison of the AC loss for tapes at different locations within the stack (here 1/4 refers to the 12th tape from the top of the stack and 3/4 refers to the 38th tape). The difference in the AC loss between tapes is minimal for no magnetic substrate and a triangular distribution (with highest losses in the middle tapes) can be observed when the magnetic substrate is present. The overall loss is significantly higher in the latter case, when compared to the former.

3. Experimental setup and results

3.1. Experimental setup

In order to measure the transport AC loss of the superconducting coil, electrical and calorimetric methods can be used. Calorimetric methods are advantageous for AC loss measurements in complex magnetic environments, such as those found in real superconductor-based devices [35]. However, calorimetric methods have a number of drawbacks in comparison to electrical methods, including the long time required to obtain a stationary regime, extensive calibration required due to heat losses other than the superconductor AC loss, and the fact that individual components of loss cannot be measured [36].

The experimental setup is shown in figure 8 and is based on a combination of a modified existing experimental setup used for measuring the transport AC loss of superconducting tapes [37] with a compensation coil to cancel the large inductive component of the superconducting coil, which can be orders of magnitude higher than the AC loss component. The compensation coil needs to provide a high enough compensating voltage with low phase shift and low noise.

Power is supplied via two 400 W KEPCO power supplies connected in parallel (one master, one slave) to provide up to ±20 V, ±40 A. The output of the power supplies is controlled by the internal oscillator of the lock-in amplifier. The current flowing in the circuit is measured by a current transducer connected to an Agilent multimeter, and the input signal to the lock-in amplifier is the compensated superconducting coil voltage. The critical current of the coil, measured in [16], is approximately 50 A. The coil is contained within a liquid nitrogen bath, and is connected in series with the power

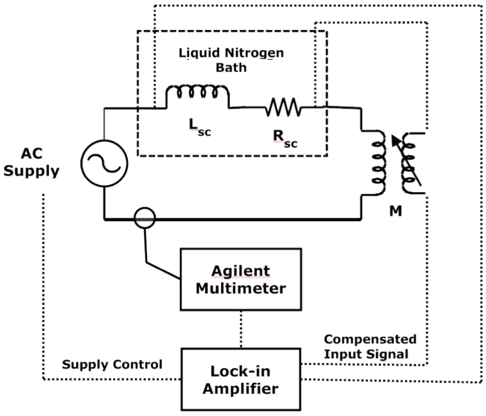

Figure 8. Experimental setup for electrical AC loss measurement.

supplies and the compensation coil. The signal from the voltage taps at either end of the superconducting coil is connected in series, but with opposite polarity, to the secondary of the compensation coil.

A compensation coil is used rather than capacitive compensation to avoid the effects of higher harmonics, which make capacitive compensation very frequency sensitive. It is much easier to design a variable mutual inductance. A voltage divider is not used to reduce the superconducting coil signal as this may introduce a phase shift and reflection [38], so a large mutual inductance must be provided. As thin a wire as possible is used for both the primary and secondary coils to reduce the effect of any induced eddy currents in the windings due to time-varying magnetic fields and, for the same reason, no magnetic materials are used in the construction of the coils. The variation of the mutual inductance is achieved by displacing the secondary coils relative to the primary, whose axes are parallel to each other.

The primary coil is wound with 2.18 mm diameter enameled copper wire with $N_1 = 20$ turns and is 5 cm long. The secondary coil is wound with 0.314 mm diameter enameled copper wire with $N_2 = 3000$ turns and is also 5 cm long. Thicker wire was used on the primary to enable large currents (up to 50 A) through this coil. Plastic plumbing pipe was used as the former for the primary (5 inch pipe) and secondary (4 inch pipe) coils.

The compensation coil was designed with a mutual inductance higher than the estimated 3 mH of the racetrack coil. Assuming perfect flux linkage between the primary and secondary, the compensation coil mutual inductance was calculated to be 9.4 mH, by (10):

$$M = \mu_0 N_1 N_2 \frac{\pi}{2} \frac{r_2^2}{r_1} \tag{10}$$

where r_1 and r_2 are the radii of the primary and secondary coils, respectively.

The superconducting coil voltage is compensated such that

$$v_{\mathrm{sc}} - v_{\mathrm{comp}} = v_{\mathrm{AC}} \tag{11}$$

where v_{AC} is the AC loss component. Equation (12) shows the components of (11) in more detail:

$$\left(i\, R_{\mathrm{sc}} + L_{\mathrm{sc}} \frac{\partial i}{\mathrm{d}t} \right) - M \frac{\partial i}{\mathrm{d}t} = i\, R_{\mathrm{sc}}. \tag{12}$$

Therefore, for complete compensation $L_{\mathrm{sc}} = M$. For an input current $i(t) = I_0 \sin(\omega t)$, the inductive voltage across the superconducting coil is $\omega L_{\mathrm{sc}} I_0 \cos(\omega t)$. The resistance of the compensation coil's secondary coil can be ignored due to the large input impedance of the lock-in amplifier (10 MΩ).

3.2. Experimental results

The range of the mutual inductance of the compensation coil was measured for varied displacement levels of primary versus secondary coil. Using a function generator (50 Hz signal) and an oscilloscope, the mutual inductance was measured to vary between 6.6 mH (no displacement) and 1 mH (9 cm displacement).

The inductance of the superconducting coil was measured by applying a small current (0.6 A) after cooling the coil in a liquid nitrogen bath, and measuring the coil voltage with the lock-in amplifier. At such a low current, the superconducting coil voltage is expected to be predominately inductive. A frequency of 41.7 Hz was used to avoid using a frequency too close to the mains frequency. The inductance was measured as 2.74 mH, close to the estimated 3 mH.

The compensation coil was then connected to the lock-in amplifier (without the superconducting coil) and was adjusted until a voltage equal to the measured superconducting coil voltage was displayed on the lock-in amplifier. The superconducting and compensation coil signals were connected in series, ensuring opposite polarities to cancel the inductive component and achieve the required compensation. The setting of the phase of the lock-in was performed using its internal reference, which also provides the control signal to the power supply. The phase setting was performed initially, and the same phase was used for subsequent measurements. The current transducer is used only for the purpose of measuring the magnitude of the current flowing in the circuit and does not provide a reference to the lock-in. The experimental results for two sets of measurements are shown in figure 9. The power supply described above was able to provide up to approximately 25 A.

In analytical models based on the critical state approximation, the AC loss has a cubic or quartic dependence [24, 39, 40]; however, for currents greater than 10 A, the measured AC loss tends towards a square law relationship, suggesting that the actual phase had drifted from the original phase setting. As the transport current increases, the AC loss voltage increases at a faster rate than the inductive voltage, which increases linearly, and this results in a phase shift from the original setting. Future experiments will include improvement of the phase setting in order to obtain more accurate results over a wider range of current.

However, these results highlight the potential of the model in calculating AC loss—in particular, the improved model of the coil cross-section, which models superconducting and

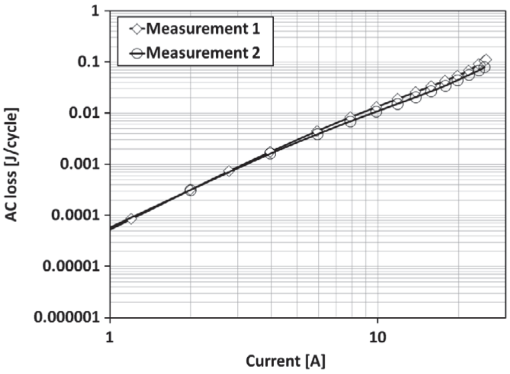

Figure 9. Experimental results for the transport AC loss measurement of the superconducting racetrack coil.

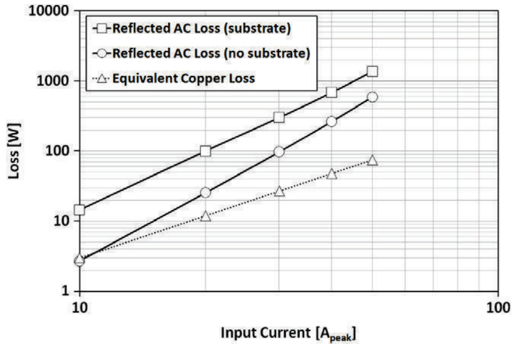

Figure 10. Comparison of the superconducting coil transport AC loss ($J_c(B)$ models with and without the magnetic substrate) with an equivalent copper coil.

magnetic substrate layers that are geometrically accurate, can estimate the AC loss of a superconducting coil. In addition to the phase setting improvement above, another improvement that can be made to the experimental technique is to use the split compensation coil described in [36, 38] to reduce the potential of stray magnetic fields affecting the measured signals.

4. Discussion

The AC losses must be kept to a very low level because any heating occurring at the low temperatures required to maintain superconductivity needs a large amount of refrigeration power. Using an HTS at liquid nitrogen temperatures (e.g. 77 K), Carnot efficiency would suggest about 4 W of cooling power is needed for 1 W of heat. In reality, Carnot efficiency is never reached, and assuming a 20% efficient cooling system, in this scenario about 20 W is required for every watt of heat. Here, a comparison is made between the superconducting coil's transport AC loss and the resistive loss of a similar coil wound with room temperature copper conductor. Although the ductility of copper allows for better distribution of the coil windings within the stator, in order to simplify the analysis, the same coil dimensions as the superconducting coil are assumed, including the same length of conductor, i.e. 60 m. The resistivity of the copper can be calculated by $R = \frac{\rho l}{A}$ where $\rho = 1.68\times10^{-8}\ \Omega$ m (at 20 °C), $l = 60$ m and $A = \pi r^2$. Here r is the radius of conductor required to carry a maximum current (in rms) comparable to the critical current of the superconducting coil. For example, AWG five wire (diameter 4.620 26 mm) carries a maximum 47 A_{rms} current [41]. Using the previous equation, the resistivity is 0.0601 Ω. Therefore, for $I = 50\ A_{peak}$ (35.35 A_{rms}), $P = 75.13$ W; for $I = 40\ A_{peak}$ (28.28 A_{rms}), $P = 48.08$ W; and so on. A comparison of the simulation results and the equivalent copper coil is shown in figure 10. The superconducting coil AC losses are reflected to room temperature by $P_{ref} = 20P_{AC}$ and given in units of W assuming a frequency of 50 Hz. This shows that at least an order of magnitude reduction in the AC loss is required for the coil to have comparable performance to that of copper at power frequencies such as 50 Hz. Reducing the frequency of the supply to the machine to a few Hz will also reduce the loss by an order of magnitude, making it feasible for this type of coil to be used in high torque, low speed applications, such as wind turbines.

A comparison can also be made between the transport AC loss reflected to room temperature and the output power of the motor. In [17], the output power of the machine was calculated as 4.52 kW for an electrical loading of 40 A_{peak} and a trapped field in the rotor poles (comprising YBCO bulks) of 0.4 T. In the machine design there are six stator coils meaning the total reflected transport AC loss of the superconducting PMSM is $P_{total} = 6 \times 20 \times P_{AC}$. Therefore, for 40 A_{peak}, the total reflected loss is 1.59 kW (no substrate, $J_c(B)$ model) and 4.14 kW (substrate, $J_c(B)$ model), and these correspond to approximately 35% and 92% of the motor output power, respectively. For 20 A_{peak}, the output power was calculated to be 2.26 kW [17], so the reflected loss (153 W—no substrate, 602 W—substrate) corresponds to approximately 7% and 27% of the motor output power, respectively.

From these results, it is clear that serious investigations need to be carried out in the area of AC loss mitigation for all-superconducting machine design—for example, shielding using superconducting or magnetic materials or tape striation. The magnetic flux density profile for coils wound from a coated conductor with a magnetic substrate raises some interesting points for further analysis. Improvement of the in-field performance of YBCO coated conductors is also required to improve the performance of coated conductor wound coils.

5. Conclusion

In this paper, an improved 2D finite element model based on the H formulation was described, which is implemented in COMSOL Multiphysics and models the cross-section of the coil as a stack of individual tapes. The model was used to investigate the electromagnetic properties of and calculate the transport AC loss in a superconducting racetrack coil for use in an all-superconducting motor. The model improves on previous models by modeling the actual thickness of the superconducting layer (instead of an artificially expanded thickness) and uses a mapped mesh consisting of large aspect ratio rectangular elements to improve computational speed and reduce the number of elements in and between each tape. A modified formulation was introduced to include a ferromagnetic substrate and models were compared with (e.g. RABiTS coated conductors) and without (e.g. IBAD coated conductors) magnetic substrates. The AC loss increases when a magnetic substrate is present in the model—not necessarily due to the presence of a ferromagnetic substrate loss, but due to the different composition of the magnetic flux front penetrating into the stack of tapes in the direction perpendicular to the tape faces. For relatively low current, the substrate loss cannot be neglected and can exceed the superconductor hysteretic loss, but for practical values of current, the substrate loss can be neglected.

The transport AC loss of a stator coil was measured using an electrical method based on inductive compensation with a variable mutual inductance. The experimental results verify the validity of the model for estimating the AC loss, but also indicate that improvements can be made to increase the accuracy of the setup, particularly in regard to the phase setting of the lock-in amplifier.

The transport AC loss is compared with an equivalent room temperature copper coil by reflecting the AC loss to room temperature taking into account Carnot efficiency and the efficiency of the cryocooler. The AC loss is found to be an order of magnitude higher in the case of the superconducting coil. When compared to the output power of the machine, the reflected loss can be seen to have a significant impact on the machine. These findings indicate that serious investigations need to be made in the area of AC loss mitigation for all-superconducting machine design in order to make these types of machines performance-competitive with existing machines.

References

[1] Fee M, Staines M P, Buckley R G, Watterson P A and Zhu J G 2003 *IEEE Trans. Appl. Supercond.* **13** 2193
[2] Gubser D U 2003 *Physica* C **392–396** 1192
[3] Masson P J, Breschi M, Tixador P and Luongo C A 2007 *IEEE Trans. Appl. Supercond.* **17** 1533
[4] Barnes G, McCulloch M and Dew-Hughes D 1999 *Supercond. Sci. Technol.* **13** 518–22
[5] Stavrev S, Grill F, Dutoit B, Nibbio N, Vinot E, Klutsch I, Meunier G, Tixador P, Yang Y and Martinez E 2002 *IEEE Trans. Magn.* **38** 849–52
[6] Prigozhin L 1997 *IEEE Trans. Appl. Supercond.* **7** 3866–73
[7] Campbell A M 2009 *Supercond. Sci. Technol.* **22** 034005
[8] Amemiya N, Miyamoto K, Murasawa S, Mukai H and Ohmatsu K 1998 *Physica* C **310** 30–5
[9] Kajikawa K, Hayashi T, Yoshida R, Iwakuma M and Funaki K 2003 *IEEE Trans. Appl. Supercond.* **13** 3630–3
[10] Hong Z, Campbell A M and Coombs T A 2006 *Supercond. Sci. Technol.* **19** 1246–52
[11] Brambilla R, Grilli F and Martini L 2007 *Supercond. Sci. Technol.* **20** 16–24
[12] Sirois F, Dione M, Roy F, Grilli F and Dutoit B 2007 *J. Phys.: Conf. Ser.* **97** 012030
[13] Grilli F, Brambilla R and Martini L 2007 *IEEE Trans. Appl. Supercond.* **17** 3155–8
[14] Grilli F, Sirois F, Brault S, Brambilla R, Martini L, Nguyen D N and Goldacker W 2010 *Supercond. Sci. Technol.* **23** 034017
[15] Jiang Y, Pei R, Hong Z, Jiang Q and Coombs T A 2008 *J. Phys.: Conf. Ser.* **97** 012123
[16] Jiang Y, Pei R, Xian W, Hong Z and Coombs T A 2008 *Supercond. Sci. Technol.* **21** 065011
[17] Ainslie M D, Jiang Y, Xian W, Hong Z, Yuan W, Pei R, Flack T J and Coombs T A 2010 *Physica* C **470** 1752–5
[18] Ainslie M D, Yuan W, Hong Z, Pei R, Flack T J and Coombs T A 2011 *IEEE Trans. Appl. Supercond.* doi:10.1109/TASC.2010.2089484
[19] Ainslie M D, Flack T J, Hong Z and Coombs T A 2011 *COMPEL, Intl. J. Comput. Math. Electr. Electron. Eng.* at press
[20] COMSOL, Inc. http://www.comsol.com
[21] American Superconductor http://www.amsc.com
[22] Rodriguez-Zermeno V M, Sørensen M P, Pedersen N F, Mijatovic N and Abrahamsen A B 2009 *Proc. Comsol Conf. 2009 (Milan)*
[23] Rodriguez-Zermeno V M, Mijatovic N, Træholt C, Zirngibl T, Seiler E, Abrahamsen A B, Pedersen N F and Sørensen M P 2011 *IEEE Trans. Appl. Supercond.* at press
[24] Norris W T 1970 *J. Phys. D: Appl. Phys.* **3** 489–507
[25] Kim Y B, Hampstead C F and Strnad A R 1963 *Phys. Rev. Lett.* **9** 306–9
[26] Anderson P W 1963 *Phys. Rev. Lett.* **9** 309–11
[27] Souc J, Pardo E, Vojenciak M and Gomory F 2009 *Supercond. Sci. Technol.* **22** 015006
[28] Stavrev S, Grilli F, Dutoit B and Ashworth S P 2005 *Supercond. Sci. Technol.* **18** 1300–12
[29] Gomory F, Vojenciak M, Pardo E, Solovyov M and Souc J 2010 *Supercond. Sci. Technol.* **23** 034012
[30] Nguyen D N, Ashworth S P, Willis J O, Sirois F and Grilli F 2010 *Supercond. Sci. Technol.* **23** 025001
[31] Majoros M, Ye L, Velichko A V, Coombs T A, Sumption M D and Collings E W 2007 *Supercond. Sci. Technol.* **20** S299–304
[32] Duckworth R 2007 *Flux Pinning and AC Loss Studies on YBCO Coated Conductors* ed M P Paranthaman and V Selvamanickam (New York: Nova Science) pp 281–98
[33] Grilli F, Stavrev S, Le Floch Y, Costa-Bouzo M, Vinot E, Klutsch I, Meunier G, Tixador P and Dutoit B 2005 *IEEE Trans. Appl. Supercond.* **15** 17–25
[34] Miyagi D, Yunoki Y, Umabuchi M, Takahashi N and Tsukamoto O 2008 *Physica* C **468** 1743–6
[35] Dolez P, Aubin M, Zhu W and Cave J 1998 *Supercond. Sci. Technol.* **11** 1386–90
[36] Kokavec J, Hlasnik I and Fukui S 1993 *IEEE Trans. Appl. Supercond.* **3** 153–5
[37] Pei R, Velichko A, Majoros M, Jiang Y, Viznichenko R, Hong Z, Marchant R, Campbell A M and Coombs T A 2008 *IEEE Trans. Appl. Supercond.* **18** 1236–9
[38] Daffix H and Tixador P 1997 *IEEE Trans. Appl. Supercond.* **7** 286–9
[39] Oomen M P 2007 *Flux Pinning and AC Loss Studies on YBCO Coated Conductors* ed M P Paranthaman and V Selvamanickam (New York: Nova Science) pp 375–404
[40] Yuan W, Campbell A M and Coombs T A 2009 *Supercond. Sci. Technol.* **22** 075028
[41] PowerStream Technologies http://www.powerstream.com/Wire_Size.htm

Appendix D

Article 4

Victor M.R. Zermeno, Asger B. Abrahamsen, Nenad Mijatovic, Mads Peter Sorensen, Bogi B. Jensen, Niels F. Pedersen. “Simulation of an HTS Synchronous Superconducting Generator” Presented at the Joint Centennial Conference on Applied Superconductivity held in 2011 at The Hague, The Netherlands. Manuscript accepted for publication in a special issue of Physics Procedia due by July 2012.

Available online at www.sciencedirect.com

ScienceDirect

Physics Procedia 00 (2011) 000–000

Physics Procedia

www.elsevier.com/locate/procedia

Superconductivity Centennial Conference

Simulation of an HTS Synchronous Superconducting Generator

Victor M.R. Zermeno[a]* Asger B. Abrahamsen[b] Nenad Mijatovic[c] Mads Peter Sorensen[a], Bogi B. Jensen[c], Niels F. Pedersen[a]

[a]*Department of Mathematics, Technical University of Denmark, Matematiktorvet 303S, Kgs. Lyngby 2800, Denmark*
[b]*Materials Research Division, National Laboratory for Sustainable Energy, Risø DTU, Frederiksborgvej 399, Roskilde 4000, Denmark*
[c]*Department of Electrical Engineering, Technical University of Denmark, Elektrovej 329, Kgs. Lyngby 2800, Denmark*

Abstract

In this work we present a simulation of a synchronous generator with superconducting rotor windings. As many other electrical rotating machines, superconducting generators are exposed to ripple fields that could be produced from a wide variety of sources: short circuit, load change, mechanical torque fluctuations, etc. Unlike regular conductors, superconductors, experience high losses when exposed to AC fields. Thus, calculation of such losses is relevant for machine design to avoid quenches and increase performance. Superconducting coated conductors are well known to exhibit nonlinear resistivity, thus making the computation of heating losses a cumbersome task. Furthermore, the high aspect ratio of the superconducting materials involved adds a penalty in the time required to perform simulations.

The chosen strategy for simulation is as follows: A mechanical torque signal together with an electric load is used to drive the finite element model of a synchronous generator where the current distribution in the rotor windings is assumed uniform. Then, a second finite element model for the superconducting material is linked to calculate the actual current distribution in the windings of the rotor. Finally, heating losses are computed as a response to the electric load. The model is used to evaluate the transient response of the generator.

© 2011 Published by Elsevier Ltd. Selection and/or peer-review under responsibility of Horst Rogalla and Peter Kes.

Keywords: Superconducting generator ; AC losses; Finite Element Simulation; Homogenization; HTS coils

1. Introduction

Nowadays, several examples of superconducting machinery can be found not just in the design but also in realization [1-3]. Several efforts have proven effective towards calculation of losses in superconductors [4-6]. However, the task has proven to be cumbersome due to the nonlinear E-J relation characterizing the material properties and the high aspect ratio of the superconducting regions in coated conductors. One

---

* Corresponding author.
E-mail address: V.Zermeno@mat.dtu.dk

additional complication comes from the multiscale nature of the problem: while the cross section of a generator itself is typically in the range of decimeters or even meters, the superconducting layer is 1 μm thick. Therefore a successful modeling tool should be able to span the 5 or 6 orders of magnitude connecting these phenomena.

Some improvements have allowed computing AC losses on coils and stacks of different sizes while modeling every conductor involved [6-8]. In the same context, it is important to note that several approximations based on homogenization techniques have been proposed to reduce the computational time and simplify the calculations for coils and stacks of tapes [9-11]. However, to this day, no calculation had been implemented for calculating AC losses of a superconducting rotating machine during a transient response. A tool to perform such calculation is necessary to optimize design, study performance and estimate safe operational margins. Such a tool must provide with a way to predict the heating losses induced in the superconducting windings as a response to either an electric load or torque change.

In this work we present a method to simulate the electromagnetic transient response of a superconducting generator. The technique is based upon a segregated model that decouples the dynamics of the generator and the dynamics of the superconducting coils. A homogenization technique is implemented to simulate the current distribution in the superconducting coils.

2. Modeling strategy

The overall model is constituted by two sub models (Fig. 1): the first being the simulator of a generator where superconducting properties are neglected; the second, a segregated model that uses the previously obtained results as boundary conditions to calculate the current distribution in the superconducting stator coils. Although no feedback from the second model is taken into account, this simplification should provide with accurate values for the actual Magnetic Field in the coupling boundary.

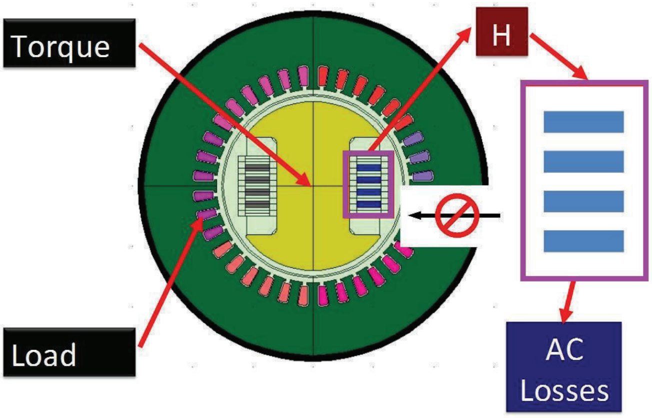

Fig. 1 Simulation strategy: In a first model, both electric load and mechanical torque are considered as known inputs of an electric generator. Using this model, the Magnetic Field is calculated in a coupling boundary (purple) around the rotor windings. A second model uses this as a Dirichlet boundary condition to compute for the AC losses. No feedback is considered from the second to the first model.

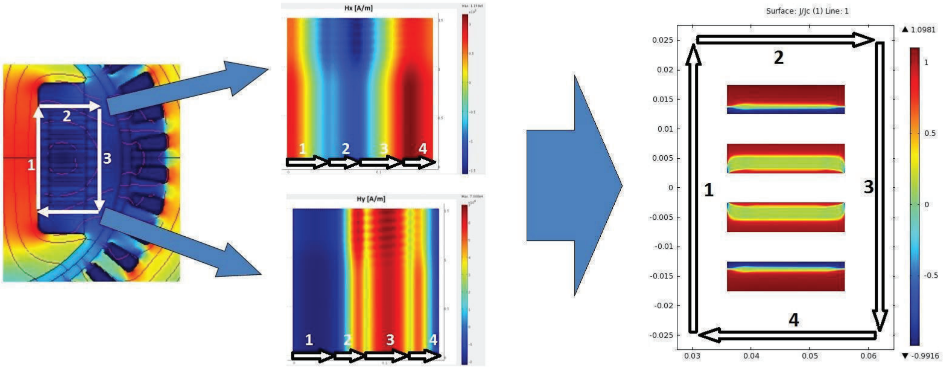

Fig. 2 Model Coupling: The Magnetic Field in the coupling boundary around the coils (left) is used as a boundary condition for the calculation of AC losses. Both components of the magnetic field are plotted (central figure): the horizontal axis of these plots corresponds to the arc length spanned by arrows 1-4. The vertical axis is time. Notice that after a 1 second long steady state, the field components start to change; this corresponds to the variation in applied load in the stator windings. The Magnetic Field evaluated in the path 1-4 is used as Dirichlet boundary condition for the superconducting coils. The left figure presents the current distribution in the superconducting coils at t=0.65s during the ramp up.

2.1. Generator model

Using the commercially available AC/DC module of COMSOL Multiphysics, a generator was modeled following design parameters as reported in [12]. For simplicity and homogeneity, every superconducting coil was assumed to be constituted of 50 turns of a coated conductor with critical current of 62.5 A. The superconducting windings of every coil have a cross section of 1E-4 m2 therefore, an engineering critical current of 3.125e7 A/m2 was considered. The rotor windings are composed by 20 turns of copper wire. A load case as described in section 3 was implemented.

2.2. Coils model

The electromagnetic properties of the superconducting coils were modeled using a formulation in the H Magnetic Field [4]. A power law with n value of 21 was considered, no Jc(B) dependence or magnetic substrate was taken into account in this model. To increase the computational speed, a homogenization technique based on similar assumptions as in a recently published work [11] was implemented. This aims to “wash out” the geometrical features of the coils’ layers i.e. the cross section of the coil was assumed to be an anisotropic bulk rather than the actual stack it represents.

2.3. Coupling

In order to link both models, the Magnetic Field in the generator was calculated in a boundary surrounding the superconducting coils. This data was then used as the time dependent Dirichlet boundary condition for the superconducting coil model. Fig. 2. Since the current in each individual tape of a given coil is constrained to a (possibly time dependent) known value. It is assumed that the Magnetic Field outside the coil should be similar to the one produced by a (possibly time dependent) known uniform current. In fact, this is the principle behind the simulation of electromagnetic machinery by finite element analysis, as the computation of the actual current distribution in each individual wire would require large memory and computing time resources. Therefore, no bidirectional coupling was implemented as it became redundant under the previously discussed assumption.

3. Results

To test the proposed strategy, a simple load change was implemented as in Fig. 3. First, a smooth ramp up current was applied to the superconducting coils, therefore increasing their current to 80% of the critical value. The system was let to relax for about 7 seconds, allowing for the transient behavior of the ramp up process to settle and fade. Then, at t=7.8 s a total resistance of 1 Ω was connected to every phase of the generator (taking into account the 0.32 Ω self-resistance of the copper windings). At t=9.8 s the total resistance was reduced to 0.5 Ω and back again to 1 Ω at t=11.8 s. Notice in Fig. 3 the instantaneous loss increase as the resistor is connected, or changed. A peak instantaneous loss of 0.4 W was observed during ramp up, peaks of about 0.3 W also appeared at increasing load changes, from R=∞ Ω (no load) to R=1 Ω at t= 8; and from R=1 Ω to R=0.5 Ω at t= 8 s. A smaller loss peak of about 0.05 W was observed when the load was reduced back to R=1 Ω at t= 12.

The 14 s transient response required approximately 6 hours for the generator model and about 12 hours for the superconducting coils model. Therefore transitory analysis of superconducting rotating machinery can be computed within a manageable time.

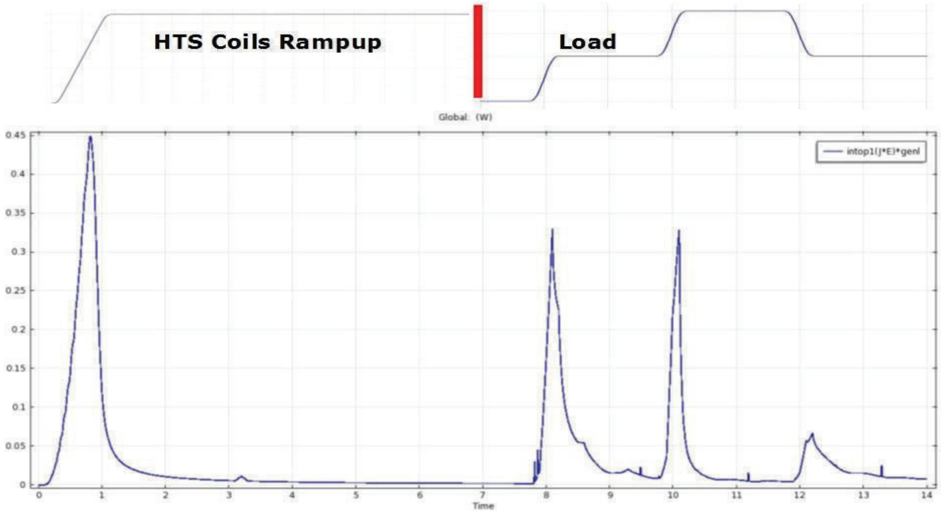

Fig. 3. Instant Joule losses in the superconducting coils of the generator. Starting from being in a zero field and zero current state, the current in the coils is ramped up to 80% of its critical value (top left figure). At t=7.8s, a passive load of R= 1 Ω is slowly connected to the terminals of the generator, later on at t=9.8s the load is changed to R= 0.5 Ω and back to R= 1 Ω at t=11.8s (shown as 1/R in the top right figure). The bottom figure shows a plot of the instantaneous losses (W) as a function of time.

4. Conclusions

A strategy to calculate the AC losses in a superconducting generator during transient operation was developed. Instantaneous losses were calculated for a ramp-up and load change test case. The strategy relies on decoupling the homogenized superconducting model from the generator model. Further studies must be carried out to compare and match the simulation results with experimental data and calibrate the simulator to make tailored predictions for specific transient operation cases. As an additional remark, it is also important to notice that since a homogenization technique was used for the superconducting coils, a similar treatment can be carried out for other machines and devices like motors or transformers with several conductors with ease.

Acknowledgements

We acknowledge support from the Technical University of Denmark, Vestas Wind Systems and SEP- Mexico.

References

[1] American Superconductor. *Superconductor Motors & Generators*. [Online] [Cited: September 1, 2009.] http://www.amsc.com/products/motorsgenerators/index.html.

[2] Eckels, P. W., Snitchler, G. *5 MW High Temperature Superconductor Ship Propulsion Motor Design and Test Results.* Naval Engineers Journal, Vol. 117, No. 4. (2005), pp. 31-36.

[3] J Frauenhofer, J Grundmann, G Klaus and W Nick. 2008, *Basic concepts, status, opportunities, and challenges of electrical machines utilizing hightemperature superconducting (HTS) windings.* EUCAS 2007 J. Phys.: Conf. Ser. 97 012189.

[4] R. Brambilla, F. Grilli, and L. Martini. Development of an edge-element model for AC loss computation of high-temperature superconductors. Supercond. Sci. Technol., vol. 20, pp. 16–24, 2007

[5] F Gömöry, M Vojenčiak, E Pardo, M Solovyov and J Šouc. *AC losses in coated conductors.* 2010 Supercond. Sci. Technol. 23

[6] E. Pardo. *Modeling of coated conductor pancake coils with a large number of turns*. 2008 Supercond. Sci. Technol. 21

[7] Ainslie, M; Zermeno-Rodriguez, V; Hong, Z; Yuan, W; Flack, T; Coombs, T. *An Improved FEM model for computing transport AC loss in coils made of YBCO coated conductors Rabit for electric machines.* Supercond. Sci. Technol. 24

[8] Rodriguez-Zermeno, V.; Mijatovic, N.; Traeholt, C.; Zirngibl, T.; Seiler, E.; Abrahamsen, A.; et al. *Towards Faster FEM Simulation of Thin Film Superconductors: A Multiscale Approach.* 2011 IEEE Trans. App. Supercond. Vol: 21, Issue: 3

[9] John R Clem, J H Claassen and Yasunori Mawatari. *AC losses in a finite Z stack using an anisotropic homogeneous-medium approximation*. 2007 Supercond. Sci. Technol. 20

[10] Weijia Yuan, A M Campbell and T A Coombs. *A model for calculating the AC losses of second-generation high temperature superconductor pancake coils*. 2009 Supercond. Sci. Technol. 22

[11] Leonid Prigozhin and Vladimir Sokolovsky. *Computing AC losses in stacks of high-temperature superconducting tapes.* 2011 Supercond. Sci. Technol. 24

[12] Mijatovic N., Jensen B., Traeholt C., Abrahamsen A., Rodriguez-Zermeno V., Pedersen N., et al. *High Temperature Superconductor Machine Prototype*. ICEMS 2011, Beijing, China

Appendix E

Article 5

A.B. Abrahamsen, B.B. Jensen, E. Seiler, N. Mijatovic, **V.M. Rodriguez-Zermeno**, N.H. Andersen, J. Østergård. “Feasibility study of 5 MW superconducting wind turbine generator”. Physica C 471 (2011) 1464–1469

Physica C 471 (2011) 1464–1469

Contents lists available at ScienceDirect

Physica C

journal homepage: www.elsevier.com/locate/physc

Feasibility study of 5 MW superconducting wind turbine generator

A.B. Abrahamsen [a,*], B.B. Jensen [b], E. Seiler [d], N. Mijatovic [b], V.M. Rodriguez-Zermeno [c], N.H. Andersen [a], J. Østergård [b]

[a] Materials Research Division, Risø DTU, Technical University of Denmark, Frederiksborgvej 399, Roskilde, Denmark
[b] Department of Electrical Engineering, Technical University of Denmark, Lyngby, Denmark
[c] Department of Mathematics, Technical University of Denmark, Lyngby, Denmark
[d] Institute of Electrical Engineering, Slovak Academy of Sciences, Bratislava, Slovakia

ARTICLE INFO

Article history:
Available online 13 May 2011

Keywords:
Superconducting generator
Offshore wind turbine
Race track coils

ABSTRACT

The feasibility of installing a direct drive superconducting generator in the 5 MW reference offshore wind turbine of the National Renewable Energy Laboratory (NREL) has been examined. The engineering current densities J_e obtained in a series of race track coils have been combined with magnetization measurements to estimate the properties of suitable field coils for a synchronous generator, which is more light weight than the conventional used combination of a gear box and a fast rotating generator. An analytical model and finite element simulations have been used to estimate the active mass of generators with varying number of poles. A 24 pole machine with an outer diameter of 4.2 m and active length and mass of 1.2 m and 34 tons is suggested possible, if a J_e = 300 A/mm^2 can be obtained in B = 4 T pointing to an operation temperature around 40 K.

© 2011 Elsevier B.V. All rights reserved.

1. Introduction

The urge for the development of offshore wind power in Europe has increased due to member state policies on fossil fuel independency by 2050 in order to reduce global warming and to secure energy supplies. Offshore wind power is an emerging technology with only 2.1 GW installed capacity in EU by the end of 2009, which should be compared to 76.2 GW and 156.5 GW of total installed capacity in EU and world wide respectively [1,2]. The EU offshore capacity must be expanded by two orders of magnitude by 2030 in order to supply 20% of the electricity demand from renewable sources [3]. Effort is now made to increase the size of offshore turbines and to improve the reliability by introducing mechanically simplified drive trains, such as direct drive generators based on permanent magnets [4].

The EU offshore capacity is provided by 830 turbines with an average size of 2.9 MW, but a small number of 5 MW offshore turbines have been in operation since 2009 with a distribution of 14 REpower 5M and 6 Areva Multibrid M5000 [4]. The REpower 5M turbine is based on a conventional drive train with a three stage gearbox and a generator rotating at 1500 revolutions per minutes (rpm), whereas the Multibrid turbine has a hybrid drive train with a single stage gearbox and a slow rotating generator at 150 rpm. The Repower turbine was developed as part of a research project and it is often referred to as the NREL reference turbine, since public informations about the properties are available [5].

We have previously examined the challenges of introducing a superconducting direct drive generator in future 10 MW offshore wind turbines and indicated that the price of coated conductors must be reduced by an order of magnitude before the 2030 target installation price of 1.5 MEuro/MW can be reached [6]. Secondly the reliability of a superconducting direct drive generator must be proven and in this paper we will examine the possibility of a demonstration installation in a turbine resembling the NREL reference turbine. In this context it is interesting to mention that the present offshore installation price is in the range of 3.4–3.6 MEuro/MW [7,8]. This price increased to 4–5 MEuro/MW for the present 5 MW installations and indicates a reasonable price for a superconducting direct drive demonstration.

This paper is organized by a presentation of the engineering current density J_e of a series of race track coils constructed within the Superwind project at DTU [9]. The temperature and field scaling of J_e as determined by magnetization measurements is used as input for determination of the properties of a synchronous generator suitable for the NREL reference turbine. An analytic generator model based on reluctance circuit analysis is introduced and compared to finite element simulations. Finally the active material of the superconducting generators is determined as function of the pole number and the feasibility is discussed.

---

[*] Corresponding author. Tel.: +45 46774741; fax: +45 46775758.
E-mail address: asab@risoe.dtu.dk (A.B. Abrahamsen).

0921-4534/$ - see front matter © 2011 Elsevier B.V. All rights reserved.
doi:10.1016/j.physc.2011.05.217

2. Superconducting race track coils

A number of race track coils have been constructed and tested as part of the Superwind project at DTU in order to demonstrate the feasibility of using high temperature superconducting tapes in rotor coils of synchronous generators suitable for wind turbines [9]. A coil design which can hold both Bi-2223(denoted first generation tape 1G) and coated conductor tapes (denoted second generation 2G) was developed. The design is based on an inner frame of 316 stainless steel onto which a superconducting tape and a glass fiber (GF) tape are wound. A copper block is soldered onto the beginning of the tape prior to winding and serves as one of the current contacts and another copper block is soldered to the end of the tape to provide the outer current contact as shown on Fig. 1. Thin copper wires are soldered onto the tape during the winding in order to allow voltage measurement directly across sections of the superconducting tapes and the wires are connected to a circuit board sitting on an outer 316 stainless steel frame, which also provides the mechanical support of the coil. The coils are vacuum impregnated by epoxy in a stainless steel form after the assembly and cured in air. Excess epoxy was mechanically cracked off from the coils, which were treated with epoxy release agents before assembling. Fig. 1 shows one of the coils, which allows a 20 mm thick winding of tape. The purpose of the coils is to stack them onto the iron rotor piece of a two pole test machine under construction at DTU.

The properties of the tapes used in the coils are summarized in Table 1 as well as the engineering current density J_e

$$J_e = \frac{I_C}{(t_{tape} + t_{insulation})w_{tape}} \tag{1}$$

defined as the critical current I_C of the tape divided by the sum of the tape t_{tape} and the insulation $t_{insulation}$ thickness multiplied by the width of the tape w_{tape}. Two types of Bi-2223 tapes from American Superconductors based on brass and steel reinforcement have been investigated using the glass fiber tape insulation technique in the winding of coil no. 1 and nos. 2–5 respectively. This method was also used for coil no. 6 holding a 2G $YBa_2Cu_3O_{6+x}$ coated conductor from American superconductor. Coated conductor tape of type 4050 from Superpower has been insulated by a thin layer of epoxy adding only 60 μm to the tape thickness and this is planned for the winding of coil no. 7 [11]. Estimates of the critical current of the coils have been obtained from 3D finite element simulations of the field distribution by assuming a homogenous current density in the entire cross section of the coil winding. The maximum field component normal to the tape surface was evaluated and compared to the field dependent critical current of the used tapes. This field component is along the c-axis of the textured HTC material in the tape and it is usually causing the smallest critical current. The Current–Voltage (*IU*) curves of the tapes were measured in liquid nitrogen at T = 77 K using an Agilent 34420A nano voltmeter connected to voltage probe copper wires soldered onto the tape surface with a 15–20 mm spacing. A HP6031A power supply was used to increase the current from $I = 0 - 120$ A controlled by a Labview program also collecting the voltage across the tape. A magnetic field of $B = 0 - 1$ T was applied perpendicular to the tape surface using an electromagnet [10].

The *IU* curves all showed a power law behavior

$$U = E_0 \cdot l \left(\frac{I}{I_C(\mathbf{B},T)}\right)^{n(\mathbf{B},T)} \tag{2}$$

where I is the transport current of the tape, $I_C(\mathbf{B}, T)$ is the critical current causing a voltage drop of $U = E_0 \cdot l$ and $n(\mathbf{B}, T)$ is the exponent of the power law quantifying how abrupt the transition from the superconducting to the resistive state will be. The choice of $E_0 = 10^{-6}$ V/cm was used as criteria for defining the critical current, where l is the distance between the voltage taps. The *IU* curves of the coils of Table 1 were obtained by measuring the voltage across the beginning and end copper wires of the coil immersed in liquid nitrogen as the current was increased in the setup also used for the tape measurements. Fig. 2 shows the *IU* curves of coil no. 1 based on 1G-brass tape and the 1G-steel tape is represented by the coils 2 and 3, which are similar to coils 4 and 5 (not shown). The two *IU* curves of coil 6 based on AmSC 348 tape are first showing a quench of the coil and the subsequent measurement confirming that the coil was not damaged by the quench. A critical current criteria of $U_0 = E_0 \cdot l$, where l is the length of the tape in the coil was applied and the *IU* curves in Fig. 2 have been normalized by the length of tape in the coil. The critical current and n-values of the coils at T = 77 K are listed in Table 1. The demonstrated engineering current density of the demonstration coils will be used to extrapolate the properties of larger race track coils operating in higher field and at lower temperatures.

Table 1
The properties of the high temperature superconducting tapes used in the Risø-DTU race track coil are listed in the first part of the table, whereas the predicted and obtained coil properties are shown below. 1G and 2G refers to Bi-2223 and coated conductor tapes respectively. *Expected values since winding of coil no. 7 is planned.

Coil no	1	2–5	6	7
Tape	1G Brass	1G Steel	2G 348C	2G 4050
Width (mm)	4.3	4.3	4.8	4.2
Thickness (mm)	0.39	0.28	0.22	0.10
I_C (77*K*, *sf*) (A)	150	145	95	125
Insulation	GF tape	GF tape	GF tape	Epoxy
Thickness (mm)	0.10	0.10	0.10	0.06
J_e (77*K*, *sf*) (A/mm^2)	68.8	88.7	61.8	186.0
No. turns	31	48–51	57	125*
Tape length (m)	16.3	25.4–28.8	31.6	69.1*
$I_{C,coil}$ 77 K (A)	76.7	82.9–83.5	69.4	–
n_{coil} 77 K	14.1	14.4–15.6	41.9	–

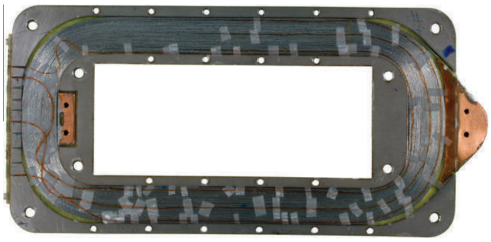

Fig. 1. Racetrack coil based on a winding of 5 mm wide high temperature superconducting tape. Electrical contact is provided by copper block at the two ends of the winding and thin copper wires are soldered onto the tape, whereby 4 point voltage measurements can be performed on selected sections of the tape. The inner and outer frame is made of 316 stainless steel and provides mechanical support for the coil. A circuit board is mounted on the left hand side of the steel frame for connection of voltage probe wires. The square hole of 150 mm × 60 mm in the middle can be fitted around an iron core of a test machine under construction at DTU.

3. Temperature and magnetic field scaling of critical current

The in-field pinning properties of the coated conductor tapes of the coils have been investigated in applied fields up to 16 T using a vibrating sample magnetometer (VSM) from Cryogenic Limited [12]. Pieces of tapes with identical width and length were mounted in straws using Kapton tape and inserted into the VSM with the applied field normal to the tape surface and parallel to the c-axis of

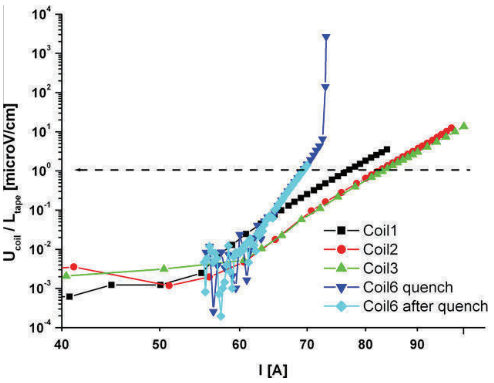

Fig. 2. *IU* curves of race track coil no. 1 (American Superconductor Bi-2223-Brass tape), coil nos. 2 and 3 (American Superconductor Bi-2223-Steel) and coil no. 6 (American superconductor coated conductor 348C) immersed in liquid nitrogen at $T = 77$ K. The two *IU* curves of coil no. 6 are showing a quench at $I = 73$ A and the following measurement confirming no damage during the quench. The noise level of the measurements of coil no. 6 is similar to the other coils and is not shown for clarity.

the $YBa_2Cu_3O_{6+x}$ superconductor. Magnetization curves were obtained by cooling the samples below the critical temperature $T_C \sim 93$ K in zero applied field and then sweeping the applied field $\mu_0 H = 0 \rightarrow 16 \rightarrow -16 \rightarrow 16 \rightarrow 0$ T. Subsequent magnetization curves were obtained by decreasing the temperature after the applied field was ramped to zero. The opening of the hysteresis curves Δm was determined as the difference between the $\mu_0 H = 16 \rightarrow -16$T and $\mu_0 H = -16 \rightarrow 16$ T part of the curves. Figs. 3 and 4 are showing the hysteresis opening scaled by the value at $T = 77$ K and zero applied field as function of applied field and at different temperatures. From the simple Bean model it is known that the magnetization hysteresis Δm will be proportional to the critical current density J_C of a superconductor, $\Delta m \propto J_C$. Similar relations are also found for thin film solution [13]. Thus the critical current $I_C(B, T)$ of the tapes scaled to the critical current I_C(*self field*, 77 K) provided by the tape manufacturers can be assumed to scale like the hysteresis scaling shown in Figs. 3 and 4. This temperature scaling will be used to estimate the current density of coils suitable for a wind turbine generator.

4. NREL reference turbine and generator model

The properties of the drive train of the NREL/REpower wind turbine are summarized in Table 2 and it should be noted that the weight of the gearbox and the generator is 80 tons. One could ask if a 80 tons superconducting direct drive generator could replace the conventional drive train, but the competition from $Nd_2Fe_{14}B$ permanent magnet based direct drive generators as installed in the recent Siemens SWT 3.0-101 turbine will call for a further weight reduction [16]. A target of 40 tons of active mass will be used in the following analysis, but a target price of the drive trains must first be estimated. A target installation cost of 2 MEuro/MW in 2020 will be assumed and this gives a drive train price estimate of $P_{DT} = 2\ \text{MEuro/MW} \cdot 5\ \mathit{MW} \cdot 1/3 \cdot 1/2 = 1.65$ MEuro, since the turbine fraction of the cost is often 1/3 and the drive train fraction is 1/2. Using the density of the superconductor/insulation composite deduced from Table 1 and an target price of 8 Euro/m in 2020 then one can estimate a maximum allowed volume of superconductor to be used. This would correspond to 228 km of AmSC 348C or 206 km of Superpower tape resulting in a weight of 2061 kg or 706 kg respectively. We will focus the analysis on a radial synchronous machine with a superconducting field winding and an stator winding without iron teeth at room temperature as has been demonstrated for large scale systems [17,18].

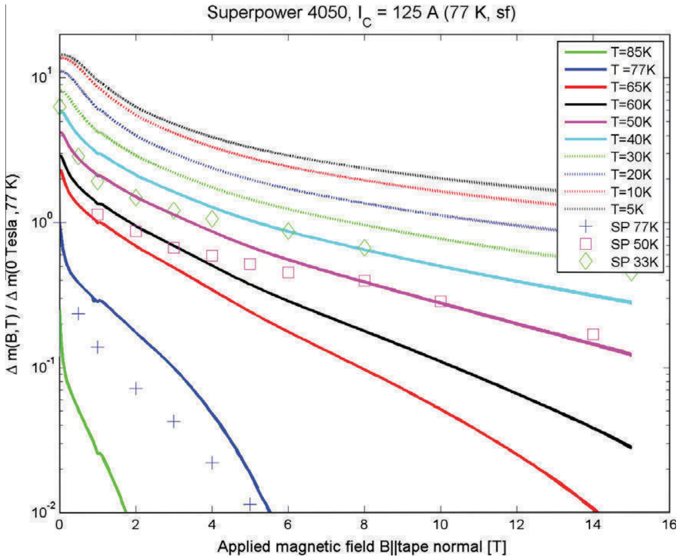

Fig. 3. Scaling of magnetization hysteresis $\Delta m(B, T)/\Delta m(0\ \text{T}, 77\ \text{K})$ of Superpower 4050 tape. A simple description of the pinning in superconductors like formulated in the Bean model will result in a proportionality between the magnetization hysteresis $\Delta m(B, T)$ and the critical current density J_C, $\Delta m(B, T) \propto J_C$. Thus one can in principle use the magnetization hysteresis to obtain information about the in-field performance of the tape by applying the scaling factor to the critical current of a tape obtained in a transport measurement. The markers are showing the publicly available in-field performance of a standard SP4050 tape with a $I_C = 80$ A (self field, 77 K) [14]. The discrepancy is believed to be caused by the fact that the tape studied here has an $I_C = 125$ A (self field, 77 K), which is expected also to result in a better in-field performance.

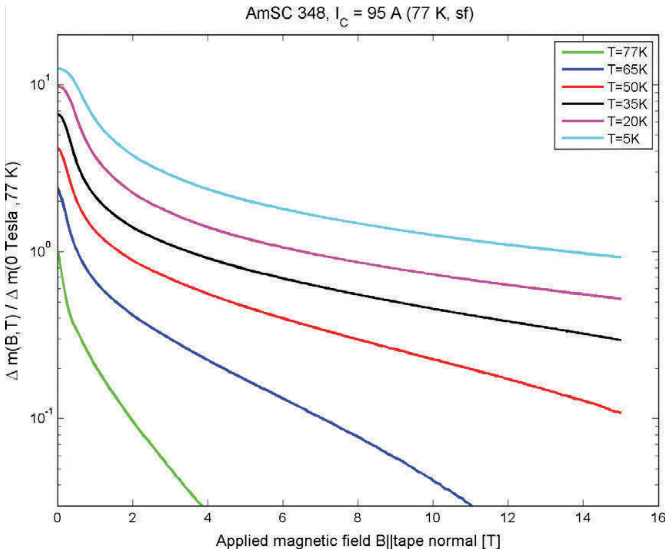

Fig. 4. Scaling of magnetization hysteresis of American Superconductor 348 C tape observed on top of the ferromagnetic response of the Ni–W based substrate of the tape.

Table 2
Drive train properties of the NREL/REpower wind turbine [5,15]

Power (MW)	5
Rotation speed (rpm)	12.1
Gearbox size $W \times H \times L$ (m)	4.6 × 3.0 × 4.1
Gearbox weight (tons)	63
Generator size $W \times H \times L$ (m)	2.2 × 2.2 × 4.0
Generator weight (tons)	17
Nacelle Size $W \times H \times L$ (m)	6.0 × 6.0 × 18
Nacelle weight (tons)	265

Alternatives based on bulk superconductors [19] or fully superconducting machines [20] have not been investigated, since the magnetization method of the bulk superconductor and low AC loss superconducting wires or tapes for a superconducting stator are still under development. A cryostat of 4 cm thickness on each side of the superconductor field winding is assumed and the outer diameter of the machine is fixed at D_{out} = 4.2 m in order to make the generator fit into the nacelle.

An analytical model based on a lumped reluctance circuit has been used to estimate air gap flux of a multipole machine as shown on Fig. 5a. The circuit on Fig. 5b describes the flux linkage between the two sides of a superconducting field winding by introducing reluctances related to the radial direction $R_{i,r}$ and to the circumferential direction $R_{i,c}$ of the active layers i of the machine. The reluctance reflects both the geometry of the machine and also the magnetic properties of the material specified by the relative permeability μ_r

$$R_{i,r} = \frac{1}{\mu_{r,i}\mu_0}\frac{l_{r,i}}{A_{r,i}} \tag{3}$$

where μ_0 is the vacuum permeability, l_r is the length of the flux path in the radial direction and A_r is the area which the flux passes through. Using Kirchhoff's circuit law on the reluctance loops a matrix relation between the magneto motive force F_{sc} of the superconductor and the flux ϕ_i in the loops is obtained

$$\begin{pmatrix} 0 \\ 0 \\ F_{sc} \\ 0 \\ 0 \\ 0 \end{pmatrix} = \begin{pmatrix} R_{11} & R_{12} & 0 & 0 & 0 & 0 \\ R_{21} & R_{22} & R_{23} & 0 & 0 & 0 \\ 0 & R_{32} & R_{33} & R_{34} & 0 & 0 \\ 0 & 0 & R_{43} & R_{44} & R_{45} & 0 \\ 0 & 0 & 0 & R_{54} & R_{55} & R_{56} \\ 0 & 0 & 0 & 0 & R_{65} & R_{66} \end{pmatrix} \begin{pmatrix} \phi_1 \\ \phi_2 \\ \phi_3 \\ \phi_4 \\ \phi_5 \\ \phi_6 \end{pmatrix} \tag{4}$$

The terms $R_{x,y}$ contain the reluctance sums linking the fluxes, ex. $R_{32} = -R_{si,c}$, $R_{33} = 2R_{si2,r} + 2R_{so1,r} + R_{si,c} + R_{so,c}$ and $R_{34} = -R_{so,c}$. By inverting Eq. (4) one can obtain the airgap flux of the pole and by assuming a sinusoidal angular variation one can deduce the maximum flux density B_0 in the airgap

$$\phi_3 = \int B_0 \cos(p\theta) r d\theta L \tag{5}$$

where p is the pole number and L is the active length of the machine. Similarly by assuming a sinusoidal current distribution of the 3-phase stator $I_S = \sqrt{2}A_S \cos(p(\theta - \psi))$ one can estimate the torque of the machine by

$$T = \sqrt{2}B_0 A_s V \cos(p\psi) \tag{6}$$

where A_s is the electric loading in [A/m] and $V = \pi r^2 L$ is the volume of the machine given by the airgap radius r and the active length L. The power is then $P = T\omega$, where ω is the angular rotation speed.

The analytical model was used to obtain the dimensions and hence the active mass of the machines, as the number of poles was varied. The output power was kept at 5 MW while the sum of the iron losses and the copper losses were maintained at 5% of the input power; the electric loading of the stator was kept at 90 kA/m; the airgap flux density at 2.4 T; and the core flux density was kept below 2.5 T. The finite element program Magnet from Infolytica was used to verify the magnetic field distribution as shown on Fig. 5c in the case of a 24 pole generator. The analytical model results were within 2–10% of the FE simulations. Fig. 6 shows the usage of active materials for the machines with a J_e = 70 A/mm^2 and a J_e = 300 A/mm^2 as obtained for the AmSC coil no. 6 and as expected for the Superpower coil no. 7 when the temperature is

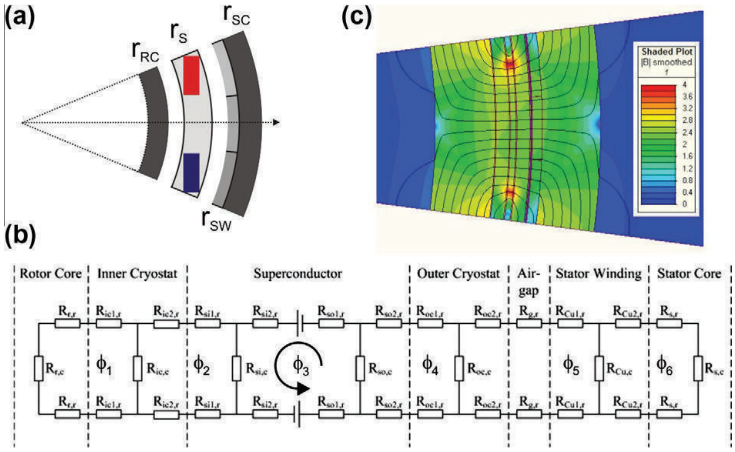

Fig. 5. (a) Layout of generator with $R_{RC1,2}$ denoting the inner and outer radius of the rotor iron core back, $R_{S1,2}$ denoted the superconducting field winding, $R_{SW1,2}$ the 3 phase stator winding and $R_{SC1,2}$ the stator core back iron. (b) A reluctance circuit representation of generator topology. (c) Finite element simulation of field distribution in a 24 pole machine.

lowered to $T = 30$ K and $T = 40$ K respectively. The operation temperature is deduced from Figs. 4 and 3 by identifying when the scaling factor is 1.13 for the AmSC tape and 1.61 for the Superpower tape at $B = 4$ T, which is the maximum flux density on the superconductors as seen on Fig. 5c. The finite element simulations showed that although the peak flux density in the iron was 2.5 T, the iron losses were very small (below 10 kW in all the cases). This is because the frequency was very low, e.g. 2.4 Hz for a 24 pole machine rotating at 12 rpm, and the iron losses depend heavily on the frequency. As the iron was heavily saturated where the peak flux density occurred, some flux would penetrate through the iron and come into the ambient air surrounding the iron. The magnitude of the flux density outside the iron core was investigated and found to be reduced to below 0.1 T at a distance of half a pole pitch, i.e. 250 mm outside the iron core the peak flux density was 0.07 T in the 24 pole machine. This was deemed acceptable by the authors, because the application is a wind turbine with free ambient air surrounding the machine.

5. Discussion

The general trend of Fig. 6 is that the amount of superconductor increases with the number of poles, but the usage of iron for both the rotor and stator can be decreased and thereby reduces the total weight of the generator. In the case of $J_e = 70$ A/mm^2 it is seen that the total target weight is first fulfilled for a 24 pole machine, but this would need about 5 tons of 2G AmSC tape, which is more than twice the allowed limit. One could stay within the usage limit of the tape by choosing a 8 pole machine, but then the total active mass is 90 tons. This indicates that a higher J_e is needed and this could be obtained by applying the epoxy insulation technique or to replace the GF tape with a thinner material. Additionally it should be said that using a wider tape would also increase the effective J_e, since the present tape has a soldering region at the edges of 0.4 mm/ 4.9 mm = 8%. Finally one could consider to decrease the operation temperature further, but this would also increase the complexity of the cryogenic design. In the case of $J_e = 300$ A/mm^2 the active weight target is fulfilled for a 20 or higher pole number machine and the usage of tape is within the price target, which would also allow funding for the cooling system and cryostat. Such a 24 pole machine does seem interesting because

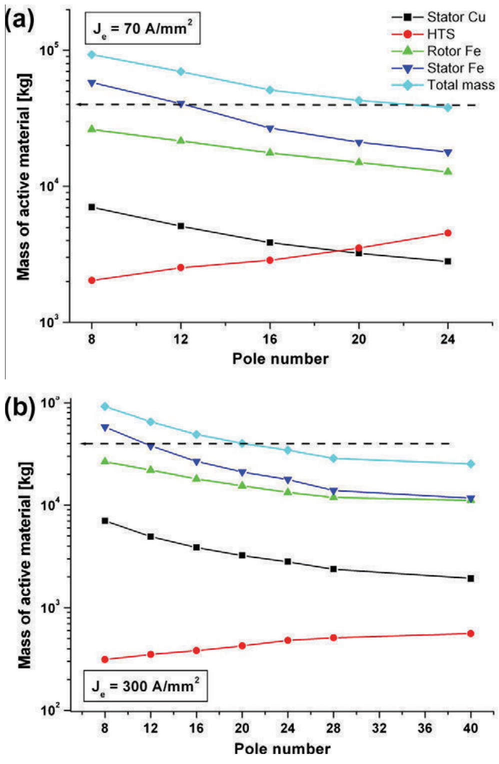

Fig. 6. Active material usage as function of pole number for a 5 MW direct drive superconducting generator with a 2.4 T airgap flux density and with a engineering current density of the superconducting winding corresponding to (a) $J_e = 70$ A/mm^2 and (b) $J_e = 300$ A/mm^2. The horizontal line indicate the design criteria of a total active mass of 40 tons.

the dimensions are down to a 4.2 m diameter and an active length of 1.2 m, which should allow for a large reduction of the nacelle size and thereby further weight reductions of the support structure. From this analysis it seems that the thin substrate of the Superpower tape is a great advantage combined with a thin insulation layer, but it does remain to be proved that sufficient quench protection can be applied to the coils.

6. Conclusion

A series of race-track coils holding 16–32 m of Bi-2223 and coated conductor high temperature superconducting tapes have been constructed and magnetization measurements have been performed on the tapes to estimate the applied field and temperature scaling of the engineering current density J_e. This was used as input for model calculations of the usage of active material in a direct drive synchronous radial multipole generator suitable for installation in the 5 MW offshore reference wind turbine described by NREL. It is concluded that a $J_e = 70$ A/mm^2 at $B = 4$ T and $T = 30$ K when using an AmSC tape is too low to both fulfilling a weight reduction target below 40 tons of active material and also a price target of 8 Euro/m. By increasing $J_e = 300$ A/mm^2 at $B = 4.0$ T and $T = 40$ K when using a Superpower tape it is indicated that both the weight and price targets can be fulfilled resulting in $D = 4.2$ m and active length and mass of 1.2 m and 34 tons respectively. Further studies on cryogenic design and quench protection are needed to confirm the feasibility of such a generator.

Acknowledgements

We would like to acknowledge the globalization initiative of DTU for the funding of the Superwind project and EDFA for funding studies of coated conductor properties in high magnetic field. Danfysik A/S for the insulation of the Superpower tape and Ultera A/S for providing the 1G brass tape. One of the authors (VMRZ) acknowledges financial support from: Technical University of Denmark, The Research School of the Danish Center for Applied Mathematics and Mechanics, Vestas Wind Systems and SEP-Mexico.

References

[1] European Wind Energy Association(EWEA) Report, "The European Offshore Wind Industry key Trends and Statistics 2009, January 2010. <www.ewea.org>.
[2] S. Sawyer, A. Zervos, "Global Wind 2009 Report, Global Wind Energy Council, March 2010. <www.gwec.net>.
[3] P. Capros, L. Mantzos, N. Tasios, A. De Vita, N. Kouvaritakis, ISBN 978-92-79-16191-9, 2010.
[4] P. Gardner, A. Garrad, L.F. Hansen, P. Jamieson, C. Morgan, F. Murray, A. Tindal, J. Ignacio Cruz, L. Arribas, Nicholas Fichaux, ISBN 9781844077106, EarthScan, March 2009.
[5] J. Jonkman, S. Butterfield, W. Musial, G. Scott, Technical Report NREL/TP-500-38060, February 2009.
[6] A.B. Abrahamsen, N. Mijatovic, E. Seiler, T. Zirngibl, C. Træholt, P.B. Nørgård, N.F. Pedersen, N.H. Andersen, J. Østergård, Supercond. Sci. Technol. 23 (2010) 034019.
[7] Thanet Offshore Wind Farm. <www.vattenfall.co.uk/en/thanet-offshore-wind-farm.htm>.
[8] Anholt Offshore Wind Farm. <www.dongenergy.com>.
[9] Superwind Project. <www.superwind.dk>.
[10] Arepoc s.r.o. <www.arepoc.sk>.
[11] Epoxy Insulation Done by Danfysik A/S. <www.danfysik.com>.
[12] Cryogenic Limited. <www.cryogenic.co.uk>.
[13] E.H. Brandt, Rep. Prog. Phys. 58 (1995) 1465.
[14] D.W. Hazelton, V. Selvamanickam, Proc. IEEE 97 (2009) 1831.
[15] REpower Systems AG Webpage. <www.repower.de>.
[16] Siemens SWT3.0-101 Specifications. <www.energy.siemens.com>.
[17] S.S. Kalsi, K. Weeber, H. Takesue, C. Lewis, H.-W. Neumueller, R.D. Blaugher, Proc. IEEE 92 (10) (2004) 1688.
[18] P.N. Barnes, M.D. Sumption, G.L. Rhoads, Cryogenics 45 (2005) 670686.
[19] Y. Jiang, R. Pei, Z. Hong, J. Song, F. Fang, T.A. Coombs, Supercond. Sci. Technol. 20 (2007) 585591.
[20] Q. Jiang, M. Majoros, Z. Hong, A.M. Campbell, T.A. Coombs, Supercond. Sci. Technol. 19 (2006) 11641168.

Appendix F

Article 6

Mijatovic, N.; Jensen, B.B.; Abrahamsen, A.B.; **Zermeno, V.M.R.**; Traeholt, C.; Pedersen, N.F. “Coil Optimization for High Temperature Superconductor Machines” IEEE TRANSACTIONS ON APPLIED SUPERCONDUCTIVITY, VOL. 21, NO. 3, JUNE 2011

Coil Optimization for High Temperature Superconductor Machines

N. Mijatovic, *Student Member, IEEE*, B. B. Jensen, *Member, IEEE*, A. B. Abrahamsen, V. M. R. Zermeno, C. Træholt, and N. F. Pedersen

***Abstract*—This paper presents topology optimization of HTS racetrack coils for large HTS synchronous machines. The topology optimization is used to acquire optimal coil designs for the excitation system of 3 T HTS machines. Several tapes are evaluated and the optimization results are discussed.**

The optimization algorithm is formulated to minimize the cost for the coils wound with one type of HTS as well as multiple HTS types. It could also be used to minimize other parameters, e.g. space required for the coils. The results are inherently highly dependent on the HTS properties, which at 20 K seem to be in favor of the 1 G tape. The maximal HTS savings achieved allowing multiple current supplies in the excitation system are investigated and estimated to be in the range of 50% for highly nonlinear J-B dependence HTS tapes.

***Index Terms*—HTS coil optimization, HTS machines, topology optimization.**

I. INTRODUCTION

HIGH temperature superconducting (HTS) applications are currently limited to a few main areas, such as advance medical diagnostics tools (MRI and NMR) and high energy particle research (accelerators). Large scale HTS applications have been thoroughly demonstrated in the energy sector, e.g. HTS cables, Superconducting Magnetic Energy Storage and HTS machines. Yet their commercialization is still limited by the cost of the HTS materials.

Optimization of the superconducting devices is crucial in order to make them competitive in a free market. At present the two main HTS candidates suitable for industrial applications are first generation (1 G) BSCCO and second generation (2 G) Coated Conductors. The price and performance of the HTS conductors depend strongly on the type of HTS material including: magnetic field dependent critical current density $J_c(B)$, manufacturing procedures, availability and quantity.

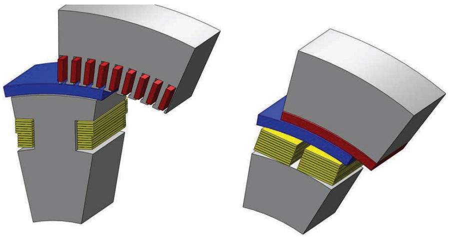

Fig. 1. Conceptual design of one pole-section for salient (left) and non-salient (right) synchronous machines with conventional and air-gap armature windings respectively. The magnetic steel is gray, the armature winding is dark red, the thermal insulation (vacuum chamber, spacers, radiation shield) is blue, and the space for the HTS coils is yellow.

The HTS price is usually the dominating factor of any system employing HTS. Optimization of the HTS usage and cost is therefore one of the main tasks of any superconducting system's designer. In the case of the electrical machines, many designs have been optimized for different applications ranging from air industry to utility companies [1]–[3].

We have employed the constrained Finite Element topology optimization in order to obtain improved HTS coil designs. Doing so it is possible to minimize the amount of HTS needed and hence the cost of HTS, or even to pinpoint a combination of HTS tapes with different properties in order to minimize the cost of the HTS machine.

II. METHODOLOGY

First the model of the HTS machine will be discussed, in order to formulate the topology optimization problem for the HTS coils in a machine. After that, details of the design of the HTS coils, HTS tapes, and most important constraints for the HTS coils will be reviewed. Finally, the formulation, implementation, and results of the topology optimization are described.

A. HTS Machine Design

Recommended HTS machine designs vary depending on the application that the machine is intended for. The common characteristic for all HTS machines, and one of their main benefits, is the power density which could be significantly larger than in conventional machines [4].

The two main designs, which the HTS synchronous machines are gravitating towards, are salient pole machines with conventional armature windings and non-salient multi-pole machines with air-gap armature windings [4], [5]. Both designs are shown and described in the Fig. 1.

Manuscript received August 03, 2010; accepted November 14, 2010. Date of publication December 30, 2010; date of current version May 27, 2011. This work was supported in part by the Technical University of Denmark under the globalization funded Project Superwind.dk.

N. Mijatovic, B. B. Jensen, N. F. Pedersen, and C. Træholt are with the Department of Electrical Engineering, Technical University of Denmark, Lyngby DK-2800, Denmark (e-mail: nm@elektro.dtu.dk; bbj@elektro.dtu.dk; nfp@elektro.dtu.dk; ctr@elektro.dtu.dk).

A. B. Abrahamsen is with the Materials Research Division, Risø National Laboratory for Sustainable Energy, Technical University of Denmark, Roskilde DK-4000, Denmark (e-mail: asab@risoe.dtu.dk).

V. M. R. Zermeno is with the Department of Mathematics, Technical University of Denmark, Lyngby DK-2800, Denmark (e-mail: V.Zermeno@mat.dtu.dk).

Color versions of one or more of the figures in this paper are available online at http://ieeexplore.ieee.org.

Digital Object Identifier 10.1109/TASC.2010.2094171

1051-8223/$26.00 © 2010 IEEE

The magnetic field is established by the HTS excitation winding. A cryostat for thermal insulation between the armature windings at room temperature and the HTS excitation windings at cryogenic temperatures is necessary. Given that the radial thickness of the cryostat is crucial for the machine design and directly responsible for the increase in required MMF, it is important to have a good estimate of the cryostat thickness necessary for operational temperatures between 20 K and 80 K.

The choice of material for the cryostat could be stainless steel (SS) or composite materials. The advantage of SS is the ease of manufacturing, and the advantage of the composite material is zero eddy current losses. The conduction and radiation heat transfer need to be suppressed with a vacuum chamber and multilayer insulation (MLI). The heat transfer through the mechanical and electrical connections also needs to be minimized. It could be assumed that for temperatures above 60 K a cryostat thickness of 20 mm can be achieved and for temperatures between 20 K and 60 K a cryostat thickness of 50 mm is necessary, due to the additional MLI and tighter heat inflow restriction because of lower cooling efficiency at lower temperatures.

Armature designs for HTS machines have been and still are a topic of a debate. Some arguments in favor of the air-gap armature design are removal of teeth saturation and higher armature current loadings. The advantages of air-gap armature windings have not yet been proven commercially and it was reported [6] that the air-gap armature winding involves several challenges, which still needed to be addressed e.g. cooling, mechanical integrity, assembly, and eddy current loss. However, if the trend for development of the compact machines continues, the air-gap armature winding's inherent advantages over conventional slotted armature windings will make the air-gap armature a more favorable choice.

It is also possible to draw some electromagnetic parallels between air-gap and conventional armature windings in slots. Having slotted configuration windings allows very small electromagnetic air gaps, but it also effectively decreases the radial flux path surface of the armature steel. This is taken in to account in conventional analytical machine design by the Carter coefficient, which modifies the effective air-gap to account for the effects of the iron teeth and slots dimensions. Bearing this in mind the model in Fig. 2 can also be used to analyse conventional slotted armatures by altering the inner radius of the stator steel according to the Carter coefficient.

B. HTS Coil Design

HTS tapes, both 1 G and 2 G, are manufactured as a thin tapes (0.1 mm–0.4 mm) of different widths (where 5 mm is the most common) [7]–[9]. In order to estimate the impact of very high engineering current densities in the HTS 2 G tapes, it is assumed that coated insulation is applied. This yields cross sectional areas of only 1 mm^2 for insulated tapes which allows compact coil designs. This tape would correspond to the most expensive tape and it is currently available in limited lengths. Extended tape lengths are currently only available for the 1 G tapes, which adds additional constrains on large scale applications.

Due to the mechanical limitations, the preferred coil layout for the HTS tapes is racetrack coils. Commercially available HTS tape can also be purchased in insulated form (usually Kapton of Glass-Fiber tape insulated) or the tape could be insulated by the coil manufacture. The insulation of the HTS tape can have large impacts on the compactness of the HTS structures.

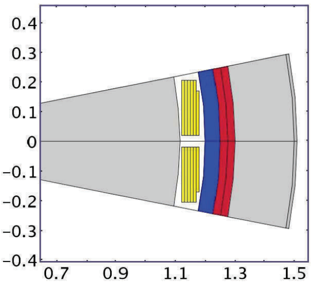

Fig. 2. Simplified model of a synchronous HTS machine with air-gap winding. The magnetic steel is gray, armature winding is dark red, thermal insulation (vacuum chamber, spacers, radiation shields) is blue and space for HTS coils is yellow. The units of x and y axes are [m].

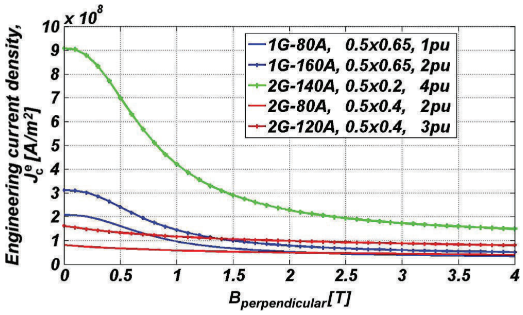

Fig. 3. Estimated engineering current density for 1 G and 2 G tapes at 20 K. The legend shows the HTS type, the critical current at 77 K in the self field, the estimated dimensions of the cross section of the insulated HTS tapes in [mm], and the estimated price of the tape all normalized to the price of 1 G–80 A. The insulation of the tapes is assumed to be 0.3 mm for glass fiber and 0.15 mm for coated insulation.

The HTS' magnetic dependence of its engineering critical current, i.e. $J_c^e - B$ data, is not standardized and is highly dependent on several parameters. In order to compare different types of HTS tapes, the data from published material [6]–[9] is used in this study together with estimated price ratios for the HTS tapes, Fig. 3.

It is also assumed that the price of the same type of HTS tapes scales linearly with the current rating. All HTS prices are normalized to 1 G-80 A, hence having the 1 G–80 A BSCCO tapes as a base value. The HTS 2 G tapes are more expensive at present but it is predicted that they could become cheaper than 1 G tapes.

C. Machine Electromagnetic Model

The model geometry of the conceptual machine used for the coil topology optimization is shown on Fig. 2. The 16 pole machine is non-salient and can be analysed with an air-gap armature winding or a slotted armature winding (simplified with the Carter coefficient). The FE model is reduced to one pole section using electromagnetic periodicity. The magnetic fields are calculated in steady state using the vector potential formulation of Maxwell's equations. The ferromagnetic steel used in the model for both cold and room temperature magnetic parts is the silicon steel M800-50.

The optimization space domain corresponds to the six double pancake coils. Each double pancake coil was presented with one rectangle of width of 10 mm.

D. Coil Magnetic Anisotropy

An important feature of HTS machines, which needs to be taken in to account, is the high sensitivity of the HTS current carrying capacity in magnetic fields. The prevailing impact on the critical current of the HTS tapes is the perpendicular direction of the magnetic flux to the wide side of the HTS tape. In the machine a single HTS tape is not in a homogenous field but rather, the gradients of the magnetic field can be very large over the entire HTS coil. However, critical currents of HTS tapes are usually derived by the 'short piece' experiment in different fields and field directions, where the field in the experiment is homogenous.

In the model, the perpendicular component of the flux density $\hat{B}_{\perp}^{[p,j]}(x)$ for tape p, is averaged over tape p width, w_{tape}, as shown in (1).

$$\hat{B}_{\perp}^{[p,j]}(x) = \frac{1}{w_{tape}} \int_{0}^{w_{tape}} {}^{j}opt \cdot |B_{\perp}(x,y)|\, dy \qquad (1)$$

The ${}^{j}opt$ represents the optimization variable which corresponds to the one type of HTS and $|B_{\perp}(x,y)|$ is the absolute value of the perpendicular component of the magnetic flux density. The peak perpendicular flux density, $B^{j}_{\max\perp}$, experienced by coils made from the j HTS material, can be found by searching for a maximum of the perpendicular flux density experienced by each tape calculated in (1), over the entire optimization domain Ω_{coils}, like in (2).

$$B^{j}_{\max\perp} = \overset{\Omega_{coils}}{MAX}\left(\hat{B}_{\perp}^{[p,j]}(x)\right) \qquad (2)$$

At this point we need to consider the excitation strategy. The conventional excitation strategy for a synchronous machine implies one excitation system and one excitation current. Yet it might be wise to allow more excitation currents in the case of HTS machines, assuming that the complication in the excitation system does not cancel out potential savings in HTS material. In this model that feature is investigated and compared with the case of having only one current supply.

The total spatial current distribution $J(x,y)$ with more than one excitation current supply, is calculated as the sum of all the coil current density contributions, as shown in the (3). The J_{cj} is the critical current density for the j type of HTS tape where the ${}^{j}opt(x,y)$ is the optimization variable which controls the spatial distribution of the j type HTS in the coil domain. An additional scalar variable is tied to each HTS type, K_j, scaling current density of that coil from the value defined by the critical current density $J_c(B)$

$$J(x,y) = \sum_{j} {}^{j}opt(x,y) \cdot K_j \cdot J_{cj}\left(B^{j}_{\max\perp}\right) \qquad (3)$$

The K_j coefficient is assumed to be fixed to 0.8 in the case of single HTS type employed, thus making sure the electrical loading of the HTS is 80% of the critical loading. In the case of different HTS types, the K_j should also be an optimization variable with values bounded between 0.4 and 0.8.

If one excitation current is allowed, (4) defines the maximal safe supply current.

$$I_{field} = \underset{j}{MIN}\left(K_j \cdot J_{cj}\left(B^{j}_{\max\perp}\right) \cdot {}^{j}A_{tape}\right) \qquad (4)$$

Since the different tapes have different cross sections ${}^{j}A_{tape}$, the engineering current densities need to be scaled in order to correspond to I_{field}. The total spatial distribution of the coil domain in this case is formulated in (5).

$$J(x,y) = \sum_{j} {}^{j}opt(x,y) \cdot \frac{I_{field}}{{}^{j}A_{tape}} \qquad (5)$$

E. Optimization Formulation

Topology optimization is used in structural studies to ensure minimum material usage and cost, and increased robustness of the structure, especially in an application where over sizing caries high cost penalty (airplane industry) [10].

The objective function, which in COMSOL [11] implementation is minimized by default, will have several terms in the formulation of the optimization problem. The form of the generalized objective function, which is minimized is shown in (6).

$$\min\ Objectiv = \sum_{k=1}^{3} obj_k \qquad (6)$$

where obj_k are contributions to the objective function.

The optimization variables, ${}^{j}opt(x,y)$, are defined in the 2D space which corresponds to the space intended for the HTS coils. The idea is to allow the optimization algorithm to control the spatial distribution of the HTS tapes. All optimization variables are constrained between zero and one with (7) and (8).

$$0 \le {}^{j}opt(x,y) \le 1 \qquad (7)$$

$$\sum_{j} {}^{j}opt(x,y) \le 1 \qquad (8)$$

If the optimization variable is one, current carrying HTS will be present at those coordinates and if it is zero, no HTS tape will be present. Additionally the sum of all the optimization variables at a specific coordinate need to be less than or equal to one, which corresponds to the statement that the same space can have only one tape.

However, since it is not possible to constrain the optimization variables in COMSOL to only binary values, the first term of the objective function, obj_1, needs to penalize all values between zero and one, which is done with (9).

$$obj_1 = \sum_{j}\left(c_{obj1} \int_{\Omega_{coils}} \left[a_{obj1} - \left({}^{j}opt - b_{obj1}\right)^2\right] d\Omega_{coils}\right) \qquad (9)$$

where the adjusting constants a_{obj1}, b_{obj1} and c_{obj1} are set to 0.25, 0.5 and 100 respectively, in order to allow this term to have significant effect to the value of the objective function.

$$obj_2 = \left(a_{obj2}\left(B^{design}_{r,peak} - 2\underbrace{\int_{-\pi/2}^{\pi/2} B_r \cos(\theta) d\theta_{armature}}_{firstharmonic}\right)\right)^2 \tag{10}$$

The second term of the objective function, obj_2, shown in (10) is to make sure that the fundamental harmonic of the radial air-gap flux density, B_r, is maintained closely to the desired design value, $B^{design}_{r,peak}$. Thus, the $obj2$ will have the dominating effect on the objective function as long as the air-gap flux is far from the desired value. The constant a_{obj2} controls how dominant this term is in the final objective function and in this implementation its value is set to 5.

The final term of the objective function is the price contributions of each HTS which is calculated using (11).

$$obj_3 = \sum_j \left(\int_{\Omega_{coil}} {}^{j}opt \cdot \frac{C_j}{{}^{j}A_{tape}} \cdot d\Omega_{coil}\right) \tag{11}$$

where the price of each tape is C_j.

III. RESULTS

In order to compare the coil optimization results of the generator design shown in the Fig. 2, the price of the optimized coil topology made from a single type of HTS material (both 1 G and 2 G) is compared.

The limiting factor during simulations, especially for the case of multiple tape coils, was a built-in optimization algorithm in COMSOL, which searches only for local minimum [10]. Thus it is very important to keep in mind that the solution, which is a local minimum is highly dependent on the initial conditions. This requires a good initial estimate of which tape should be in which portion of the coil.

1) Single Tape Coils: An optimization example is done on the 16 pole air-gap stator machine. For the machine design input the flux density was set to 3 T with an HTS operating temperature of 20 K.

The optimization results for the 16 pole machine in Fig. 2 are shown in Fig. 4. In the case where the coils consist of a single HTS, the coils made from 2 G 120 A tape (with a relative price of 3 pu), had a price of 54×10^3 pu, as compared to the coils made from 1 G 180 A tape (with a relative price of 2 pu) where the price was only 18×10^3 pu. The price difference between 1 G and 2 G is a factor of three which is in line with expectations, since 1 G tapes have more current capacity between 2 T and 3 T and are 50% cheaper, according to Fig. 3. The coils from ultra thin 2 G 140 A tape would result in a price of 63×10^3 pu. However, the cost impact of the coil space reduction is not taken into account here. This could have a significant impact on the overall price of the machine as it could result in a reduced effective air-gap and hence a lower required value of ampere-turns for a given air-gap fluxes density. The lowest grading 1 G 100 A and 2 G 80 A tapes were unable to produce the required 3 T with the allowed coil space.

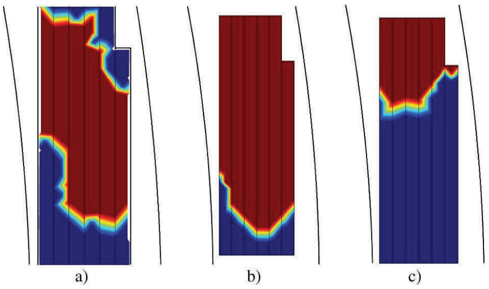
a) b) c)

Fig. 4. Optimization results for HTS coils with single HTS type at 20 K. The results are shown only for the upper side of the coils, since the current distribution is symmetrical to the x axis. The dark red is the HTS active domain and the dark blue empty space. (a) 1G-180A-2pu; (b) 2G-120A-3pu; (c) 2G-140A-4pu.

The optimization results show that the 1 G-180 A tape is most advantageous at 20 K. It has the lowest price and degree of magnetic anisotropy. The results for the ultrathin 2 G-140 A tape are interesting, with a very compact coil of similar price to the 2 G-120 A tape. This tape requires further analysis which allows for the potential benefits of the compact coil to be taken into account.

2) Multiple Excitation Currents: In order to investigate the potential savings in HTS material by allowing multiple excitation currents, we have examined the extreme case were each tape has its own current supply, which should yield the lowest amount of HTS needed to achieve 3 T. This means that each tape operates with its own maximal safe J defined by $J_c(B)$. It is not realistic that each tape would have its own current supply, but it is realistic to imagine that the HTS area was divided into sections with a few separate current supplies.

The optimization was carried out with the same tapes as in the single excitation current case. The optimization resulted in the following price for 1 G–180 A, 2 G–120 A and 2 G–140 A respectively: 12×10^3 pu, 25×10^3 pu and 26×10^3 pu.

The optimization has confirmed the potential for significant HTS savings if multiple current supplies are allowed. The tapes with higher degree of nonlinearity in $J_c - B$, as 2 G at 20 K, have potential savings exceeding 50%. Such savings are less for the 1 G tapes and are in the order of 30% at 20 K.

IV. CONCLUSION

In this article an optimization algorithm for HTS coils in electrical machines is presented. We have estimated the price ratios of three commercially available types of HTS and used it to derive the price ratios for excitation coils of multi-pole HTS machines. The results were clearly in favor of 1 G tape at 20 K, due to its lower cost and higher current capacity. Promising results were achieved with ultra thin 2 G tape, which require further investigation. Additionally, the article discusses the potential HTS savings of using multiple excitation supplies. Future work will focus on optimal design of coils with two and more types of tapes with one or more current supplies.

REFERENCES

[1] M. H. Ali, W. Bin, and R. A. Dougal, “An overview of SMES applications in power and energy systems,” *IEEE Trans. Sustainable Energy*, vol. 1-1, pp. 38–47, Mar. 18, 2010.

[2] J. Cho *et al.*, “Design and experimental results of a 3 phase 30 m HTS power cable,” *IEEE Trans. Applied Superconductivity*, vol. 16, no. 2, pp. 1602–1605, June 2006.

[3] S. S. Klasi, “Advances in synchronous machines employing high temperature superconductors (HTS),” in *IEEE Int. Conf. Electric Machines and Drives Conference 2003-IEMDC’03*, vol. 1, pp. 24–28.

[4] G. Klaus, “Design challenges and benefits of HTS synchronous machines,” in *IEEE General Meeting 2007*, June 2007, pp. 1–8.

[5] P. J. Masson and C. A. Luongo, “HTS machines for applications in all-electric aircraft,” in *IEEE General Meeting 2007*, June 2007, pp. 1–6.

[6] E. J. Davies, “Airgap winding for large turbogenerators,” in *Proc. of the Institution of Electrical Engineers*, 1971, vol. 118-3.4, pp. 529–535.

[7] [Online]. Available: http://www.superpower-inc.com/content/technical-documents

[8] [Online]. Available: http://global-sei.com/super/hts_e/index.html

[9] [Online]. Available: http://www.amsc.com/products/htswire/

[10] M. P. Bendsøe, N. Olhoff, and O. Sigmund, “Recent developments in the commercial implementation of topology optimization,” in *IUTAM Symp. on Topological Design Optimization of Structures, Machines and Materials*, 2006, vol. 137, pp. 239–248.

[11] *“Comsol Multiphysic 4.0a—Optimization Module, Software Manual,”* 2010.